Modelling of the Thermal History During Submerged Arc Welding and Wire and Arc Additive Manufacturing

by

Anqi Shao

A thesis submitted in partial fulfillment of the requirements for the degree of

Master of Science

in

Chemical Engineering

Department of Chemical and Materials Engineering
University of Alberta

Abstract

The finite element method (FEM) and finite element analysis (FEA) are numerical techniques to solve partial differential and ordinary differential equations. They are widely used in engineering, physics, and other fields. The development of these FEM and FEA makes it possible to accurately simulate the temperature history of many processes, such as welding and additive manufacturing process.

In this work, a general-purpose finite element analysis (FEA) software, ABAQUS, was used to predict the temperature profile on the welding line for submerged arc welding (SAW) and wire and arc additive manufacturing (WAAM) processes. A new technology called Additive Manufacturing Modeler was utilized within ABAQUS to enhance the accuracy of the simulation. The peak temperature and cooling rates can be determined with the temperature profile, which is crucial for understanding and optimizing the welding and additive manufacturing processes. Using the 3D model in ABAQUS also makes it possible to know the temperatures at any time and at any point on the plate. This allows for a more comprehensive process analysis. Additionally, the bead widths and depths during the processes can therefore be predicted, which can be used to control the final geometry of the product.

Finally, the predicted results from the ABAQUS model were compared with experimental data taken under similar conditions. For the SAW process, the results were compared with the research done by Lecoanet [1], who made measurements using thermocouples. The thermal history on the welding line and also in the heat-affected zone are analyzed and compared. As for the WAAM process, the results are compared with McDonald's [2] work, where the temperature profile on the

welding line and also the solidification cooling rates were analyzed and compared. The penetration of the bead is also compared. The results from the model showed good agreement with the experimental data, validating the simulation's accuracy. The work demonstrates the applicability of using the Additive Manufacturing Modeler technology within ABAQUS for predicting temperature profiles and other process parameters in welding and additive manufacturing.

Preface

This thesis is an original work by Anqi Shao and is the result of a co-supervision collaboration between the University of Alberta and ENSIC in France. The models and simulations presented in the thesis were all designed by myself. The experimental measurements are collected by A.Lecoanet and A.McDonald.

Acknowledgments

I would like to begin this section by expressing my deepest gratitude to my supervisor, Dr. Hani Henein, for all his support and guidance throughout the course of this research. His encouragement, expertise, and valuable advice played a crucial role in the successful completion of this thesis. Thank you, Dr. Henein. Your teachings and this research experience will stay with me for the rest of my life.

I would also like to thank my colleagues in the AMPL group, especially Dr. Jonas Valloton, Anne McDonald, Geoffrey Bonias, Tailin Ren, and Lucas Martin Ishida, for their support, collaboration, and friendship. Thank you for all the discussions, comments, and help.

I would like to extend my sincere thanks to NSERC, EVRAZ and HI-AM for providing the financial support necessary for this research. This work would not have been possible without their sponsorship.

Finally, I would like to extend my heartfelt thanks to my family for their love and support throughout my academic journey and long before that. Even though we are physically far apart, I feel your presence and guidance with me every step of the way. Thank you for always being there for me.

Thank you all for your contributions and support.

Table of Contents

Abstract ii
Preface iv
Acknowledgments v
Table of Contents vi
List of Tables ix
List of Figures x
List of Symbols xiv
Glossary of terms xvi
Chapter 1: Introduction 1
Chapter 2: Literature review 2
2.1 Welding Process 2
2.1.1 Submerged arc welding (SAW) 2
2.1.2 Gas metal arc welding (GMAW) 3
2.2 Treatment of convection in the weld pool 4
2.3 Temperature measurement methods 5
2.4 Material 7
2.4.1 X70 7
2.4.2 17-4 PH 7
2.5 Wire and arc additive manufacturing (WAAM) 8
2.5.1 Additive Manufacturing (AM) 8
2.5.2 Wire and arc additive manufacturing (WAAM) 8
2.6 Simulation 10
2.6.1 Prediction of the thermal effect 10
2.6.2 Goldak heat source 11
2.6.3 Thermal efficiency 13
2.6.4 Finite element method (FEM) and finite element analysis (FEA) 14
2.6.5 FEM and FEA for welding 14

2.6.6 FEA for WAAM 15
2.6.7 Additive Manufacturing Modeler in Abaqus 16
2.7 Summary 18
Chapter 3: Modelling of the thermal history in submerged arc welding (SAW) using Abaqus. .. 19
3.1 Introduction 19
3.2 Governing equations 19
3.3 Simulation Description 22
3.3.1 Geometry 22
3.3.2 Thermo-physical properties 22
3.3.3 Initial and boundary conditions 23
3.3.4 Mesh design 25
3.3.5 Additive Manufacturing Modeler 28
3.4 Results 28
3.5 Validation with experimental tests 34
3.6 Summary 37
Chapter 4: Modelling of the thermal history of Wire and arc additive manufacturing (WAAM) using Abaqus. 38
4.1 Introduction 38
4.2 Simulation Description 38
4.2.1 Geometry 38
4.2.2 Thermo-physical properties 39
4.2.3 Initial and boundary conditions 41
4.2.4 Mesh design 45
4.3 Results: 47
4.4 Validation of the model 52
4.4.1 Experimental setup 52
4.4.2 Comparison of Abaqus prediction and experimental results 55
4.5 Summary 59

Chapter 5: Conclusions and future work 62
5.1 Conclusions of this work 62
5.2 Future work 62
References 64
Appendix A 69
A.1. Thermophysical properties for X70 69
A.2. Thermophysical properties for 17-4 PH 71
Appendix B 73
B.1. Goldak parameters used in SAW simulation 73
B.2. Goldak parameters used in WAAM simulation 73
Appendix C 74
C.1 Experimental settlements for SAW in the previous research 74
C.2. Simulation results for WAAM from ABAQUS 75

List of Tables

Table 4-1: Composition of 17-4 PH 40
Table 4-2: Composition of Exocor Executive 630 wire........ 53
Table 4-3: Details of the measurement of Abaqus prediction and experimental data. 61
Table A. 1: Thermal conductivity of 17-4PH for different temperatures........ 71
Table B. 1: Goldak parameters used in SAW........ 73
Table B. 2: Goldak parameters used in WAAM........ 73

List of Figures

Figure 2-1: Schematic of S.A.W. Equipment Layout & Process[5] 3
Figure 2-2: Schematic of GTAW Equipment Layout & Process[8] 4
Figure 2-3: Weld performed with eight thermocouples embedded in the plate [16] 6
Figure 2-4 Diagram of WAAM process. [21] 9
Figure 2-5: Schematic diagram of Goldak model presented in (Kik) [36] 12
Figure 2-6: AM Modeler in ABAQUS.......... 17
Figure 3-1: Geometry of the plate.......... 20
Figure 3-2: Geometry of the bevels. 22
Figure 3-3: Selected part for initial bead temperature in Abaqus. 23
Figure 3-4: Selected part for the plate preheating in Abaqus. 24
Figure 3-5a: Illustration of the mesh design. 26
Figure 3-5b: Illustration of mesh design after zooming. 26
Figure 3-6: Mesh convergence tests. 27
Figure 3-7: Illustration of the directions. 29
Figure 3-8: An example of the temperature profile along the weld line. 30
Figure 3-9: Temperature profiles along bead width for different depths. 30
Figure 3-10: Temperature profiles for different heat inputs along the weld line. 32
Figure 3-11: Temperature profiles for different heat inputs along the x-axis. 32
Figure 3-12: Temperature profiles for different travel speeds along the weld line. 33
Figure 3-13: Temperature profiles for different travel speeds along the x-axis. 34
Figure 3-14: Comparison of temperature profiles as a function of time at position R2KbZ2. (A combination of plots) [1] 35
Figure 3-15: Comparison of temperature profiles as a function of time at position R2KaZ1. (A combination of plots) [1] 36
Figure 4-1: Geometry of the plate and the bead. 39
Figure 4-2: Temperature as a function of mole fraction of solid. 40
Figure 4-3: Latent heat per gram as a function of temperature. 41
Figure 4-4: Illustration of symmetry. 42
Figure 4-5: Convection and radiation on the plate. 43

Figure 4-6: Mesh convergence test. 46
Figure 4-7: Mesh size design. 46
Figure 4-8: Example of the model results. 47
Figure 4-9: Indication of position for points A and B. 48
Figure 4-10: Temperature profile at point A. 48
Figure 4-11: Temperature profile at point B. 50
Figure 4-12: Predicted solidification cooling rate as a function of heat input. 51
Figure 4-13: An example of an illustration for bead depth in the model. 51
Figure 4-14: Bead depth as a function of heat input. 52
Figure 4-15: Experimental setup for WAAM process. 53
Figure 4-16: Geometry of the plate in the experiment. 54
Figure 4-17a: Temperature profiles on the warm bead for the 5th plate. 56
Figure 4-17b: Temperature profiles in the range of liquidus and solidus temperature on the warm bead for the 5th plate. 56
Figure 4-18a: Temperature profiles on the warm bead for the 11th plate. 57
Figure 4-18b: Temperature profiles in the range of liquidus and solidus temperature on the warm bead for the 11th plate. 57
Figure 4-19a: Temperature profiles on the warm bead for the 21st plate. 58
Figure 4-19b: Temperature profiles in the range of liquidus and solidus temperature on the warm bead for the 21st plate. 59
Figure 4-20: Solidification cooling rate as a function of heat input for both predictions and experiments. 60
Figure A.1: Density as a function of temperature given by Thermo-Calc. [1] 69
Figure A.2: Derivative of Enthalpy(J/g.K) as a function of temperature given by Thermo-Calc. [1] 70
Figure A.3: Thermal conductivity as a function of temperature given by Thermo-Calc. [1] 71
Figure A.4: Density as a function of temperature. 72
Figure A.5: Heat capacity as a function of temperature. 72
Figure C.1: Geometry of the machined plate, with the positions of the thermocouples[1] 74
Figure C.2: An example of polished and etched cross-sections presented in previous research.[1] 75

Figure C.3a: Temperature profiles for the 4^{th} plate. 76
Figure C.3b: Temperature profiles in the range of liquidus and solidus temperature for the 4^{th} plate. 76
Figure C.4a: Temperature profiles for the 5^{th} plate. 77
Figure C.4b: Temperature profiles in the range of liquidus and solidus temperature for the 5th plate. 77
Figure C.5a: Temperature profiles for the 7^{th} plate. 78
Figure C.5b: Temperature profiles in the range of liquidus and solidus temperature for the 7^{th} plate. 79
Figure C.6a: Temperature profiles for the 11^{th} plate. 79
Figure C.6b: Temperature profiles in the range of liquidus and solidus temperature for the 11^{th} plate. 80
Figure C.7a: Temperature profiles for the 12^{th} plate. 80
Figure C.7b: Temperature profiles in the range of liquidus and solidus temperature for the 12^{th} plate. 80
Figure C.8a: Temperature profiles for the 15^{th} plate. 81
Figure C.8b: Temperature profiles in the range of liquidus and solidus temperature for the 15^{th} plate. 82
Figure C.9a: Temperature profiles for the 17^{th} plate. 82
Figure C.9b: Temperature profiles in the range of liquidus and solidus temperature for the 17^{th} plate. 83
Figure C.10a: Temperature profiles for the 18^{th} plate. 83
Figure C.10b: Temperature profiles in the range of liquidus and solidus temperature for the 18^{th} plate. 84
Figure C.11a: Temperature profiles for the 19^{th} plate. 84
Figure C.11b: Temperature profiles in the range of liquidus and solidus temperature for the 19^{th} plate. 85
Figure C.12a: Temperature profiles for the 21^{st} plate. 85
Figure C.12b: Temperature profiles in the range of liquidus and solidus temperature for the 21^{st} plate. 86
Figure C.13a: Temperature profiles for the 22^{nd} plate. 86

Figure C.13b: Temperature profiles in the range of liquidus and solidus temperature for the 22nd plate. 87
Figure C.14a: Temperature profiles for the 23rd plate. 87
Figure C.14b: Temperature profiles in the range of liquidus and solidus temperature for the 23rd plate. 88
Figure C.15a: Temperature profiles for the 24th plate. 88
Figure C.15b: Temperature profiles in the range of liquidus and solidus temperature for the 24th plate. 89
Figure C.16a: Temperature profiles for the 25th plate. 89
Figure C.16b: Temperature profiles in the range of liquidus and solidus temperature for the 25th plate. 90

List of Symbols

Latin alphabet:

c_p	Specific heat (J/(kg.K))
d	Diameter of the nozzle (m)
h	Convection heat transfer coefficient ($W/m^2.K$)
k	Thermal conductivity (W/(m.K))
$\dot{q}_c$	Rate of heat transfer by convection (W)
$\dot{q}_r$	Rate of heat transfer by radiation (W)
$\dot{q}_x$	Rate of heat conduction at the position x (W)
q_x	heat conduction in x direction (J)
$\dot{q}_{x+dx}$	Rate of heat conduction at the position x+dx (W)
$\dot{q}_y$	Rate of heat conduction at the position y (W)
$\dot{q}_{y+dy}$	Rate of heat conduction at the position y+dy (W)
$\dot{q}_z$	Rate of heat conduction at the position z (W)
$\dot{q}_{z+dz}$	Rate of heat conduction at the position z+dz (W)
$\dot{q}_{gen}$	Rate of heat generation (W)
r	Distance from the heat source (m)
t	Time (s)
v	Travel speed (m/s)
E	Energy content of the element (J)
P	Laster power (W)
Pr	Prandtl number
Q	Power density (W/m^3)
Re	Reynolds number
S	Surface area (m^2)
T	Temperature (K) or (°C)
T_∞	Temperature of the surroundings (K) or (°C)
Z	Distance travelled by the heat source (m)

Greek alphabet:

α	Thermal diffusivity (m^2/s)
ε	Emissivity 0.85-0.9
ρ	Density (kg/m^3)
σ	Stefan-Boltzmann constant (W/m^2K^4)
λ	Absorptivity
ξ	Moving coordinate (m)
η	Thermal efficiency

Glossary of terms

AM	Additive Manufacturing
CFD	Computational Fluid Dynamics
CR	Cooling Rate
DED	Directed Energy Deposition
FDM	Fused Deposition Modeling
FE	Finite Element
FEA	Finite Element Analysis
GMAW	Gas Metal Arc Welding
GTAW	Gas Tungsten Arc Welding
HAZ	Heat-affected Zone
IR	Infrared
LDED	Laser-directed Energy Deposition
PAW	Plasma Arc Welding
SAW	Submerged Arc Welding
SLA	Stereolithography
SLS	Selective Laser Sintering
SLM	Selective Laser Melting
TIG	Tungsten Inert Gas

Chapter 1: Introduction

In the early 20th century, the first mathematical model appeared and gave a fundamental equation to predict the temperature history of the welding process. [30] The finite element method and finite element analysis for 3D simulation were then developed to simulate the welding process more accurately. [36] Though the FE package was implemented for additive manufacturing simulation in Abaqus, the method can also predict the temperature profile for the welding process. It is possible to predict the temperature profile in submerged arc welding because the software can simulate the heat transfer and thermal stresses during the welding process. Submerged arc welding is a widely used technique known for its high productivity and consistent quality. Predicting the temperature profile is crucial to ensure the quality of the weld. For wire and arc additive manufacturing (WAAM), AM modeler in Abaqus is also a powerful tool for predicting the temperature profile of WAAM. It considers the complex physics of the process, including the heat transfer and fluid flow, which allows for a realistic simulation of the thermal behaviour of the wire and the base material, the solidification cooling rate, and the heat-affected zone.

This work focused on the peak temperature, solidification cooling rates, bead width, and penetration depth because they can significantly impact the weld's final properties. The models can optimize the SAW or WAAM by adjusting the process parameters to achieve the desired microstructure and mechanical properties while minimizing distortion, residual stress, and safety risks. [1]

After the Introduction chapter, the literature review is presented in Chapter 2, providing an overview of the relevant research and studies conducted in the field of welding and additive manufacturing. Following the literature review, the simulation chapters are presented, outlining the simulation models for submerged arc welding (SAW) and wire and arc additive manufacturing (WAAM) processes. These chapters include detailed descriptions of the models, as well as the comparison of the simulation results with experimental data. This allows for an evaluation of the accuracy and reliability of the models. Finally, the conclusions and future work are presented.

Chapter 2: Literature review

2.1 Welding Process

Welding is a process that joins two or more pieces of metal or thermoplastics by heating the surfaces to their melting points and then applying pressure to fuse them together. In this study, the specific type of welding being discussed is fusion welding. The fusion welding process involves heating two or more pieces of metal to their melting temperature, which causes the metal to fuse together. The melted metal then solidifies and creates a strong bond between the pieces, fusing them together. The heat for fusion welding is generated through external means, such as electricity or gas.[3]

Arc welding is a type of fusion welding in which an electric arc is used to melt the metal. The arc is generated by an AC or DC power supply, making the process fast and efficient. However, this method can also generate smoke and spatter as a result of the high heat generated. To prevent this, shielding gas or slag is often used to protect the weld from contamination by the surrounding atmosphere, which can cause the metal to react chemically with oxygen and nitrogen. [4] Overall, arc welding is a powerful and efficient method of welding, but it requires proper protective measures to ensure a high-quality weld.

Two different welding processes are simulated in this work. The first one is submerged arc welding (SAW), representing the simulation of the welding process. The other is gas metal arc welding (GMAW), the method used for the wire and arc additive manufacturing process. Simulating two different welding processes allows for a comprehensive comparison and understanding of the capabilities of the Additive Manufacturing Modeler in ABAQUS. It is also possible to understand the limitations and advantages of the software and to identify potential areas for improvement.

2.1.1 Submerged arc welding (SAW)

Submerged arc welding (SAW) (Figure 2-1) is a type of arc welding that utilizes a continuously fed consumable electrode. The electrode and the arc are covered by a layer of molten slag and granular flux, which protects the electrode and the weld from the atmosphere and creates clean welds. [5] However, this feature limits the flexibility of the SAW process. It is primarily used for flat and horizontal welding positions but is unsuitable for vertical or overhead welding positions[6]. It is used in production to produce spiral welded pipe.

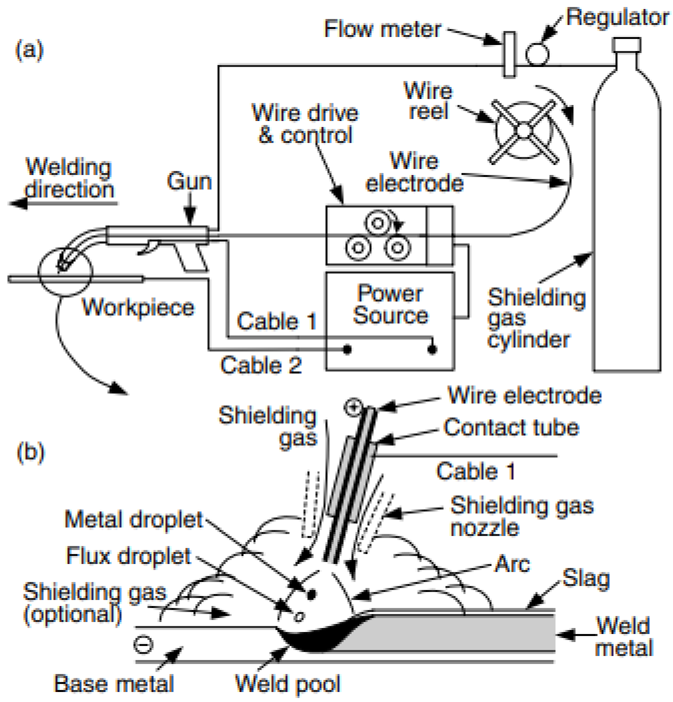

Figure 2-1: Schematic of S.A.W. Equipment Layout & Process[5]

The temperature measurement of the bead during the welding process can be therefore challenging when slag and flux are present on the surface.

2.1.2 Gas metal arc welding (GMAW)

In general, the heat source used in WAAM can be one of three types: gas metal arc welding (GMAW), gas tungsten arc welding (GTAW), or plasma arc welding (PAW). GMAW is the one used in this research, which is a widely used method in the manufacturing industry.

As shown in Figure 2-2, the heat is generated by an electric arc. The process is performed without applying pressure and utilizes a wire electrode that is fed through the welding gun, along with shielding gas [7]. The shielding gases are often Argon, Helium, and their mixture. In some cases, CO_2 can also be used as a shielding gas. The use of shielding gases in GMAW helps to protect the weld from oxidation and other atmospheric contaminants. [8]

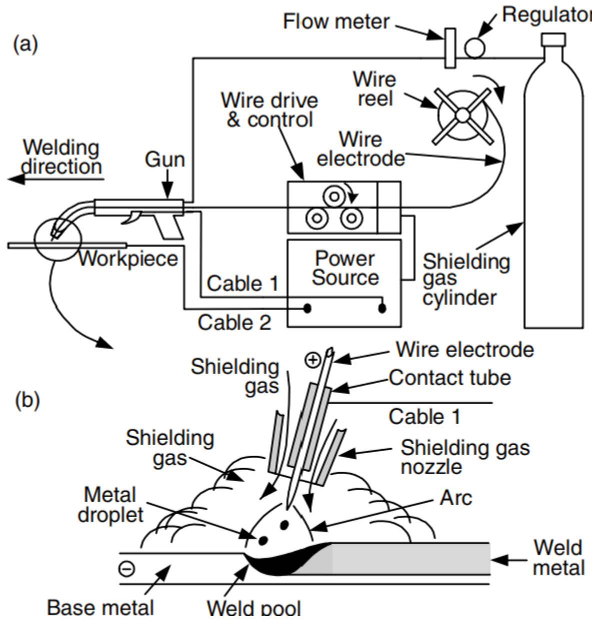

Figure 2-2: Schematic of GTAW Equipment Layout & Process[8]

GMAW is a high-speed welding technique that works well for both large-scale Manufacturing and repair. Additionally, the procedure is popular in the manufacturing industry due to its adaptability and high-quality welds. It can be used to weld a variety of metals, including steel, aluminum, and stainless steel, as well as in flat, horizontal, vertical, and overhead locations.[7] It is a standard process used for girth welding of steel pipe in pipeline construction.

2.2 Treatment of convection in the weld pool

The treatment of convection in the weld pool refers to the methods used to control and manipulate the movement of the molten metal in the weld pool during the welding process. Convection is the natural movement of the molten metal in the weld pool due to heat transfer and the buoyancy effect. If not properly addressed, this movement can lead to issues such as porosity, lack of fusion, and poor penetration. In 2013, a mathematical model was developed to consider convection and temperature distributions in moving weld pools driven by buoyancy, electromagnetic and surface tension forces. [9] This model provides a better understanding of the forces that drive the movement of the molten metal in the weld pool and helps to improve the accuracy of predictions and simulations of the welding process.

For arc welding processes, the use of a gas shield is often employed to help control the movement of the molten metal in the weld pool. Additionally, in Submerged Arc Welding (SAW), the flux blanket used in the process also helps to control the movement of the molten metal by creating a protective barrier around the weld pool, reducing the effects of convection.

2.3 Temperature measurement methods

During the welding process, several methods can be utilized to measure temperature. Three of the most commonly used methods are contact thermocouples, infrared cameras and pyrometers.

Contact thermocouples are temperature sensors composed of two metal wires joined together at one end, known as the "hot junction." The other end of the thermocouple is connected to a measuring instrument, such as a thermocouple meter. An electrical voltage is generated when there is a temperature difference between the hot junction and the measuring instrument. This voltage can be measured and used to determine the temperature at the hot junction.[10]

One of the main advantages of using contact thermocouples is that they are relatively inexpensive and easy to install. They are also versatile, as they can measure temperature in solids, liquids, and gases. Contact thermocouples are also suitable for harsh environments, such as high temperatures, pressure, vibration, and corrosive conditions. They are commonly used in industrial applications.

The results obtained from the first model in this work were compared with experimental measurements conducted by Lecoanet[1] in his research. As shown in Figure 2-3, three sets of three horizontal holes were drilled to insert thermocouples into the substrate at positions close to the weld metal. Each set of holes was drilled at different depths, and in each set, two type K thermocouples and a type B thermocouple were inserted. For K-type thermocouples, the metal wires are usually iron and constantan; while for B-type thermocouples, they are often made by platinum-30% rhodium and platinum-6% rhodium. The B-type thermocouples have a larger range than the K-type thermocouples. However, the researcher noted that this method might not provide entirely accurate measurements. This is due to slight movements of the thermocouple during the welding process may lead to incorrect results since the thermal gradients experienced in welding near the weld metal are very high. Other limitations of this method include potential issues with the insulation of the thermocouple wires and incorrect placement of the thermocouples, which can result in heat loss and inaccurate temperature readings.

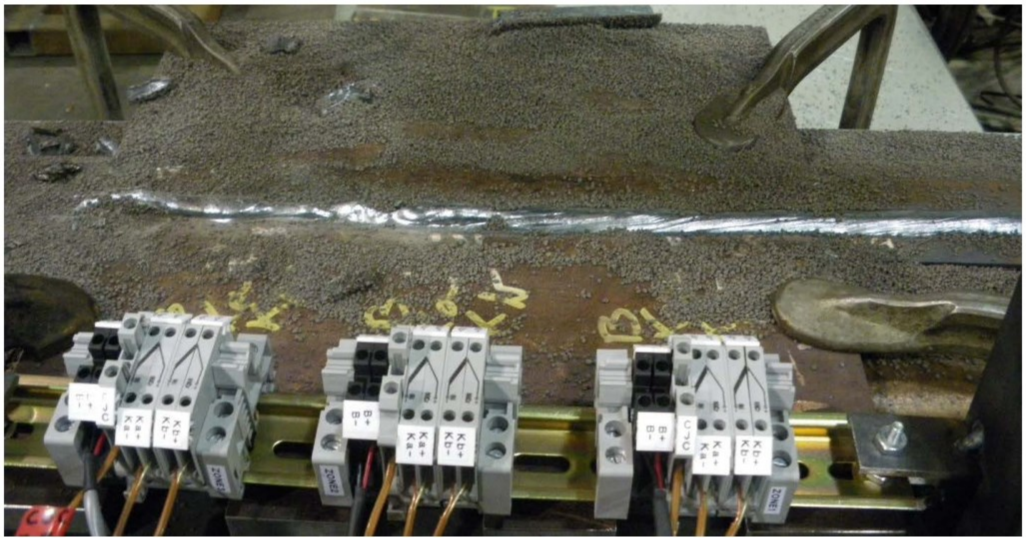

Figure 2-3: Weld performed with eight thermocouples embedded in the plate [16]

Another technique used in this work for temperature measurement is non-contact pyrometry. This method measures the temperature of an object by sensing its electromagnetic radiation without making physical contact with it. This approach is particularly useful for objects that are difficult to reach, in motion, or for situations where direct contact is not feasible due to safety or sanitation concerns. As a result, it is widely used in the welding process and other industrial applications. [11]

There are several types of pyrometers, such as infrared pyrometers, laser pyrometers, Optical pyrometers and two-colour pyrometers. The two-colour pyrometers are used in the experiment of the WAAM part in this research, which uses the principle of the ratio of two radiation intensities emitted by the object being measured to determine the temperature. The advantage of this type of pyrometer is that they are not affected by variations in emissivity, which can cause inaccuracies in other types of pyrometers. [12] They are also suitable for high-temperature environments, such as molten metals or furnaces. It was used to measure the temperatures on the weld line in this study.

An infrared camera is a device that detects and captures infrared radiation, which is electromagnetic radiation with a wavelength longer than visible light. It detects temperature differences and creates images based on that information. In 2010, Chokkalingham [13] developed a computer-controlled Gas tungsten arc welding (GTAW) machine with an IR camera mounted on the torch assembly for real-time monitoring of the weld pool during the GTAW. Later in 2012 [14], he presented a method for monitoring weld quality by estimating the bead width and depth of penetration using infrared sensing. The IR camera extracted features such as the length and width of the hot spot, peak temperature, etc. Then they were used as inputs for the neural network models, with the measured bead width and depth of penetration as the outputs. The previous research shows their capacity to monitor the temperature of industrial processes. It is a suitable temperature measurement method that can be used in future work.

2.4 Material

The material used in the SAW study is X70, while 17-4 PH material was utilized in the WAAM study.

2.4.1 X70

X70 is pipeline steel with high strength and low alloy. Its ability to withstand high pressure and temperature makes it an ideal choice for pipeline transportation, such as oil, natural gas and other pipelines.[15] The "X" in its name refers to the high-strength characteristic, while the number "70" indicates that the minimum yield strength is 483MPa (70kpsi). There are various types of X70 steel, which have different chemical compositions, mechanical properties, and applications. The composition and the thermo-physical properties in the model are the same as what was used in Lecoanet's[1] experimental work, which is shown in Appendix A.1.

2.4.2 17-4 PH

In the research on WAAM, the plate used for both the experiments and the simulation is made from a 17-4PH plate. The "17-4" in the name refers to the composition of the steel, which includes 17% chromium and 4% nickel. The "PH" stands for "precipitation hardening," a heat treatment process used to increase the strength and hardness of the alloy. The process involves heating the material to a specific temperature, then cooling it rapidly. This causes small, hard precipitates to form within the alloy, increasing strength and hardness. These features make it a cost-effective replacement for high-strength carbon steel and other stainless grades. This type of stainless steel is commonly used in aerospace and defence applications, as well as in the oil and gas industry and other high-stress applications.[16]

2.5 Wire and arc additive manufacturing (WAAM)

2.5.1 Additive Manufacturing (AM)

Additive Manufacturing, also called 3D printing, is a process of creating a physical object from a digital model, layer by layer. The material is usually plastic or metal and is typically supplied as a filament, powder, or liquid.

The 3D printing technologies were almost conceived during the same period in the 1980s by several independent investors, such as Hideo Kodama at the Nagoya Municipal[17], Alain Le Méhauté, Olivier de Witte, and Jean Claude André of the French General Electric and CILAS companies[18]. The first practical application of AM, marked as the beginning of the modern 3D printing industry, was filed in 1984 and 1986 by Chuck Hull[19], who developed the technology known as Stereolithography (SLA). SLA involves using a laser to cure a liquid resin into a solid object, layer by layer.

In the 1990s, several other additive manufacturing technologies were developed, including Fused Deposition Modeling (FDM) and Selective Laser Sintering (SLS). FDM, developed by Scott Crump, uses a heated nozzle to melt and extrude a plastic filament, while SLS, developed by Carl Deckard, uses a laser to fuse small particles of metal or plastic powder. These technologies, along with SLA, became the primary additive manufacturing methods used in industry and research[20]. As technology progressed, new materials and advanced capabilities emerged, significantly expanding 3D printing applications in various industries such as aerospace, automotive, medical, dental and consumer products.

2.5.2 Wire and arc additive manufacturing (WAAM)

Wire and arc additive manufacturing (WAAM) uses a wire feed and an electric arc to melt and deposit metal material layer by layer onto a substrate to create a 3D object (shown in Figure 2-4). It is a type of AM and is a recent technology.

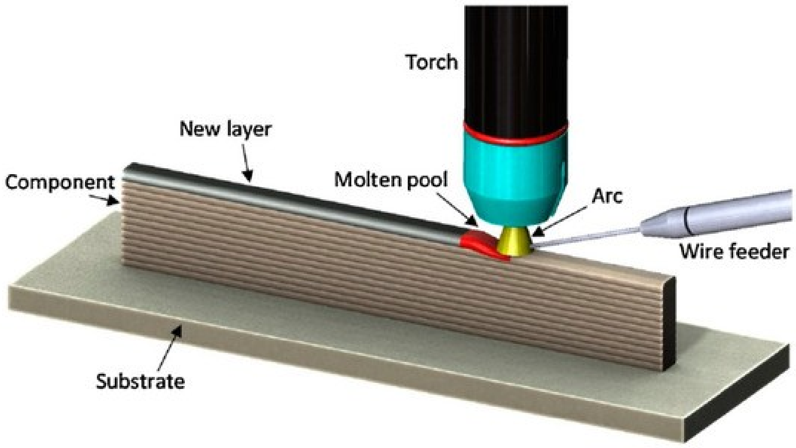

Figure 2-4 Diagram of WAAM process. [21]

Although WAAM (Wire and Arc Additive Manufacturing) had appeared in some research before the 1990s, it was not until the 2000s that it was truly defined and widely developed. In 2005, a research team at the Fraunhofer Institute for Laser Technology (ILT) in Germany laid the foundation for the development of WAAM as we know it today. Many analytical models [22-24] were then developed to predict the bead geometry, including bead height and width for a single weld bead. The analytical prediction of the temperature profile in WAAM utilizes similar principles to those used in welding. To accurately predict the temperature profile, it is necessary to use a finite element method, which will be discussed in the next section of the chapter.

The success of the process depends on a variety of variables, such as material properties, wire feed rate, arc voltage, travel speed, wire type and diameter, shielding gas, environmental conditions, and post-processing methods. Gu, Jiang Long, et al. [25] indicate that the quality and characteristics of the wire, both internally and externally, play a significant role in determining the performance of parts. Wire feed rate, travel speed, and gas flow rate can significantly affect the bead geometry and cooling rates [26][27]. There are also studies [28] that showed that adjusting the heat input can lead to improvements in the macrostructure, microstructure, and mechanical properties of the fabricated parts. These variables must be carefully controlled and monitored to ensure that the final product meets the desired specifications. A prediction that takes into account all of the necessary factors is, therefore, an important step to further develop the WAAM technology.

In this research, two key areas of study are temperature history and solidification cooling rates. Here, the study focuses more on solidification cooling rates because it is an important parameter affecting the final shape and the dimensional accuracy of the deposited material. Another commonly used cooling rate is called cooling rate 8/5, which is the cooling rate from 800 °C to 500 °C in a weld bead and its heat-affected zone.

The temperature significantly impacts the shape and size of the weld bead, and the solidification cooling rate can be used as a monitoring tool to analyze and control geometrical parameters [29]. These factors are crucial not only in understanding the geometrical characteristics of the weld but also in analyzing the microstructure of the weld. Furthermore, they play a crucial role in the study of inter-pass temperature and future research on multi-pass WAAM.

2.6 Simulation

2.6.1 Prediction of the thermal effect

Before Rosenthal's research [30], most solutions for this problem were too complex for practical application. Rosenthal developed a mathematical model known as the Rosenthal equation to predict the heat transfer between the molten pool and the base metal. According to him, the analytical solution for a quasi-steady state in a semi-infinite geometry for a point source is:

$$T = T_{\infty} + \frac{\lambda P}{2\pi k r} exp\left[-\frac{v(r+\xi)}{2\alpha}\right] \tag{2-1}$$

Where P is the power of the heat source, v is travel speed, and α is the thermal diffusivity. ξ the moving coordinate, and r is the distance from the heat source.

This model was later improved by Rykalin's equation [31], which is a summary of the fundamental equations of heat conduction for welding applications. However, the Rosenthal and Rykalin equations have limitations in that they are one-dimensional models and can only predict the temperature distribution far from the heat source. Eager and Tsai [32] developed an analytical solution based on the research of Rosenthal [30] and Rykalin [31], where they created an analytical solution for the temperature distribution using a two-dimensional surface, Gaussian distributed heat source. This improved the temperature predictions, but it is limited in its ability to predict penetration. To fully understand the temperature distribution during welding, three-dimensional heat source models are necessary. However, though there is an analytical solution for the transient temperature field of a semi-infinite body subjected to a three-dimensional power density of a dynamic heat source developed by Nguyen et al. [33], it does not take into account convection and radiation. Therefore, if a 3D heat source model is to be utilized, analytical solutions alone may not be sufficient and numerical methods such as finite element analysis should be used, as discussed in a later section of this chapter.

2.6.2 Goldak heat source

In order to model any welding process, the size and shape of the weld pool (the heat source) need to be quantitatively defined as a function of the heat input. In the simulation part of this research, a Goldak heat source distribution is used. In the 1980s, Goldak developed a comprehensive mathematical model for a 3-D, moving double ellipsoidal heat source commonly used in welding. This model makes it possible to accurately calculate the thermal history of the welded plate and provide detailed 3D simulations of the welding process. The model considers the shape, size and position of the heat source, as well as the material's thermal properties. Goldak used advanced techniques such as finite element analysis (FEA) and computational fluid dynamics (CFD) to simulate heat transfer during the welding process and predict the temperature distribution. Goldak also validated the results obtained from the model with experimental. This model provides a theoretical understanding of the heat transfer phenomena that occur during welding, which can be useful for optimizing welding processes and predicting the resulting microstructure of the welded material. [34,35]

The illustration in Figure 2-5 represents the Goldak model, which depicts the heat source as two mutually perpendicular ellipsoids. The semi-axes of the ellipsoidal molten pool in the x and y directions are represented by a and b, respectively, while c_f and c_r represent the length of the front and rear parts of the estimated molten pool.

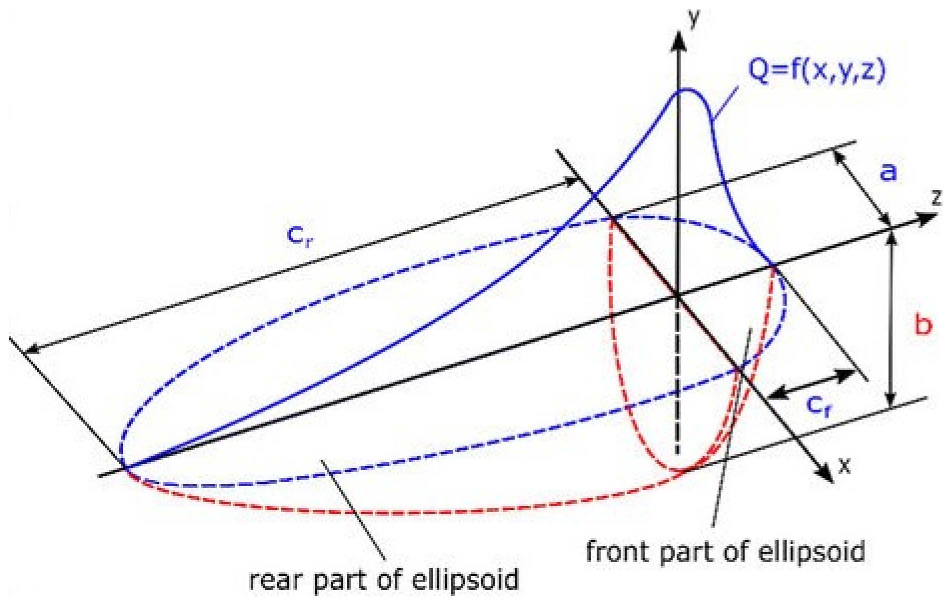

Figure 2-5: Schematic diagram of Goldak model presented in (Kik) [36]

The double ellipsoidal power density distributions are shown in Equations 2-2 and 2-3. The power density distribution inside the front part of an ellipsoid is written as follows:

$$Q(x,y,z,t) = \frac{6\sqrt{3}f_f q}{abc_f\pi\sqrt{\pi}} exp\left[-3\left(\frac{x^2}{a^2} + \frac{y^2}{b^2} + \frac{(z-vt)^2}{c_f^2}\right)\right] \tag{2-2}$$

In the rear part of an ellipsoid, the power density distribution is:

$$Q(x,y,z,t) = \frac{6\sqrt{3}f_r q}{abc_r\pi\sqrt{\pi}} exp\left[-3\left(\frac{x^2}{a^2} + \frac{y^2}{b^2} + \frac{(z-vt)^2}{c_r^2}\right)\right] \tag{2-3}$$

Obtaining the parameters a, b, c_f, and cr in the Goldak model can be done through experimental analysis of the fusion zone during the welding process. One method is to use sensors, such as infrared cameras, to measure the temperature distribution in the fusion zone. The model's parameters can then be modified based on the information gathered from the experiment to produce the desired melted zone under the appropriate welding conditions.

f_f and f_r are the fractions of deposited heat in the front and rear of the ellipsoids. They are written as:

$$f_f = \frac{2c_f}{c_f + c_r} \tag{2-4}$$

$$f_r = \frac{2c_r}{c_f + c_r} \tag{2-5}$$

Following Goldak's model, Kemph [37] demonstrated that the temperature distribution during welding could be accurately calculated using Green's function approach. Roshyara [38] proposed another approximate analytical method using the Laplace transform method. Both Kemph's [37] and Roshyara's [38] research improved the understanding of the heat transfer phenomena that occurred during welding and expanded the capabilities of Goldak's model, making it possible to predict the thermal history of the welded plate and provide detailed 3D simulations of the welding process with no size limitations.

In 1996, a study [60] presented a computational analysis for the precise prediction of heat transfer, fluid flow, and phase change during welding with a moving heat source, which resembles the Goldak heat source. This previous research mentioned that the solution for such a process requires a large number of grids to ensure the accuracy and stability of the solution. Additionally, a small time step is essential. As a result, the computation time becomes significantly large. Therefore, the present study simplifies the fluid flow in the molten pool by representing it in the thermal-physical properties, such as thermal conductivity, which is increased by a factor of five compared to its normal value.

2.6.3 Thermal efficiency

In welding, thermal efficiency is the measure of how effectively the energy from the welding arc is used to fuse the metal. It is a proportion of the energy that reaches the workpiece to form the weld to the energy supplied by the welding arc. The efficiency of the welding process can be affected by factors such as the type of welding being used, the size and shape of the weld, the quality of the materials being welded, and the ambient conditions. [39]

SAW has very high thermal efficiency as the flux layer completely covers the arc. In this work, the efficiency is 95%. As for GMAW, the efficiency is lower due to the heat being spread over a larger area. The heat source used in the WAAM process of this work has an efficiency of 85%.

2.6.4 Finite element method (FEM) and finite element analysis (FEA)

The finite element method (FEM) is a numerical technique for solving differential equations, typically used in engineering and physics. It involves breaking down a complex system or structure into smaller, simpler elements and solving for the behaviours of each element independently. Then, these behaviours are combined to provide the system's overall behaviour. Finite element analysis (FEA) uses the FEM to analyze a system or a structure, which means it is the application of FEM to a specific problem. To predict temperature fields in a 2D or 3D space, advanced numerical methods such as finite element analysis (FEA) are needed. They can provide details of the welding process and WAAM process, considering the complex geometry of the system, the heat transfer mechanisms, and the material properties.

2.6.5 FEM and FEA for welding

Before the invention of FEA or FEA, many researchers developed simplified models to predict temperature distribution during welding. However, the models were limited to accurately predicting the behaviour of real welding processes. During the year 1990s, with the development of more powerful computers, the method started to show its advantages, making it possible to simulate more complex welding processes using two and three-dimensional models.

Many software programs have been created for doing FEA. Weld simulation uses common software like ANSYS, ABAQUS, COMSOL and SYSWELD. While SYSWELD is specifically made for welding and heat treatment processes, ANSYS and ABAQUS both require significant subroutine programming.

In recent years, many studies on the welding process using FEA have been developed. For example, in 2009, Akbari et al. [40] used finite element techniques (also software ANSYS) to analyze the thermo-mechanical behaviour and residual stresses in dissimilar butt-welded pipes. Shanmugam et al. [41] used the finite element code SYSWELD and a few FORTRAN subroutines to predict the bead geometry in laser welding. A new analytical model with COMSOL has been used to predict the temperature distribution during plasma arc welding of thin Ti-6Al-4V sheets [42].

As for the simulation on SAW, a 3D transient FEA of heat transfer in SAW has been done by ANSYS to predict the different zones of microstructures [43]. Lecoanet [1] used COMSOL to predict the temperature profile in a SAW and to estimate the welding parameters. An X80 pipeline steel welded joint's twin-wire SAW welding temperature distribution was analyzed in 2018 using ANSYS. In order to simulate the deposition of weld metal, the element birth and death approach was also used[44].

Different from the software mentioned above, ABAQUS is the simulation tool in this research. It has a wide range of built-in material models and can simulate multi-physics problems, such as thermal-mechanical interactions and large deformation, which are important for accurate welding simulation. There are also some simulations done by ABAQUS previously: A multi-wire SAW process was modelled in 2001 [45], and it explained the welding process and its application in thick wall line pipe manufacturing briefly. In 2013, a new practical approach was proposed by modifying thermal conductivity to predict the thermal history [46]. Both 2D and 3D finite element models are developed using the solution of heat transfer equations in ABAQUS Standard implicit by Nezamdost, M. R., et al. in 2016 [47].

Today, FEA is widely used in the welding industry to predict the behaviour of welding processes. It makes the process more straightforward and simplifies the procedure, and has significantly improved both the process's efficiency and quality. It is now an essential tool for many welding engineers and researchers.

2.6.6 FEA for WAAM

The development of FEA for WAAM has been an ongoing process, with advancements in both the FEA software and the understanding of the WAAM process. At first, FEA was only used to predict the temperature distribution in the WAAM process for simple heat transfer models, such as steady-state or transient heat conduction, which is not accurate for the real process. Later, more complex models were developed to take into account the effects of the electric arc. In recent years, more advanced models have been developed. For example, the thermo-physical properties of the materials can be considered so that the model can predict the thermal and mechanical behaviour of the WAAM process simultaneously.

In 2017, a study was conducted to establish a model for simulating the substrate preheating temperature and thermal process in the GMAW-based AM process for circular thin-walled parts [48]. The study used the software MSC MARC. The research provided valuable insights and precautions on preheating of substrate preheating to the simulations in this study. There is also a study that used ABAQUS to predict the thermal and mechanical effects during a moving heat source of Tungsten Inert Gas (TIG) welding of Ti–6Al–4V alloy plate. The research aimed to understand the thermal and mechanical behaviour of the process by simulating the temperature distribution across the welding line and weld bead geometry at different welding currents. The prediction was found to have an excellent agreement with the experimental data of TIG welded joints.[49] These studies demonstrate the capability of using FEA to simulate the temperature distribution during the WAAM process and the potential of using ABAQUS to optimize the process.

2.6.7 Additive Manufacturing Modeler in Abaqus

The plug-in additive manufacturing modeler in Abaqus is a new tool that simulates and analyzes the AM process [50]. The analysis type can be thermal, structural or thermal-structural. The plug-in can be used to optimize the build process and reduce the likelihood of defects or failures in the printed parts. This tool simulates the deposition of material layer by layer and considers factors such as material properties, thermal effects, and build orientation to accurately predict the behaviour of the final printed part. It can also take into account the conditions like heat input, travel speed, and heat transfer, including conduction and convection and surrounding conditions. These features also make it possible to simulate the welding process. The difference between AM and the welding process is that AM is designed to simulate the layer-by-layer build process of 3D printing, while welding is to fuse two or more parts together. That is the precaution that needs to be taken when using AM modeler to simulate welding.

As shown in Figure 2-6, the AM modeler has three different sections: Data Setup, Model Setup and Simulation Setup, of which the Data Setup is most extensive. In the Data Setup section, the material properties, power and deposition information, toolpath data, and other input data needed for the simulation are input. Model Setup section to create the finite element model of the part, including the mesh and boundary conditions. The Simulation Setup section includes the type of analysis, time step, and solver settings. The load and boundary conditions can also be defined here.

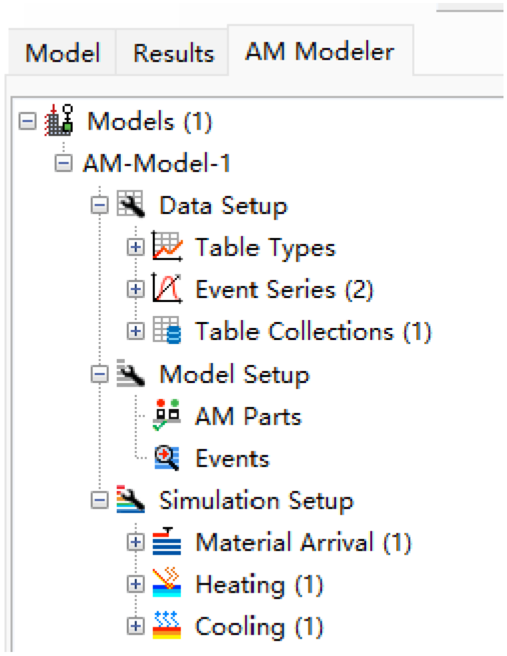

Figure 2-6: AM Modeler in ABAQUS.

To model the welding or WAAM processes, much previous research worked on user subroutines or the MODEL CHANGE option in ABAQUS. With these methods, gradual activation of different elements is required, so multiple steps need to be used. When simulating AM processes, the amount of material needed to be added is often more extensive than a welding analysis, making the model more computationally intensive and time-consuming [51]. Therefore, it is limited in some cases, such as multiple moving heat sources or multiple layers.

In 2020, a study by Song, Xu et al. [52] investigated the residual stresses and distortion in Laser-directed energy deposition (LDED) and Selective Laser Melting (SLM) processes. The study focused on modelling thin-walled components for LDED processes and comparing the predicted residual stresses with measurement results. Additionally, the study simulated overhanging structures with varying support thicknesses for the SLM process and compared the results with an experimental part. In 2021, a study by Mena, Edison A [51] utilized the ABAQUS AM modeler to simulate a Directed Energy Deposition (DED) process. The study employed the automated interface provided by the AM modeler to prescribe the toolpath and process conditions. The AM modeler was used to properly define the necessary data straightforwardly to approximate the 3D printing layer-by-layer build-up process. The toolpath-mesh intersection module was integrated with the created Event Series to simulate the layering process, which is crucial for the DED process.

The ABAQUS AM Modeler plug-in has recently undergone a number of modifications. The most recent version of 2022 now completely includes AM process simulation features. New features for simulating AM are still being developed and added to the software. A pattern-based method for thermomechanical studies of AM processes using powder beads and modelling of metallurgical phase transformations are also included in the most recent release [53]. In the new version, the available analysis types include Eigenstrain, which is available in both trajectory-based and pattern-based methods, Thermo-mechanical, which is available in powder-bed with trajectory-based and pattern-based options; LDED and FDM.

ABAQUS is widely acknowledged as a leading tool for simulating AM or 3D printing processes. Its AM Modeler plug-in, with its advanced features and capabilities, allows for accurate and convenient simulation of AM or welding processes. Utilizing the AM Modeler in ABAQUS allows researchers to stay current with the latest advancements in the field of additive manufacturing (AM) and enables them to optimize and enhance their research studies.

2.7 Summary

The use of AM Modeler in ABAQUS to construct a 3D model incorporating a moving heat source and taking into account all heat transfers is an under-explored area. This new methodology has the potential to be a highly effective tool if used correctly. This research aims to leverage this new approach to accurately predict the thermal history of welding and additive manufacturing processes.

Chapter 3: Modelling of the thermal history in submerged arc welding (SAW) using Abaqus.

3.1 Introduction

Submerged arc welding (SAW) is a welding process where an arc forms between a consumable wire electrode and a base metal workpiece. The arc is shielded by a granular flux which insulates the weld. A flux hopper supplies the flux, and the wire is continuously fed by a wire reel. This process is efficient because of its high deposition rate.

Due to the fact that the flux submerges the arc during the welding process, it becomes impossible to measure the temperature close to the weld using traditional means such as an infrared pyrometer. To overcome this limitation and accurately predict the temperature profile, an Additive Manufacturing modeler in Abaqus is employed. This modeler utilizes advanced simulation techniques to predict the temperature profile of the plate during the welding process, allowing for greater precision and control in the manufacturing process. Based on the research by Lecoanet [1], a new finite element modelling package for additive manufacturing simulation was implemented in Abaqus.

3.2 Governing equations

In the previous research of Lecoanet [1], conduction is the only heat transfer mode considered. The fluid flow in the weld pool was not studied. The differential equation of the element in a homogenous plate can be written from an energy balance:

$$(\dot{q}_x - \dot{q}_{x+dx}) + (\dot{q}_y - \dot{q}_{y+dy}) + (\dot{q}_z - \dot{q}_{z+dz}) + \dot{q}_{gen} = \frac{dE}{dt} \tag{3-2}$$

The directions of the X, Y, and Z axis are shown in Figure 3-1. The first three terms on the left side are the difference in the rate of heat conduction at the positions x, y, z and at x+dx, y+dy, z+dz. The last term is the rate of heat generation of an element. On the right side of the energy balance is the rate of change of energy content of the element.

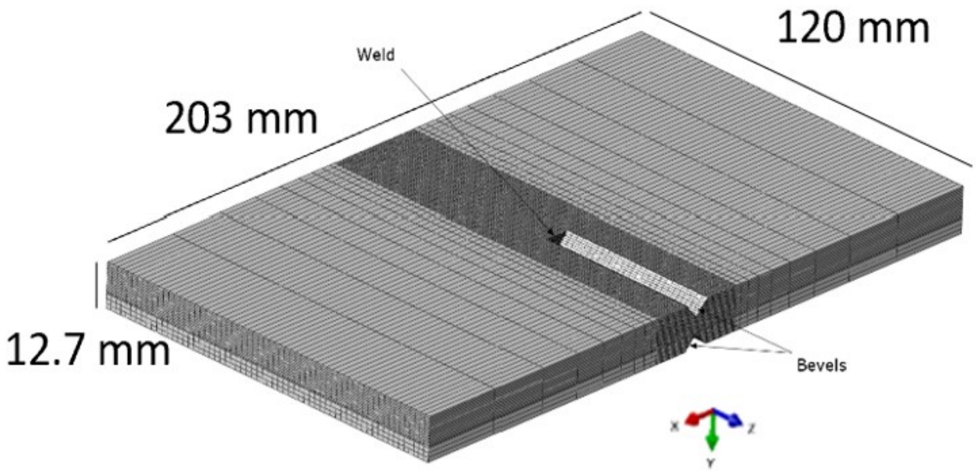

Figure 3-1: Geometry of the plate.

In Equation 3-1, the change in the rate of heat conduction can be expressed as follows:

$$\dot{q}_x - \dot{q}_{x+dx} = -\frac{\partial}{\partial x}(q_x) \cdot dx \tag{3-2}$$

Then,

$$\dot{q}_x - \dot{q}_{x+dx} = -\frac{\partial}{\partial x}(-k(dy \cdot dz)\frac{\partial T}{\partial x}) \cdot dx \tag{3-3}$$

Finally,

$$\dot{q}_x - \dot{q}_{x+dx} = \frac{\partial}{\partial x}(k\frac{\partial T}{\partial x})(dy \cdot dz \cdot dx) \tag{3-4}$$

The same for the other two directions:

$$\dot{q}_y - \dot{q}_{y+dy} = \frac{\partial}{\partial y}(k\frac{\partial T}{\partial y})(dx \cdot dz \cdot dy) \tag{3-5}$$

$$\dot{q}_z - \dot{q}_{z+dz} = \frac{\partial}{\partial z}(k\frac{\partial T}{\partial z})(dx \cdot dy \cdot dz) \tag{3-6}$$

The rate of heat generation inside the element is written as:

$$\dot{q}_{gen} = Q \cdot dx \cdot dy \cdot dz \tag{3-7}$$

The right side of the energy balance is:

$$\frac{dE}{dt} = \rho dV \cdot c_p \cdot \frac{dT}{dt} \tag{3-8}$$

From Equations 3-4 to 3-8, the energy balance becomes:

$$\frac{\partial}{\partial x}(k\frac{\partial T}{\partial x}) + \frac{\partial}{\partial y}(k\frac{\partial T}{\partial y}) + \frac{\partial}{\partial z}(k\frac{\partial T}{\partial z}) + Q = \rho c_p \frac{\partial T}{\partial t} \tag{3-9}$$

In order to ensure that the simulation reflects the actual movement of the heat source and the geometry of the process being simulated, it is necessary to make adjustments to the variables involved in the simulation. [1]

As the heat source moves in the direction of Z, a function of time can be written as:

$$z = vt \tag{3-10}$$

The derivative of z is obtained by Equation 3-10.

$$\frac{\partial z}{\partial t} = v \tag{3-11}$$

Also,

$$\frac{\partial T}{\partial t} = \frac{\partial T}{\partial z} \cdot \frac{\partial z}{\partial t} \tag{3-12}$$

Substituting Equation 3-11 into 3-12,

$$\frac{\partial T}{\partial t} = v \cdot \frac{\partial T}{\partial z} \tag{3-13}$$

By combining Equation 3-9 and Equation 3-13, the final equation, represented by Equation 3-14, is obtained.

$$\vec{\nabla} \cdot \left(k\vec{\nabla}(T)\right) + Q - \rho c_p v \frac{\partial T}{\partial z} = 0 \tag{3-14}$$

3.3 Simulation Description

In this section, the details of the simulation are provided. The geometry of the simulation is illustrated in Figure 3-1. The thermophysical properties of the materials involved in the process are then discussed. Following that, the boundary conditions and the design of the mesh are explained. Finally, a comprehensive overview of the Additive Manufacturing Modeler in Abaqus is provided.

3.3.1 Geometry

As shown in Figure 3-1, the plate is 203 mm long, 120 mm wide, and 12.7 mm tall, with bevels that have a depth of 4mm and a width of 8mm (Figure 3-2)

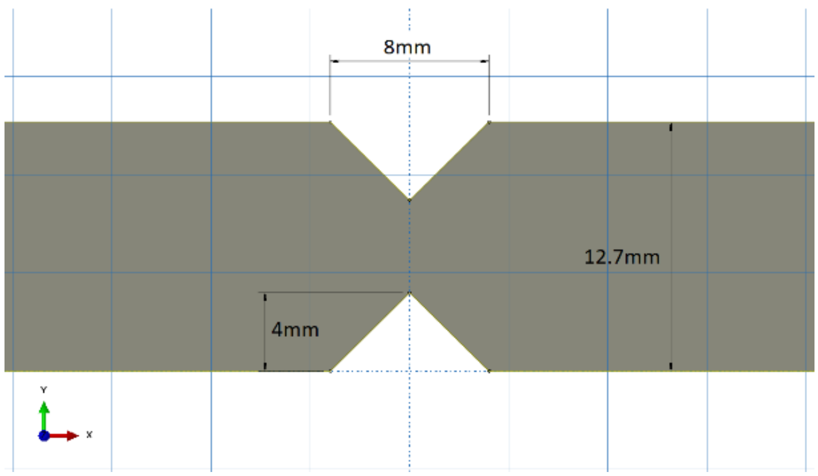

Figure 3-2: Geometry of the bevels.

3.3.2 Thermo-physical properties

In this simulation, the material used is X70 micro-alloyed steel. The thermophysical properties of the material are based on the research of Alexandre Lecoanet [1], which considers that the properties of the material vary with temperature. The liquidus temperature and solidus temperature of X70 steel are 1510°C and 880°C, respectively. Additionally, the density, specific heat, and thermal conductivity of X70 steel are also taken into account for the simulation. These properties are essential for an accurate prediction of the temperature profile. The calculation methods' details have already been shown in Lecoanet's work[1]. The details are represented in Appendix A.1. SI-mm units are used in the new Abaqus model. Hence a change in the system of units is required.

3.3.3 Initial and boundary conditions

The initial conditions for the simulation are related to the temperatures. The ambient temperature is set to 20˚C, representing the surrounding environment's temperature. The initial temperature of the bead, which is the area where the material is deposited, is set to 1500˚C, which is close to the material's melting point. This is done to simulate the condition where the material is in a molten state when it is deposited into the bead. With the heat source passing, the elements on the bead get heated, and the temperature increases significantly. It is important to note that the elements are not deposited before the heat input passes, so temperatures before the deposition will not be recorded.

In order to make the simulation more realistic and better match the experimental conditions, the plate is given an initial temperature that simulates preheating. In general, the preheat temperature is between 120˚C to 200˚C. Preheating serves multiple purposes: it removes moisture and greasy residue that could negatively affect the melting pool and slows the cooling rate, resulting in a tougher joint that is less likely to crack. From the simulation perspective, preheating the plate prevents convergence problems in Abaqus. The large temperature difference between the bead and the plate can lead to issues in the simulation, such as an excessive number of attempts within a time increment or the time increment being smaller than the minimum specified value.

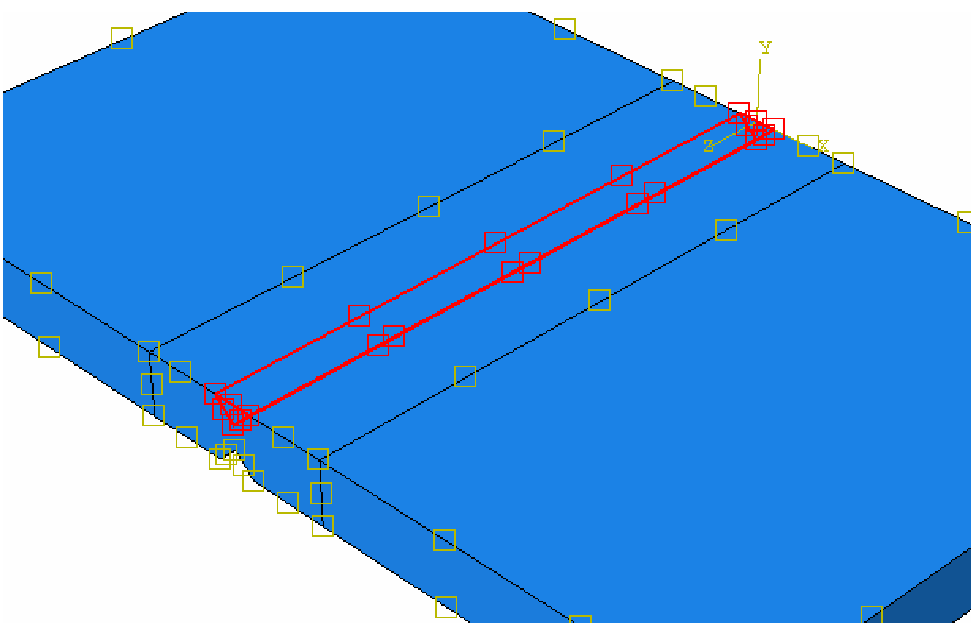

Figure 3-3: Selected part for initial bead temperature in Abaqus.

The design in the simulation for the initial temperatures is shown in Figures 3-3 and 3-4. The red part is the area selected in the model. The initial bead temperature should be set before the plate's preheating. The right picture in Figure 3-4 shows that the bead part is not red. It means that when preheating the plate, only the base metal part is selected

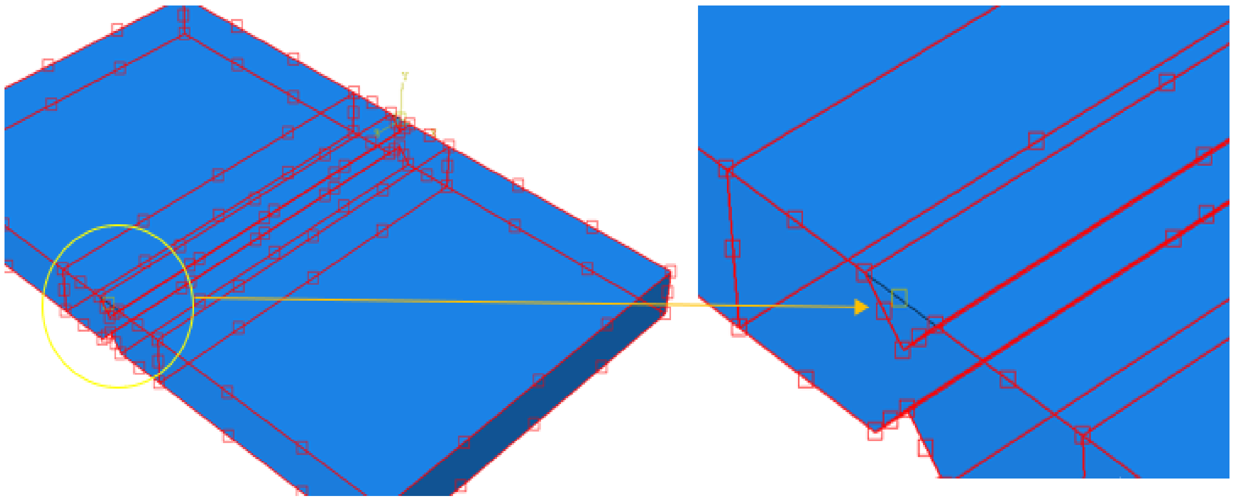

Figure 3-4: Selected part for the plate preheating in Abaqus.

As mentioned previously, in SAW, the arc is shielded by a layer of flux. So the effect of the radiation at the deposited surface is relatively smaller than conduction and convection. As a result, it is assumed that the radiation is 0 in the simulation. The convection on the bead is considered the same as that on the other surfaces. Minimizing the convection on the bead helps to achieve a high-quality weld.

Convection heat transfer is applied to the base metal in the simulation outside of the weld bead. Since the plate is surrounded by air, natural convection is applied on all surfaces of the plate except for the surface where the material is being deposited. The heat transfer due to convection is described by Newton's law of cooling, which states that the heat transfer rate is proportional to the temperature difference between the plate and the surrounding air and the heat transfer coefficient:

$$q_c = h(T - T_\infty)dSdt \tag{3-15}$$

The Fourier equation provides the conduction heat transfer that occurs at the solid's surface:

$$-k\frac{\partial T}{\partial n}dSdt \tag{3-16}$$

Equations 3-15 and 3-16 form the boundary condition of convection:

$$-k\frac{\partial T}{\partial n} = h(T - T_{\infty}) \tag{3-17}$$

In the Abaqus simulation model, the convective coefficient, h, is set to a value of 3W/(m^2K)[1]. There are two ways to incorporate these conditions in the software. One way is to use the Interaction Module and define the surface film condition. The other way is to define them in the Additive Manufacturing Modeler's Simulation Setup section. Both of these methods are able to produce the same results.

3.3.4 Mesh design

As shown in Figure 3-5a, the mesh size used in the simulation increases from the welding line toward the outer edge of the plate. This is because the region near the welding line is more affected by the welding process and requires more computational resources to simulate accurately. Using a smaller mesh size in this region increases the number of elements in the model and improves the accuracy of the results. The border of the plate, which is not as affected by the welding process, can use a coarser mesh size to reduce simulation time. However, the mesh size used in the bead or near the bevel should be as small as possible to ensure accurate results in these regions, as illustrated in Figure 3-5b. The mesh size on the bead is 0.5mm, and near the bead is designed to be 1mm. By carefully selecting the mesh size, the simulation can balance computational efficiency and accuracy to provide reliable results.

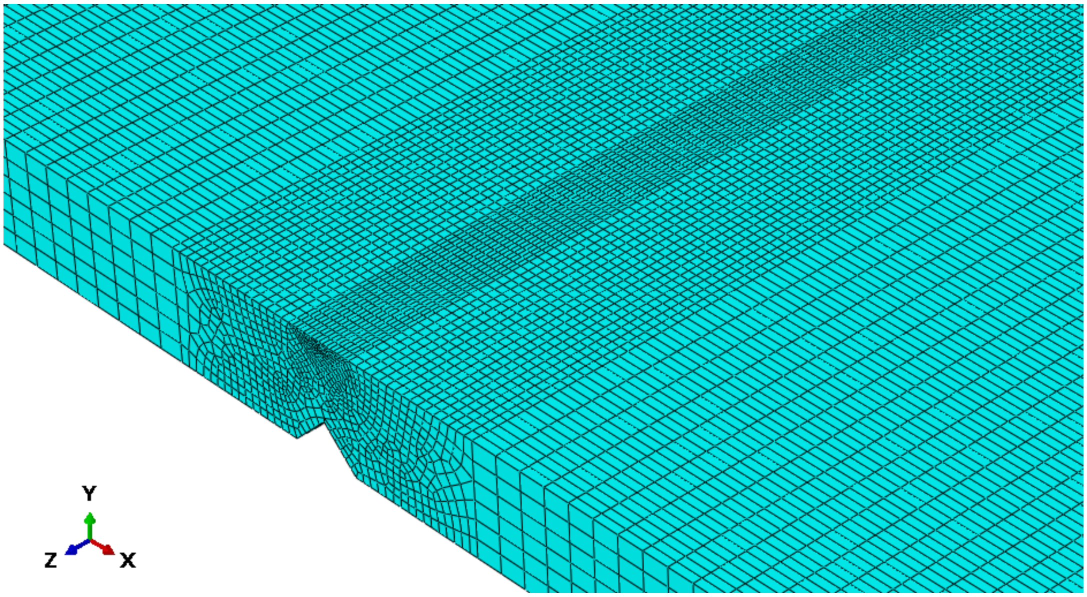

Figure 3-5a: Illustration of the mesh design.

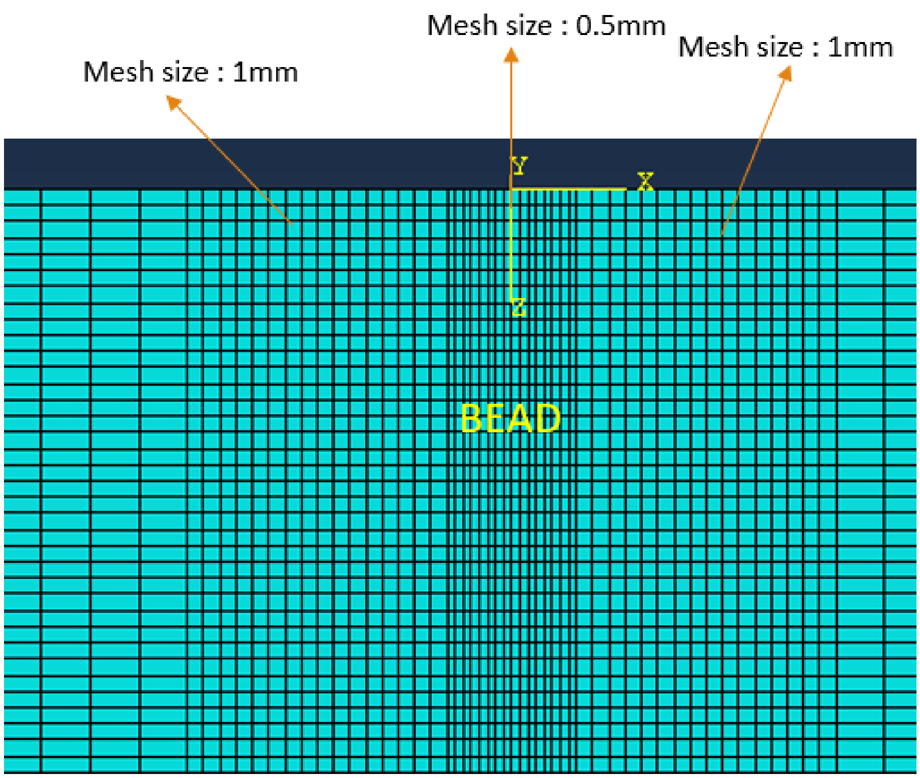

Figure 3-5b: Illustration of mesh design after zooming.

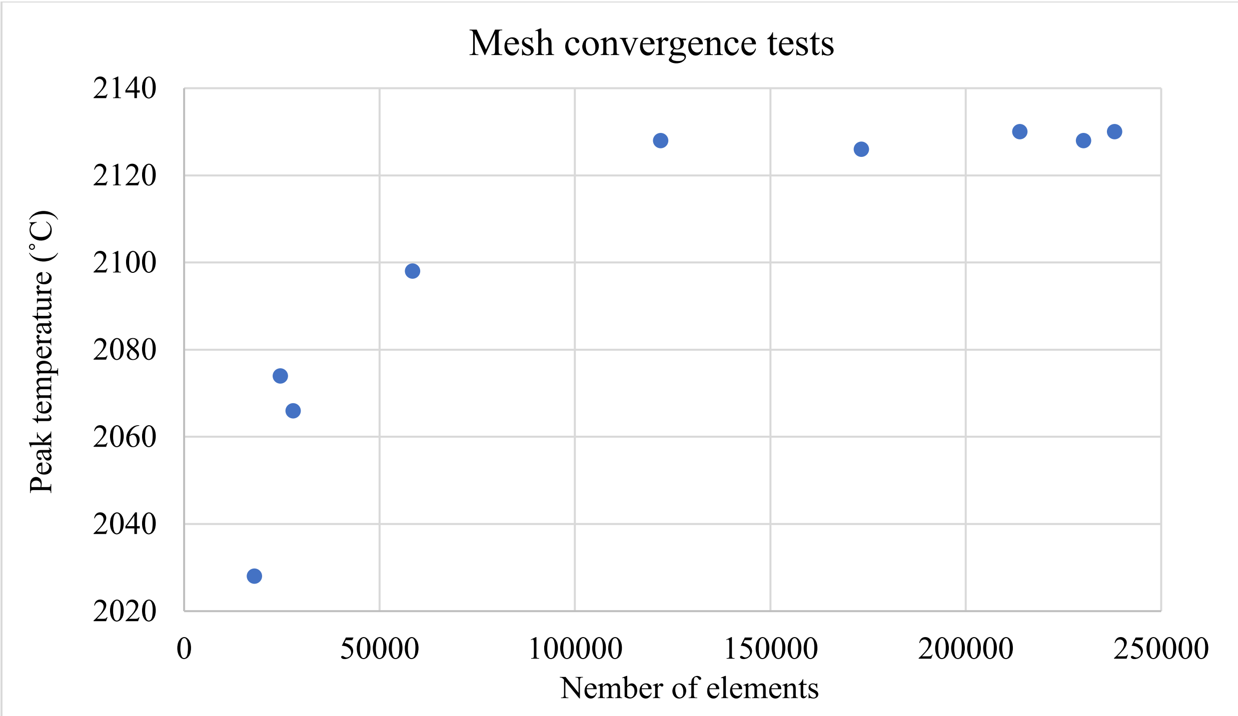

Figure 3-6: Mesh convergence tests.

Figure 3-6 shows the mesh tests that have been done. In this model, the mesh sizes are determined after several tries until the results are independent of the mesh sizing or until the results converge to nearly constant values. The result starts to converge from the number of the mesh at 100000.

When compared to other sections, the bead part has the finest mesh and measures 1mm in length and 0.5mm in width. The mesh increases to 1mm in width and 1mm in length in the area next to the bevel. They are irregular hexahedrons in these two areas. Mesh sizes on the parts further from the welding line are 3mm x 1mm x 3mm. They are rectangular cuboids.

The default element shape for the bead and the area far from the bevel is Hexahedral, commonly known as Hex elements. This structured meshing technique uses pre-established mesh patterns to predict the mesh pattern based on the topology of the region. This allows for a more efficient and accurate mesh generation process.[54]

In the vicinity of the bevel, a Hex-dominated element shape is utilized. While primarily using hexahedral elements, transition zones may also contain some triangular prisms. The technique applied here is swept meshing, which is utilized to effectively mesh complex solid and surface regions[55]. With the mesh designed, the model's total running time is an average of 5 hours with a DELL OptiPlex7080 x64-based PC, and the RAM is 16GB.

3.3.5 Additive Manufacturing Modeler

A pool of molten metal is created during welding by adding filler material. Heat causes the base metal also to melt. These two pieces are joined together. The AM Modeler can be an excellent tool for simulating the welding process as it is able to model the material and energy deposition that occurs during the process.

The AM Modeler in Abaqus has several critical parameters that must be considered. Given that the research only concerns the thermal analysis, a thermal analysis type is used. The AM Modeler has three main settings: Data Setup, Model Setup, and Simulation Setup. . In the Data Setup, all the necessary details about the material deposition and heat source are defined, including the positions of the heat source at different times, the Goldak parameters, heat input, and deposition rates. Once all the data is defined, it needs to be included in the AM analysis via Model Setup. Finally, in the Simulation Setup, the area of material deposition and the heat source is specified. Additionally, cooling due to convection or radiation heat transfer can be defined in this section.

3.4 Results

In Figure 3-7, two arrows indicate the direction "along the weld line" and "from the weld line". The white arrow is pointing in the opposite direction of the z-direction, which represents the direction along the weld line starting from the beginning of the weld pool. The red arrow is in the same direction as the x-direction but starts from the center of the weld pool. The arrows are used in the results section to help understand the temperature profiles in different orientations. Additionally, the temperatures presented in the simulation are all in degree Celsius (°C).

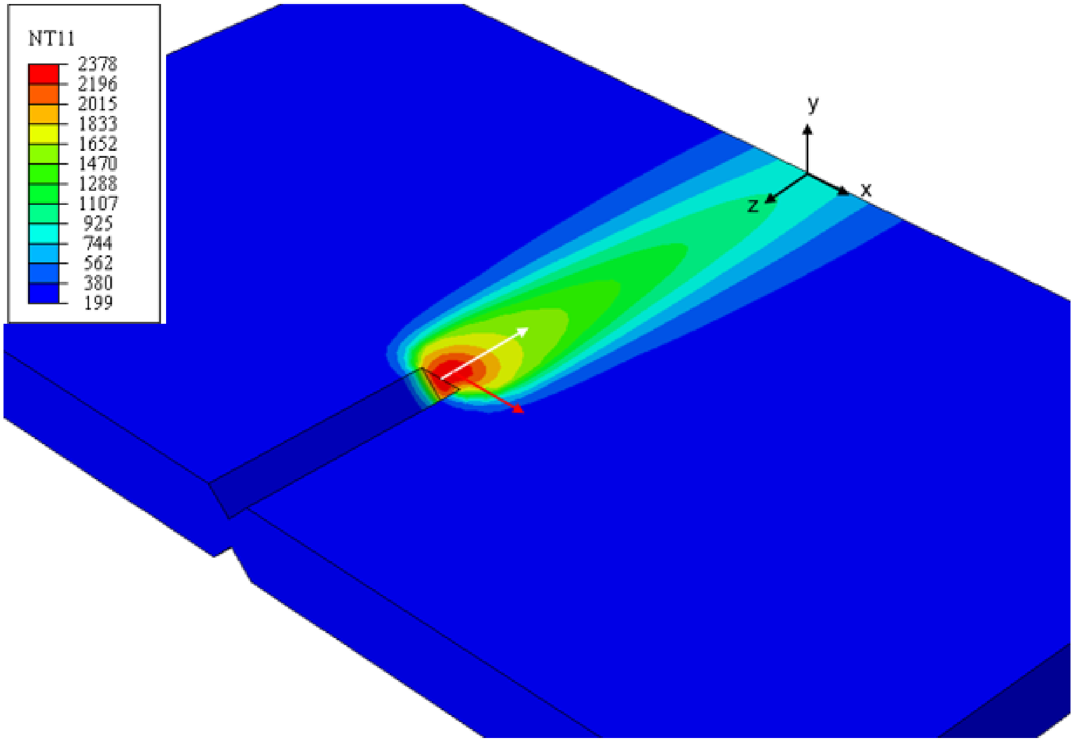

Figure 3-7: Illustration of the directions.

Figure 3-8 shows a sample of the temperature distribution along the weld line when the heat source travels 4s, around $\frac{2}{3}$ of the plate. The legend is in °C. The graphic demonstrates that the melting point is reached, so the welding occurs. The plot indicates that the melt pool is very long and that the cooling is slow even though the plot does not show the temperatures till the solidus temperature of 880°C.

Figure 3-9 illustrates the temperature profiles along the bead width for various depths at a representative z position. The liquidus temperature is shown as a black line in the figure. The temperatures are measured on the surface when y=0mm, the temperature profile 1mm below the surface is shown in the graph at y=-1mm, and so on. The plot at y=0mm intersects the melting point at around 6.5mm from the weld line, which implies that the bead width is around 13mm. The depth of the molten pool can be estimated to be around 6mm. This is inferred from the fact that the plot at y=-6mm is close to the melting point. This figure can aid in understanding the depth of the molten pool and the width of the bead.

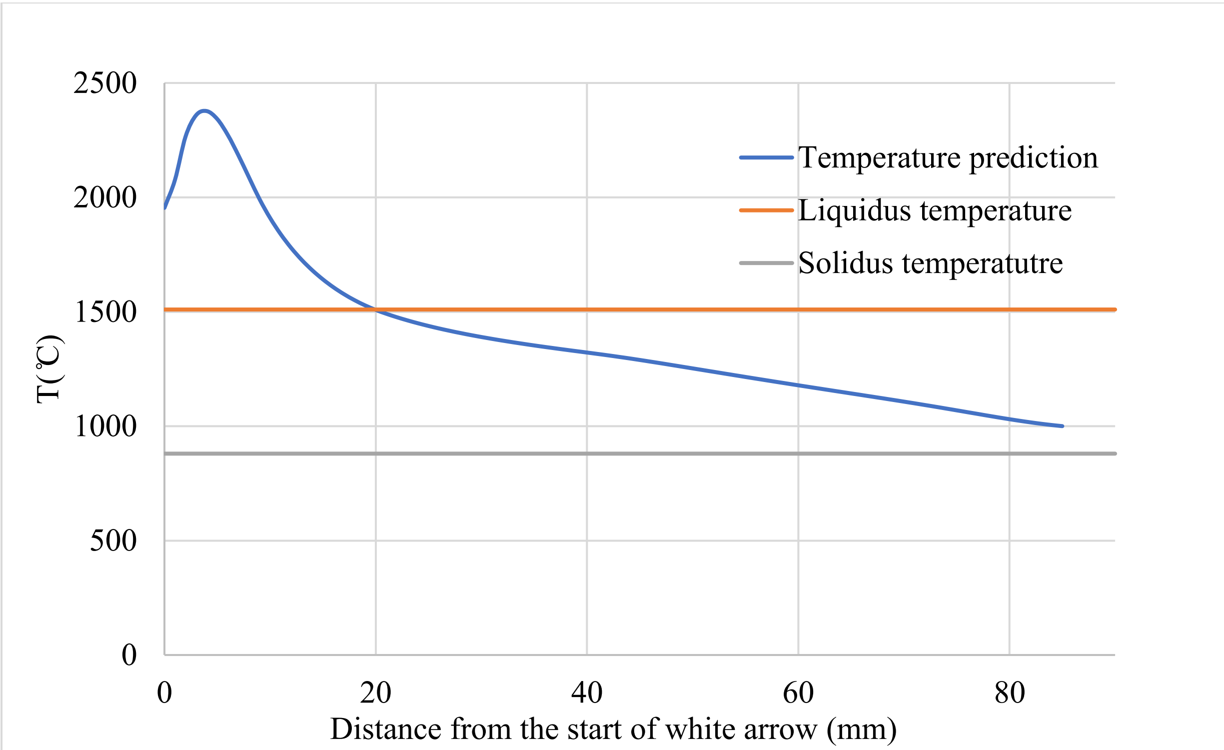

Figure 3-8: An example of the temperature profile along the weld line.

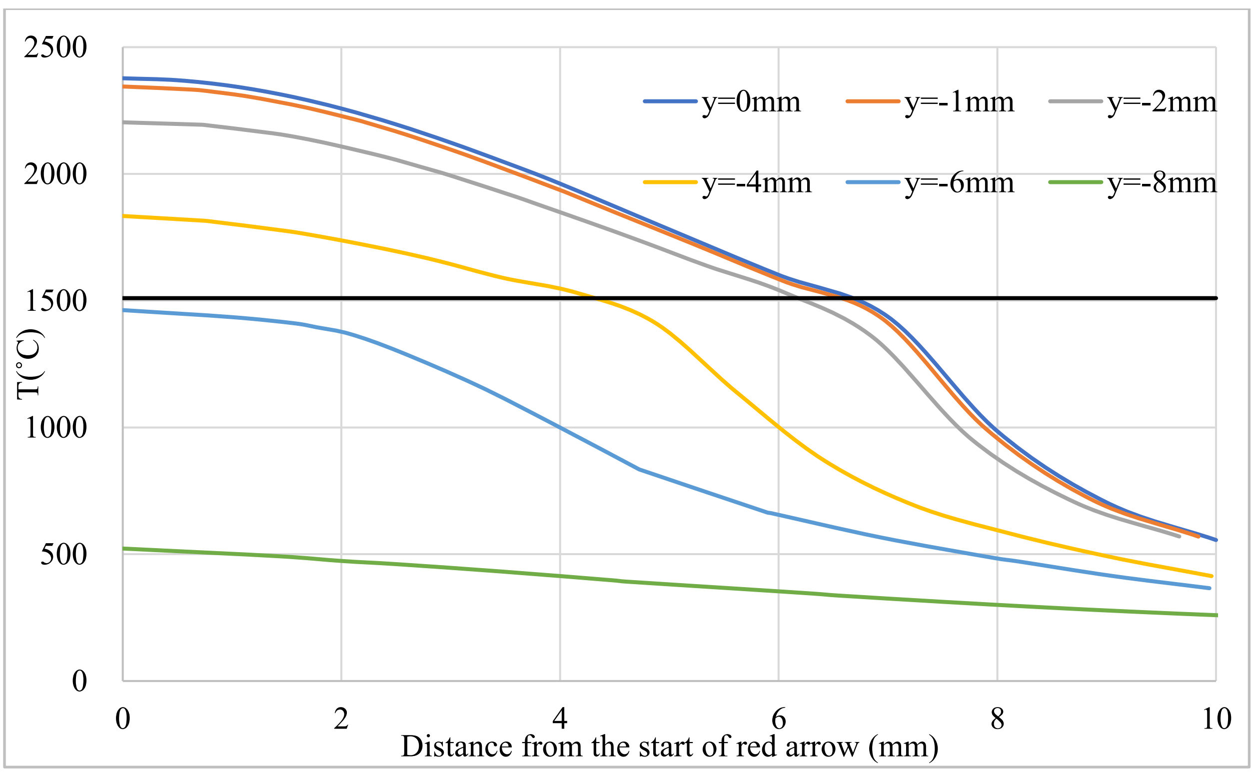

Figure 3-9: Temperature profiles along bead width for different depths.

Different heat inputs are then modelled by changing the power of the heat source. The heat input is influenced by welding current, arc voltage and the total travel speed. It is expressed as:

$$Heat\ input = \eta \frac{Welding\ current\ \times Arc\ voltage}{Total\ travel\ speed} \tag{3-18}$$

The Equation 3-18 can also be expressed as:

$$Heat\ input = \eta \frac{Power}{Total\ travel\ speed} \tag{3-19}$$

Figure 3-10 illustrates the temperature profiles along the weld line for different heat inputs. The heat input is directly proportional to the power, as described in Equation 3-19. The heat input is 41.6kW, and the travel speed is 21.2mm/s. Then, simulations with 20% more and 20% less power are conducted. The travel speed of the torch remains constant across all the simulations. From the three plots, it is clear that the one with the most power reaches the highest temperature. Even though some of the plots do not reach the material's solidus temperature, it is evident that the situation with more heat input has a slower solidification cooling rate. A slower solidification cooling rate can result in a reduction of hardness and an increase in ductility, and can prevent distortion. This graph provides valuable insights into the impact of heat input on the temperature profile and can aid in understanding the effect of heat input on the final microstructure of the welded material. [56]

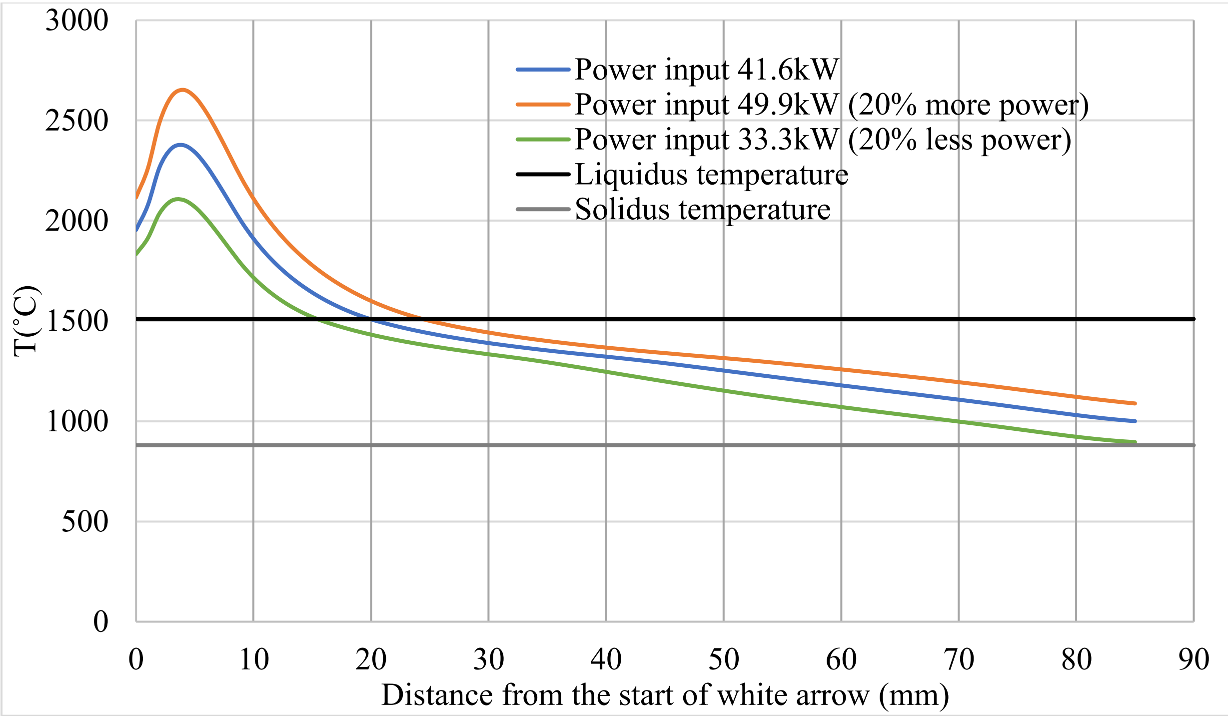

Figure 3-10: Temperature profiles for different heat inputs along the weld line.

In Figure 3-11, temperature profiles for different heat inputs along the x-axis are shown. The case with more power has a larger weld pool. According to the calculations, in this case, a 20% increase in power results in a 15% increase in bead width.

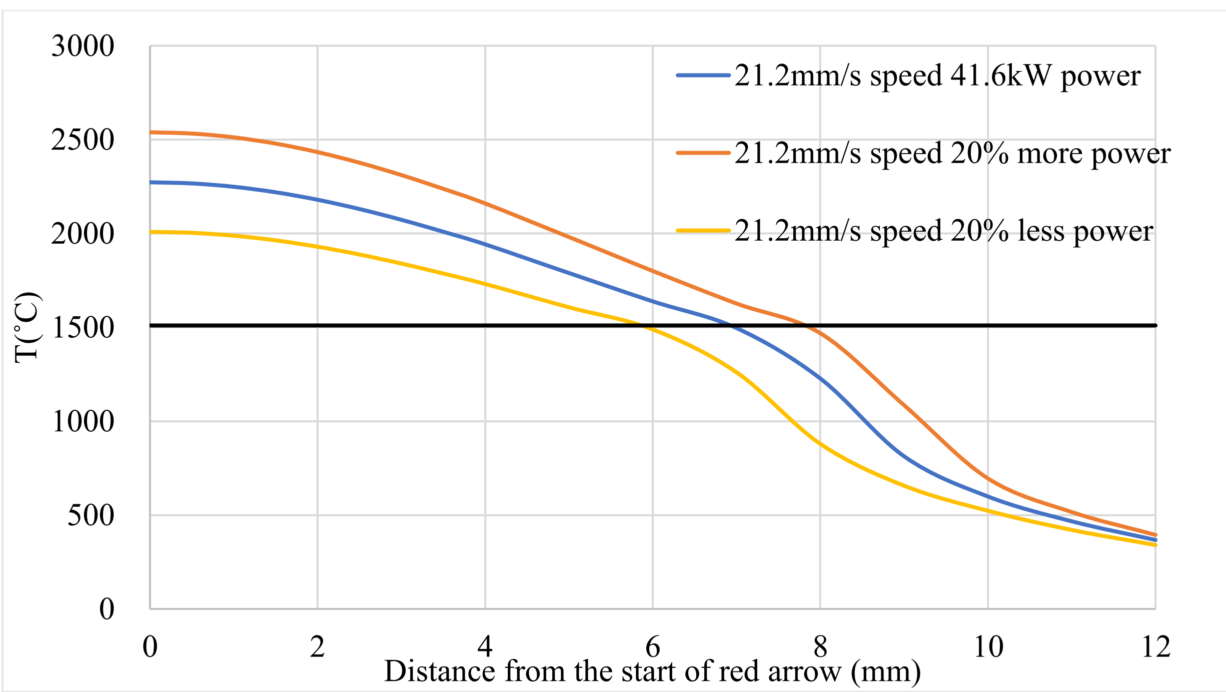

Figure 3-11: Temperature profiles for different heat inputs along the x-axis.

According to Equation 3-19, the travel speed affects the heat input as well. As a result, models of welding processes with various travel speeds are created. Figures 3-12 and 3-13 present temperature profiles for various travel speeds. Along the weld line, the temperature rises until it reaches its peak, then it starts to fall. The peak temperature is higher when the travel speed is slower. After the temperatures drop to the liquidus temperature, the results start to overlap. Plots along the x-axis demonstrate that a lower travel speed results in a larger melt pool. This is due to the fact that the bead's heat input increases as travel speed reduces.

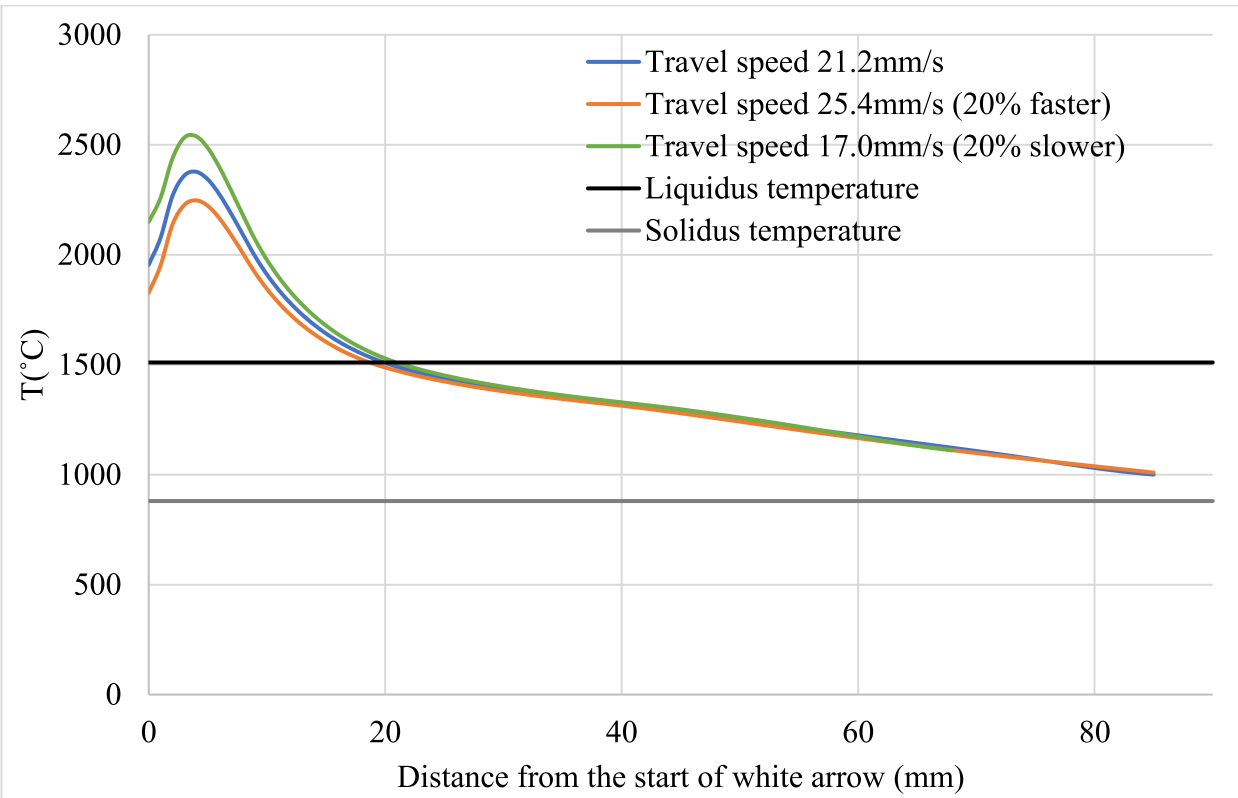

Figure 3-12: Temperature profiles for different travel speeds along the weld line.

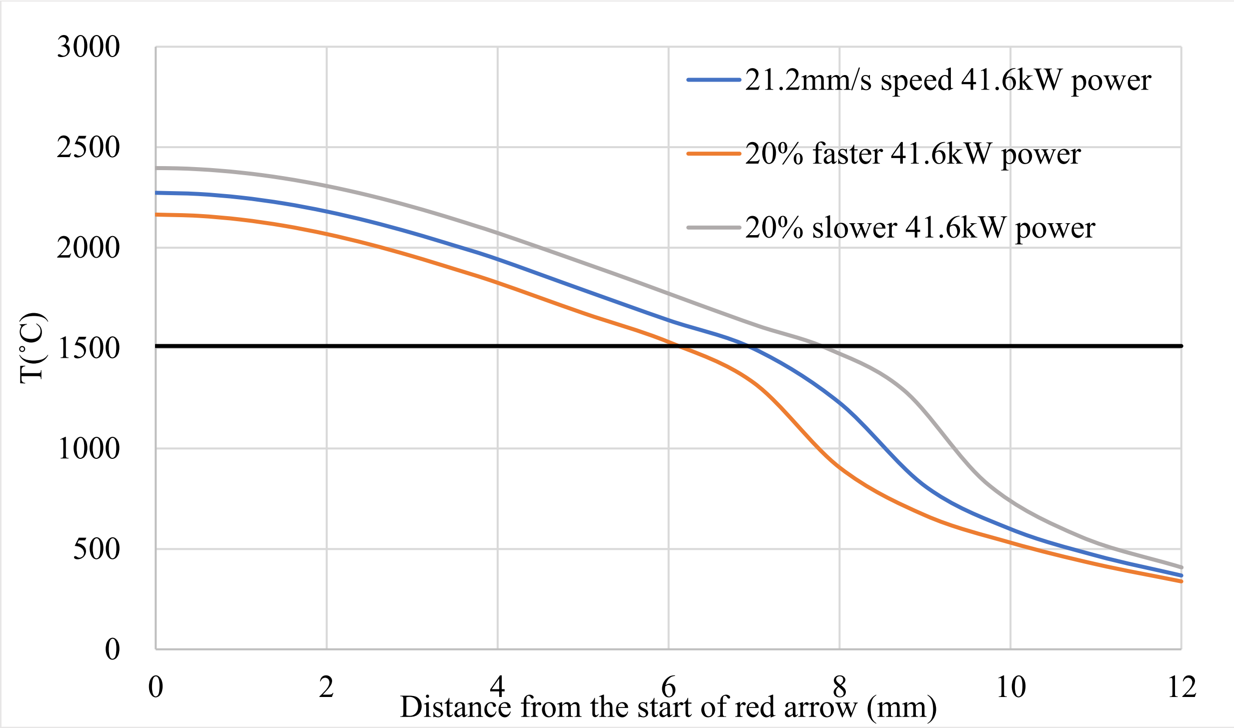

Figure 3-13: Temperature profiles for different travel speeds along the x-axis.

3.5 Validation with experimental tests

According to the previous results, the simulation in Abaqus can simulate the temperature profiles even for different variables. However, it is necessary to validate the model and prove that the simulation is correct. In previous research done by Lecoanet [1], the same process (SAW) was used in the research. The temperature is measured during the experiments, which can be a good reference. Therefore, a model with the same input values as the research reported by Lecoanet [1], including the geometry of the plate, the heat input and the boundary conditions, is created. The new plate is 30cm long, 7.5cm wide and 1.34cm high. The travel speed is 8.9mm/s. The new convective coefficient is 15 W/(m^2K).

The simulation results were compared to the experimental results obtained by experimental testing[1]. For the comparison, a new model in Abaqus is created using the same conditions in Lecoanet's research. The simulation methods are the same as described previously; only the geometry of the plates and the heat input are different. The details of the experimental measurements are discussed in Chapter 2.3. Two locations—R2KbZ2, which is far from the weld line and at the edge of the heat-affected zone, and R2KaZ1, located in the heat-affected zone and close to the weld line—are selected for comparison.

The results from Lecoanet [1] and the prediction of Abaqus are combined to create Figure 3-14. Only three plots—Tmeasured, Tellipsoid, and TAbaqus—are compared in this graph. The experimental results and simulation results obtained using COMSOL acquired in the previous research [1] are plotted as T measured and T ellipsoid, whereas T Abaqus is the temperature prediction obtained by Abaqus. The three plots display similar trends. The TAbaqus plot starts at 200°C due to the preheat applied to the plate. The temperatures predicted by COMSOL and ABAQUS are higher than the experimental ones; however, towards the end of the plots, the temperatures are relatively similar. The cooling rates in all the plots are also comparable. This comparison suggests that the simulation results are in good agreement with the experimental data, and the cooling rate predicted by the simulation is consistent with the experimental results.

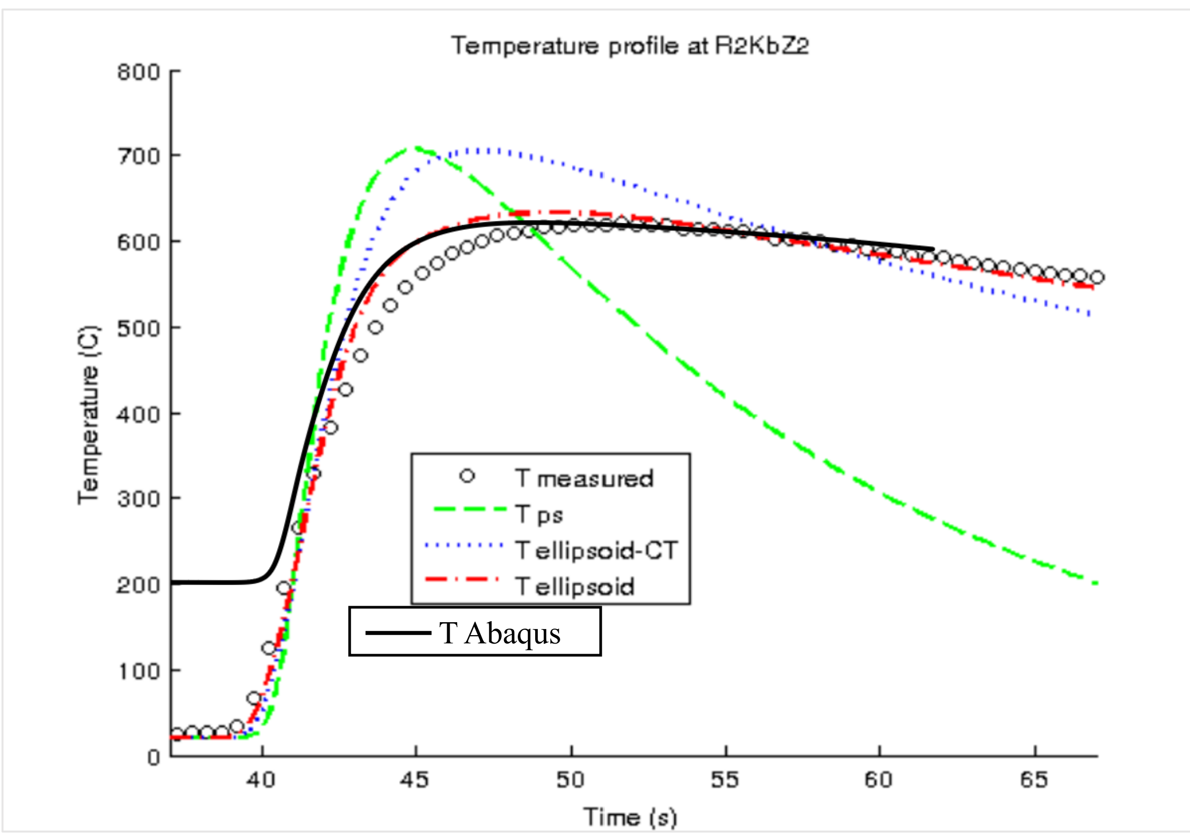

Figure 3-14: Comparison of temperature profiles as a function of time at position R2KbZ2. (A combination of plots) [1]

Figure 3-15 shows the temperature profile at R2KaZ1. Similar to Figure 3-14, only the three plots Tmeasured, Tellipsoid, and TAbaqus are taken into account. The temperature rises until it reaches a peak, then it starts to decrease. The highest temperatures predicted by both models are higher than the measured value. However, the temperatures are very similar, starting from the 50s. The differences were discussed in previous research [1]: The thermocouple might not have been positioned exactly at the bottom of the hole. The bead widths are also compared with the previous research. The experimental data showed an average bead width of 15.3mm, while the predicted value is 14mm. These comparisons suggest that the simulation results agree with the experimental data, with small discrepancies that can be attributed to measurement errors.

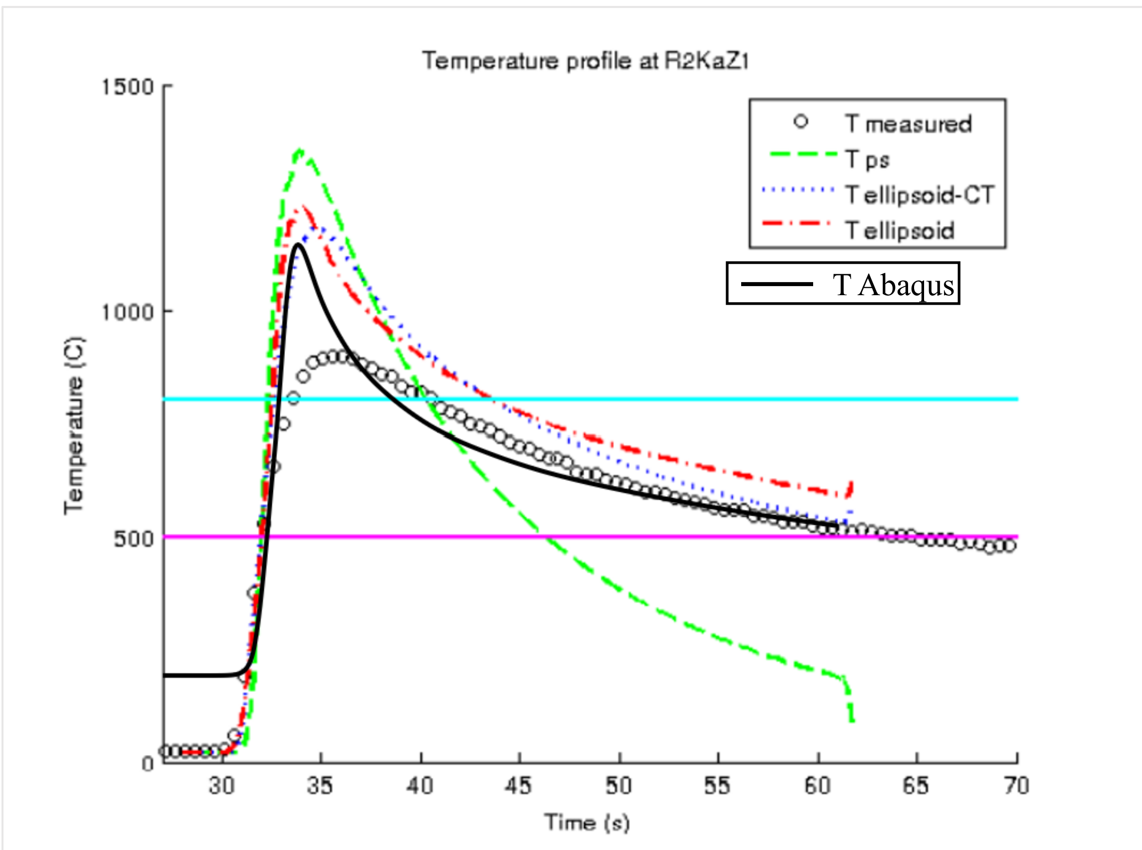

Figure 3-15: Comparison of temperature profiles as a function of time at position R2KaZ1. (A combination of plots) [1]

3.6 Summary

This chapter demonstrates how the AM modeller in Abaqus, a new finite element modelling package, can successfully estimate the temperature profile of the SAW process. The simulation results are compared with experimental data and COMSOL results from earlier studies. We can predict the microstructure and characteristics of the weld in future studies since the model can not only predict the temperature profile on the weld line but also in the heat-affected zone. The Am modeler in Abaqus can now be used to simulate other welding conditions and processes with confidence.

Chapter 4: Modelling of the thermal history of Wire and arc additive manufacturing (WAAM) using Abaqus.

4.1 Introduction

Wire and arc additive manufacturing (WAAM) is a direct energy deposition method that uses a welding process to deposit molten material onto a substrate in the form of beads. A layer is created as the beads coalesce. The process is then repeated layer by layer until the metal part is completed. This method is efficient because it has a high deposition rate and lower cost compared to other additive manufacturing (AM) processes.

In this study, a new finite element model is developed to simulate the wire and arc additive manufacturing (WAAM) process. The simulation utilizes Abaqus's plug-in Additive Manufacturing modeler to accurately predict key performance indicators such as temperature profile, solidification cooling rate, and solidification time. To begin with, the method is first applied to model a single-pass WAAM. The predictions are then compared with experimental values to validate the accuracy of the proposed method. Furthermore, the model developed can be used to predict potential issues that may arise during the WAAM process and help prevent defects, thus improving the overall performance and efficiency of the WAAM process. Additionally, the method can be extended to model multiple-pass WAAM.

The governing equations used to model the wire and arc additive manufacturing (WAAM) process are the general heat conduction equations in Cartesian coordinates. These equations are identical to those used in the case of SAW. The equations consider the effects of convection and radiation through the implementation of boundary conditions. Furthermore, the welding process considered in this study is gas metal arc welding (GMAW), which is commonly used in WAAM.

4.2 Simulation Description

4.2.1 Geometry

The size of the simulated substrate plate is 152 mm, 51 mm, and 6 mm (Figure 4-1). The plate's geometry matches that of the experimental test exactly. As for the bead, it is directly deposited on the plate. The bead width is 6.6 mm, and the bead height is 3.8 mm.

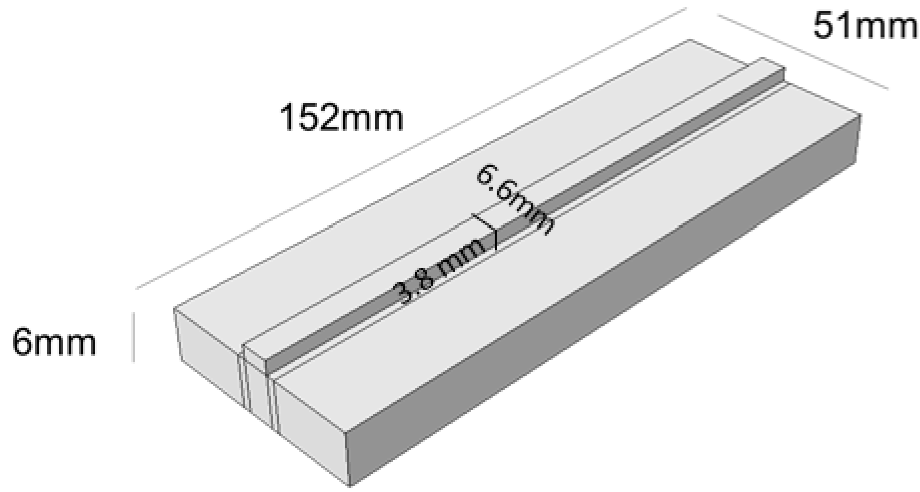

Figure 4-1: Geometry of the plate and the bead.

4.2.2 Thermo-physical properties

The material chosen in this WAAM process is 17-4 stainless steel (also known as 17-4 PH). The "17-4" in the name refers to the composition of the steel, which includes 17% chromium and 4% nickel. The "PH" stands for "precipitation hardening", which is a heat treatment process used to increase the strength and hardness of the alloy.

The heat-treating process involves solutionizing the steel to ensure that all copper is dissolved. This is followed by re-heating the material to a specific temperature, holding it for a specified time, then cooling it. This causes small, hard precipitates of copper to form within the alloy, which results in an increase in strength and hardness. This type of stainless steel is commonly used in aerospace and defence applications, as well as in the oil and gas industry and other high-stress applications.

Table 4-1 shows the composition of the 17-4 PH studied in this simulation. The conductivity is obtained from the datasheet of Rolled Alloy, and they are shown in Appendix A.2. [16] Knowing the composition, the key properties such as liquidus temperature, solidus temperature, density, heat capacity and latent heat can be determined with the help of the software THERMO-CALC. As an example, Figure 4-2 indicates the liquidus temperature of the material is 1458° C, and the solidus temperature is 1191˚ C.

Table *4-1: Composition of 17-4 PH*

Element	Wt. %
C	0.012
Mn	0.44
Si	0.41
P	0.022
S	0.001
Cu	3.33
Ni	4.57
Cr	16.11
Mo	0.04
N	0.03
Nb+Ta	0.23
Fe	Balance

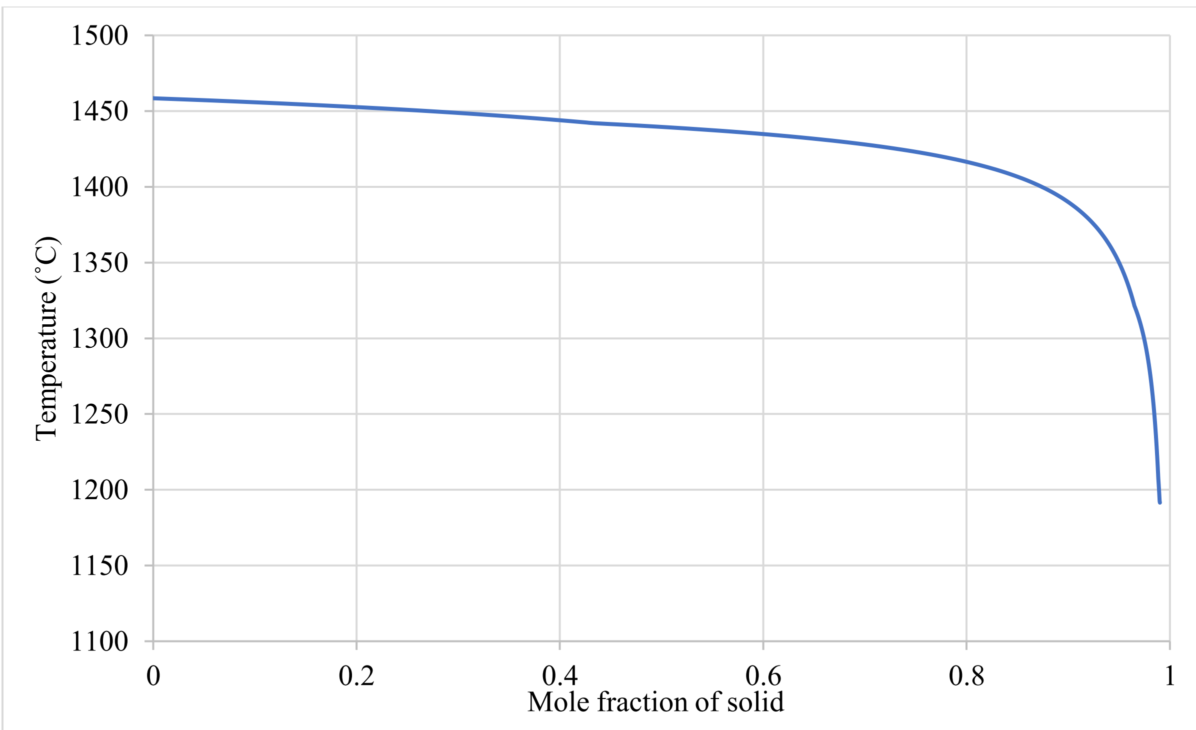

Figure 4-2: Temperature as a function of mole fraction of solid.

Figure 4-3 is the latent heat per gram as a function of temperature in the range of solidus and liquidus temperature. The latent heat of fusion is the integral of latent heat per gram within the temperature range. A simple way of calculating it is to find the area under the curve. As a result of approximation, the latent heat of fusion is around 40.7 kJ/g.

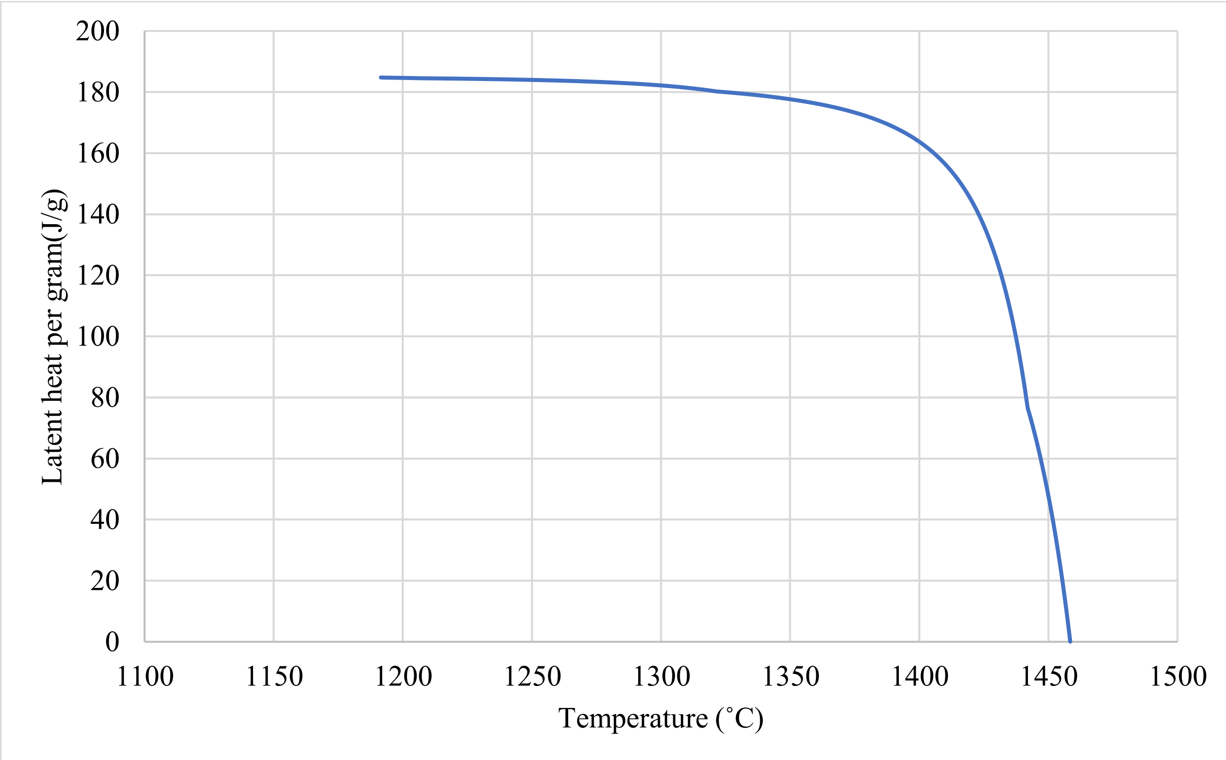

Figure 4-3: Latent heat per gram as a function of temperature.

4.2.3 Initial and boundary conditions

The ambient temperature is 20˚C, and the initial temperature of the bead is set to 1500˚C, close to the material's liquidus temperature. The bead gets heated, and the temperature will increase when the heat source passes. The base metal has an initial temperature of 200˚C to simulate the preheating of the plate.

To simplify the analysis, Figure 4-4 illustrates the X plane of symmetry, which implies that U1 = UR2 = UR3 = 0. In the equation, 1,2,3 represents the x,y, and z axes. U1=0 indicates that the plane is fixed in the x-direction; UR2=0 and UR3=0 mean that the plane cannot rotate in the y and z directions. This results in significant improvements in simulation time and memory requirements. As a result, a more refined mesh can be employed for a more precise analysis.

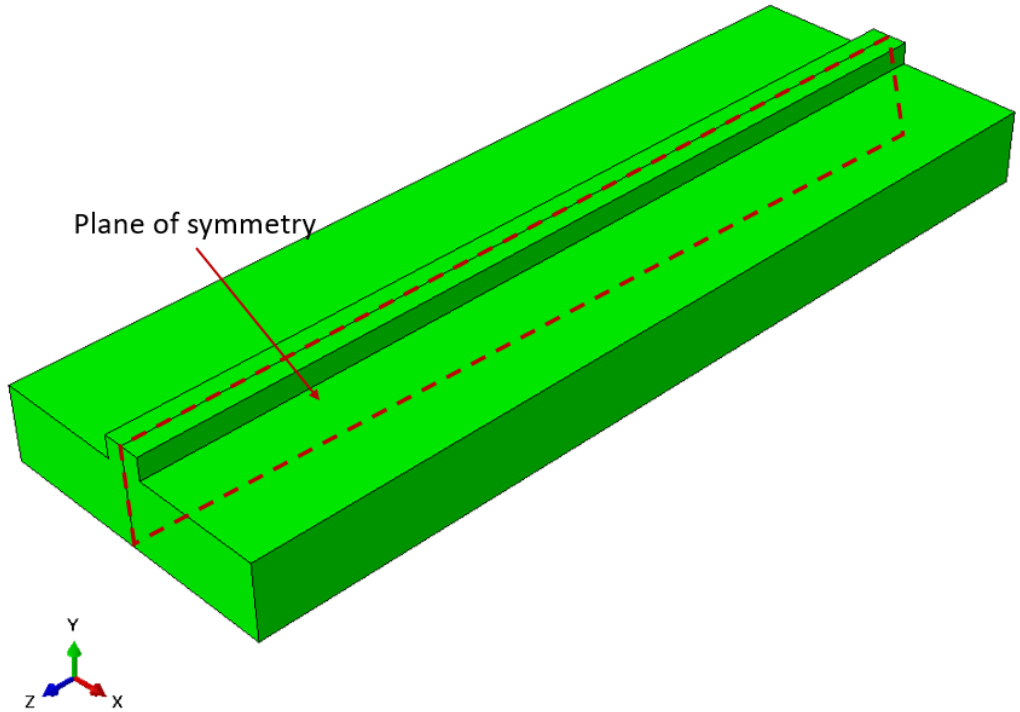

Figure 4-4: Illustration of symmetry.

As depicted in Figure 4-5, the z-direction represents the welding direction. The bead surface is subject to convection and radiation. On the other hand, the base metal and heat-affected zone (HAZ) generally exhibit a low heat transfer rate, which is primarily due to conduction rather than convection. However, as mentioned before, the plate is preheated to 200˚C, so there will be convection occurring at these surfaces, although it is very small. As for the bottom surface, the process has no influence on it, and it is contacted with a table. Therefore the temperature at the bottom surface is the same as the ambient temperature. No heat transfer is considered between the bottom plate and the environment. The boundary condition for convection is derived by combining Newton's Law and the Fourier heat conduction equation. Equation 3-17 is the boundary condition in this case.

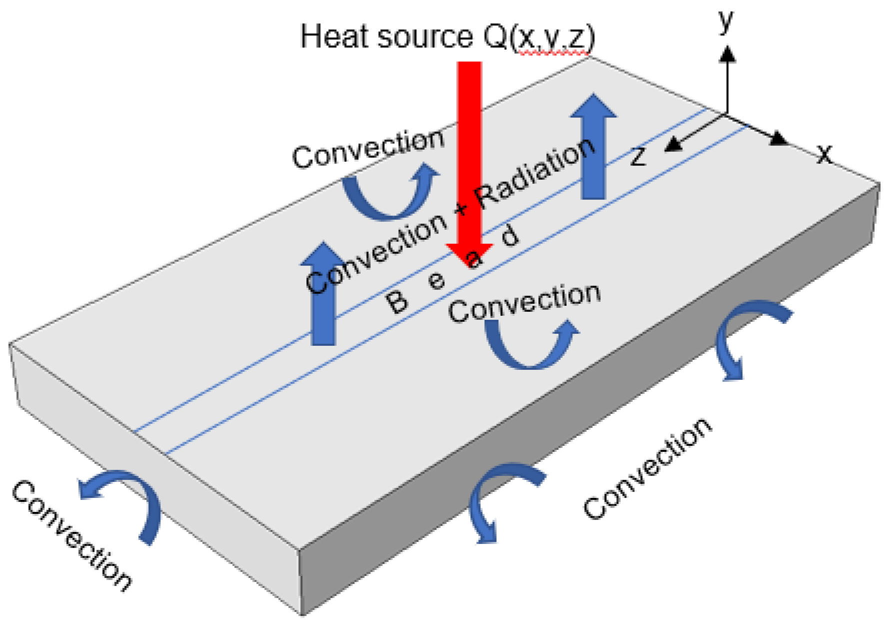

Figure 4-5: Convection and radiation on the plate.

Several correlations can be used to estimate the convective heat transfer coefficient (h) at the deposited surface for GMAW, including the Gnielinski correlation[57], the Dittus-Boelter equation[58], and the Sieder-Tate correlation[59]. Before using the correlations, the Reynolds number (Re) and the Prandtl number (Pr) are calculated first.

The Reynolds number (Re) is a dimensionless quantity that describes the ratio of inertial forces to viscous forces in a fluid flow.

$$Re = \frac{vL}{\mu} \tag{4-1}$$

In equation 4-1, v is the flow velocity (m/s); L is the characteristic length (m), here is the bead width; μ is the kinematic viscosity (m^2/s).

The gas used in this process is Argon, with a gas flow of 35 cubic feet per hour (CFH), which is $2.75 \cdot 10^{-4}$ cubic meters per second. Equation 4-2 indicates the method of calculating the flow velocity.

$$Flow\ velocity\ = \frac{Flow\ rate}{Cross - section} \tag{4-2}$$

Where the unit of flow velocity is m/s, and that of flow rate is m^3/s. The cross-sectional is the cross-section of the nozzle, which has a diameter of 13mm.

Re has a value of $2.8x10^4$ as a result of the calculation. This indicates that the flow of the gas is in a turbulent flow regime during the welding process.

The Prandtl number (Pr) is a dimensionless quantity that describes the ratio of the fluid's momentum diffusivity to its thermal diffusivity.

$$Pr = \frac{\mu}{\alpha} \tag{4-3}$$

α is the thermal diffusivity (m^2/s). Plugging the values into Equation 4-3, the Pr is around 0.72.

The Gnielinski correlation [57] is given by the following equation:

$$h = \frac{0.023Re^{0.8}Pr^{0.4}}{1 + 12.7\left(Pr^{\frac{2}{3}} - 1\right)^{\frac{1}{4}}} \tag{4-4}$$

The acceptable range for the calculations of Reynolds number (Re) and Prandtl number (Pr) is typically between 10^3 to 10^6 and 0.7 to 500, respectively. Once the values of Re and Pr are calculated, the chosen correlation can be used to estimate the convective heat transfer coefficient (h). An h of 786.6 W/(m^2K) would be obtained as a result. It is important to note that the Gnielinski correlation may work well for certain fluids and geometries, but it is not universally applicable and experimental data is recommended to validate the results.

The Dittus-Boelter equation [58] (4-5) is a correlation that can be used to h for a fluid flowing over a solid surface.

$$h = 0.037Re^{0.8}Pr^{\frac{1}{3}} \tag{4-5}$$

Equation 4-5 is used when $10^4 \leq Re \leq 10^6$, and $0.5 \leq Pr \leq 200$. By calculation, h is 772.5 W/(m^2K).

As for the Sieder-Tate correlation[59],

$$h = \frac{k}{d} Re^{0.8} Pr^{0.33} \tag{4-6}$$

In the correlation, k is the thermal conductivity of the fluid (W/(mK)), and d is the diameter of the nozzle (m). The correlation is used for a Re from 10^3 to 10^6, and a Pr from 0.7 to 200. An h of 815.9 W/(m^2K) is obtained.

The values of h calculated by these three methods are similar. An average value of 791.7 W/(m^2K) is input in the Abaqus simulation. For the other parts on the plate, the convective coefficient is considered as 3W/(m^2K).

At the top surface, the radiation is also considered. The radiation heat exchanged given by Stefan-Boltzmann law is:

$$q_r = \sigma\varepsilon(T^4 - T_\infty^4)dSdt \tag{4-7}$$

Where σ is the Stefan-Boltzmann constant, which is 5.67 x 10^{-8} (W/m^2K^4). The emissivity, represented by ε, of 17-4PH stainless steel is generally 0.85-0.9, indicating good thermal radiation emission. Refs

Then, the boundary condition for the radiation is given by:

$$-k\frac{\partial T}{\partial n} = \sigma\varepsilon(T^4 - T_\infty^4) \tag{4-8}$$

This equation describes the heat transfer by radiation to the surrounding air. Here, λ is the thermal conductivity of the surface. $\frac{\partial T}{\partial n}$ is the temperature gradient in the normal direction to the bead surface.

4.2.4 Mesh design

To ensure that the solution of the model is not sensitive to the size of the elements in the mesh, mesh convergence is tested. The same model is run multiple times with different mesh densities till the results no longer change significantly. As shown in Figure 4-6, to start, a coarse mesh is used, then the mesh is refined incrementally. This process ensures that the solution is not sensitive to the size of the elements in the mesh, resulting in accurate results with less computational power demanded. The results start to converge when the number of mesh arrives at around 40000.

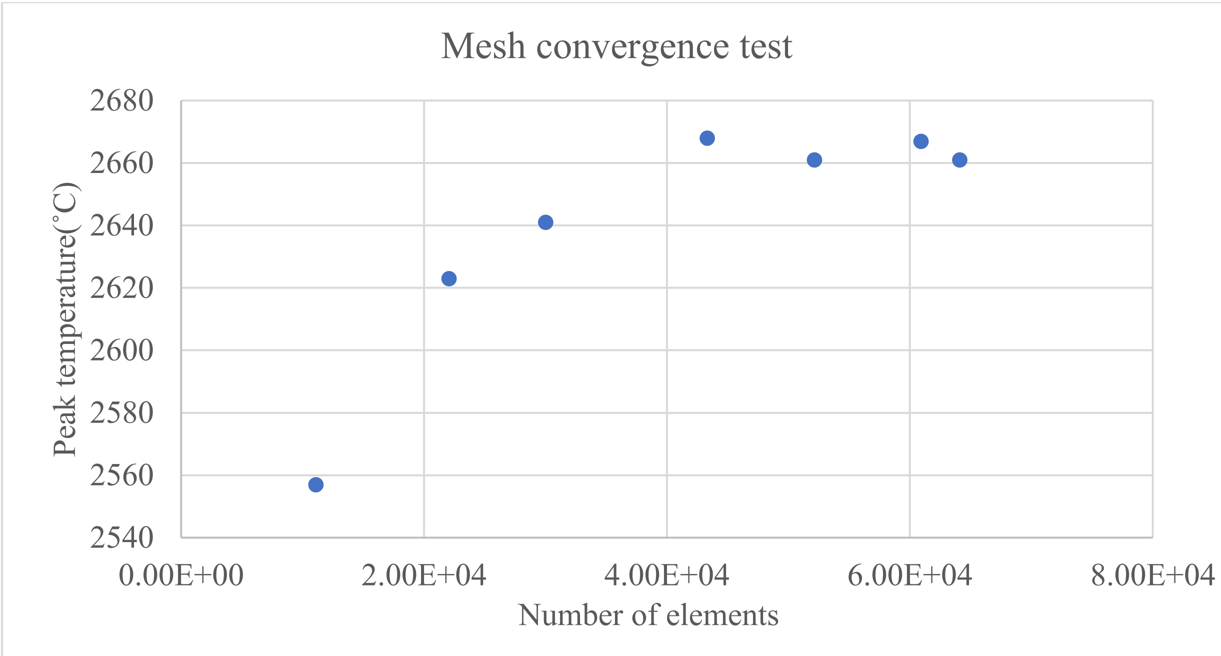

Figure 4-6: Mesh convergence test.

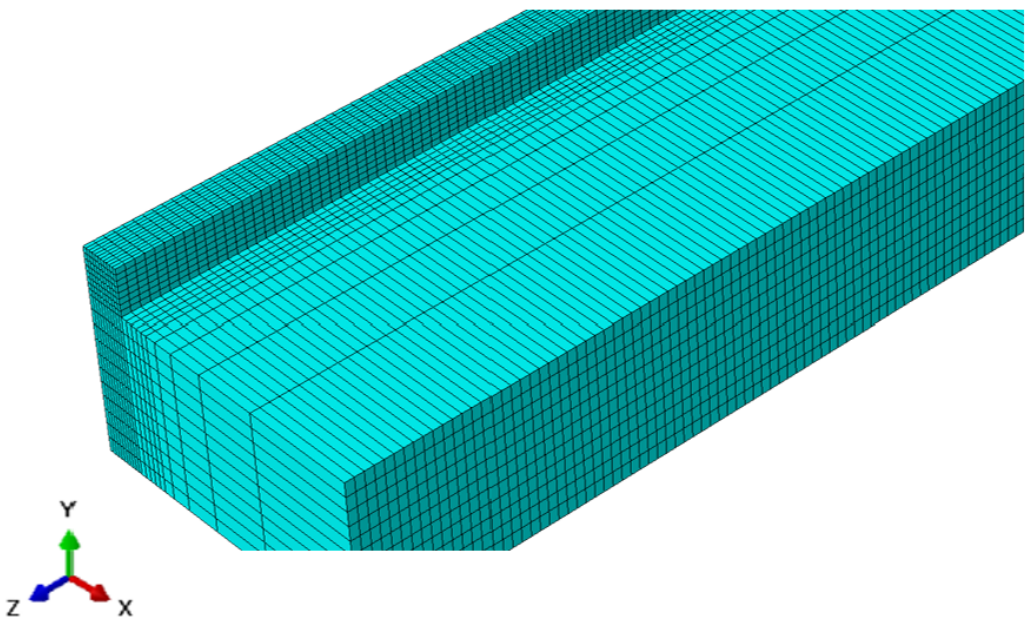

Figure 4-7: Mesh size design.

The final mesh design used in the model is shown in Figure 4-7. The elements on the bead have a size of 0.3mm x 0.5mm x 1.2mm. The width of the elements gradually increases from 0.5mm to

10mm as they move away from the weld line. Using a blend of uniform and refined elements allows the model to accurately depict the material's behaviour while minimizing the time needed for generating simulation results. Partitions are created at the edge of the bead and near the bead. The goal is to divide the plate and make the mesh easier. Generally, a DELL OptiPlex7080 x64-based PC, which has a RAM of 16GB, has an average running time of 2.3 hours.

4.3 Results:

In this section, the results of the WAAM process simulated in Abaqus are presented and discussed. The results will be discussed in terms of the maximum temperature, solidification cooling rates as a function of heat inputs, and bead depth. The results provide valuable insight into the thermal behaviour of the WAAM process, which can be used to optimize the process and improve the quality of the weld produced.

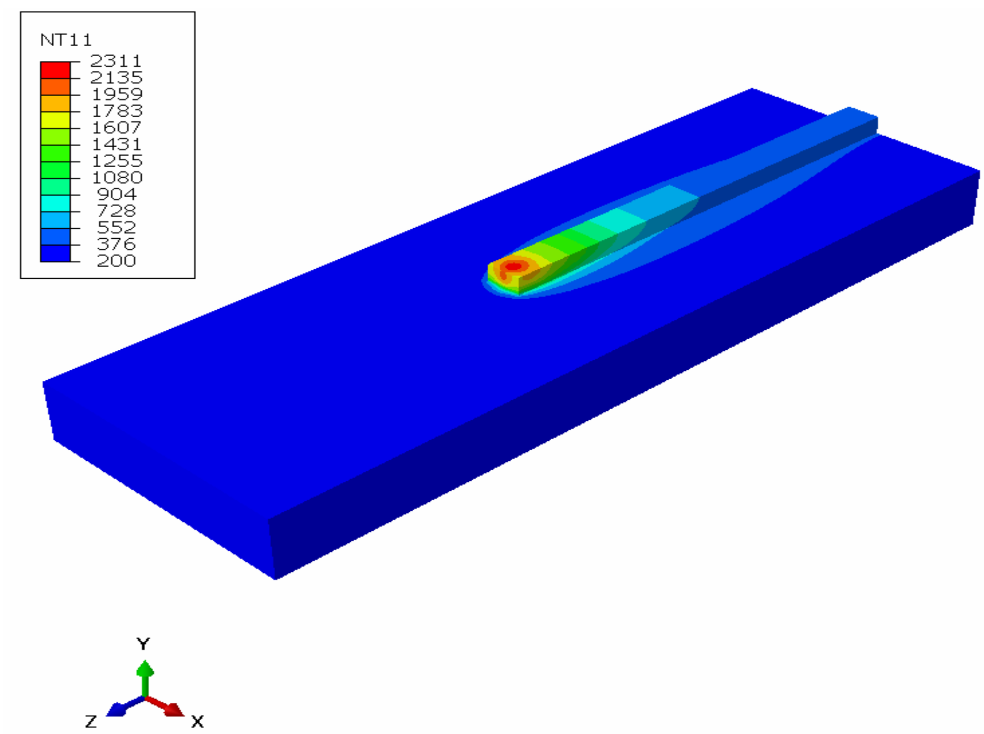

Figure 4-8: Example of the model results.

Figure 4-8 is an example of a simulation result with a low heat input of 617 J/mm. The temperatures in the simulation are all in °C. It can be observed that the highest temperatures occur in the molten pool as the material is being deposited and the heat source is passing. However, it can be noted that in the areas far from the welding line on the plate, the process has little influence on their temperatures.

As shown in Figure 4-9, point A is a point on the welding line, and point B is a position in the HAZ, 0.5mm from the bead so that 3.8mm from the welding line. The temperature profiles of points A and B are shown in Figures 4-11 and 4-12.

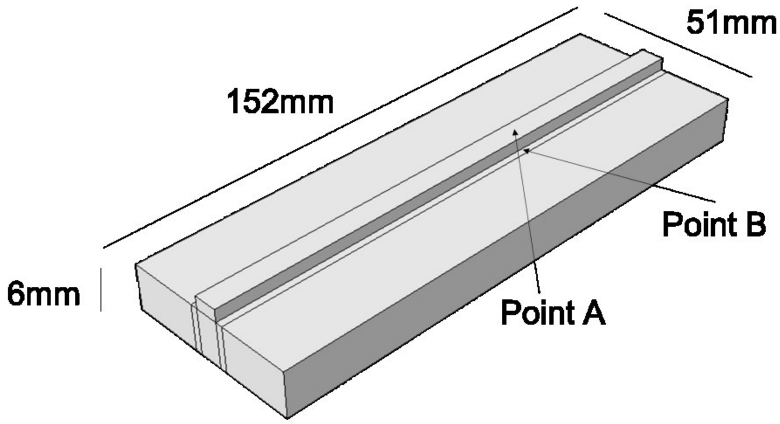

Figure 4-9: Indication of position for points A and B.

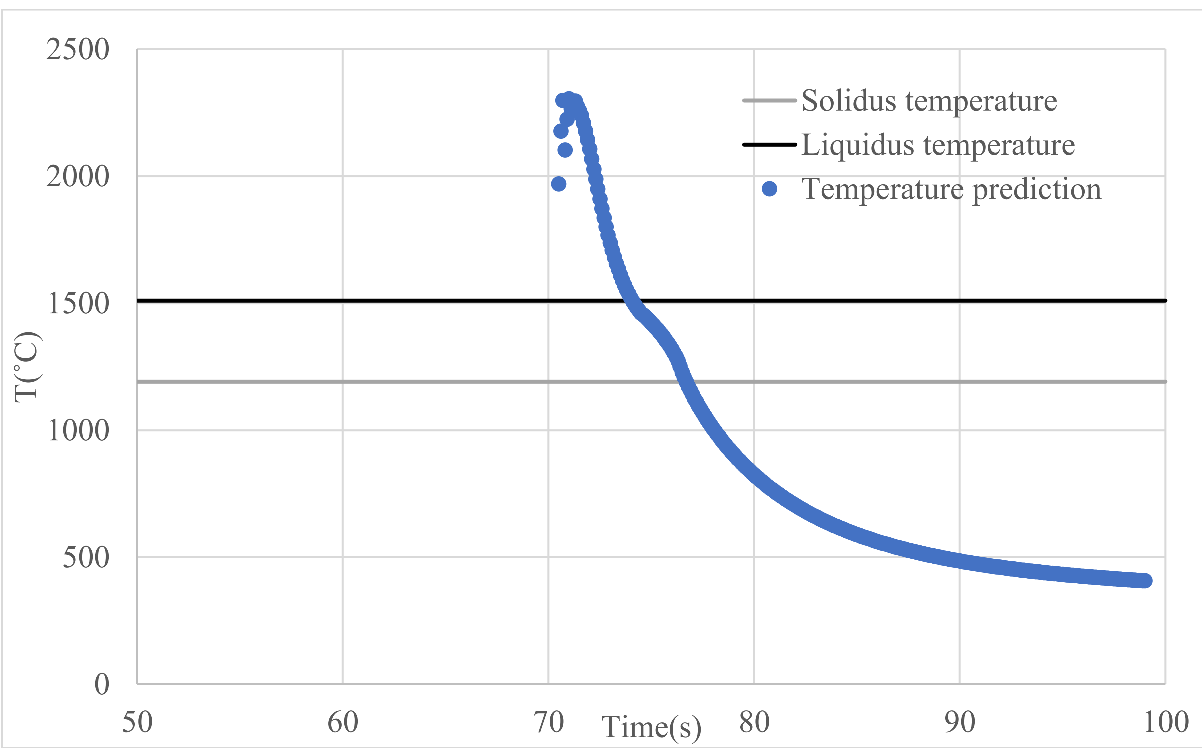

Figure 4-10: Temperature profile at point A.

Figure 4-10 is the temperature profile at point A. When the material is being deposited by the WAAM process, the temperature of the material at the point on the weld line is not considered here, as it is not yet in contact with the heat source. As the material is deposited and comes into contact with the arc, the temperature rapidly increases until it reaches a peak. With the deposition of the material, the temperature begins to decrease as it begins to solidify. Once the material reaches the solidus temperature, it solidifies completely. It's also important to note that the change of the slope at the temperature around 1500°C to 1200°C, refers to the phase change during the liquidus and solidus temperatures.

In Figure 4-11, a temperature profile at point B is shown. When the material is being deposited by the WAAM process, the temperature of the material at a point in the HAZ is relatively low. As the deposited material solidifies and the heat from the arc is transferred to the surrounding material, the temperature at the point in the HAZ increases gradually. The rate of this temperature increase depends on the thermal conductivity of the material and the distance from the welding line. The temperature continues to increase until it reaches a peak, at which point the cooling process begins. The cooling rate from 800°C to 500°C is of particular interest when discussing the microstructural evolution of the material. In this period, the decrease in temperature can lead to the formation of martensite and other microstructures, which can affect the mechanical properties of the material. However, in the point of view of multiple-pass WAAM, the cooling rate for liquidus to solidus temperature is also important as it can affect the solidification of the droplets so that the quality of the welds and the final microstructure of the material. In this study, the solidification cooling rate, which means the cooling rate from liquidus to solidus temperature, is the main focus.

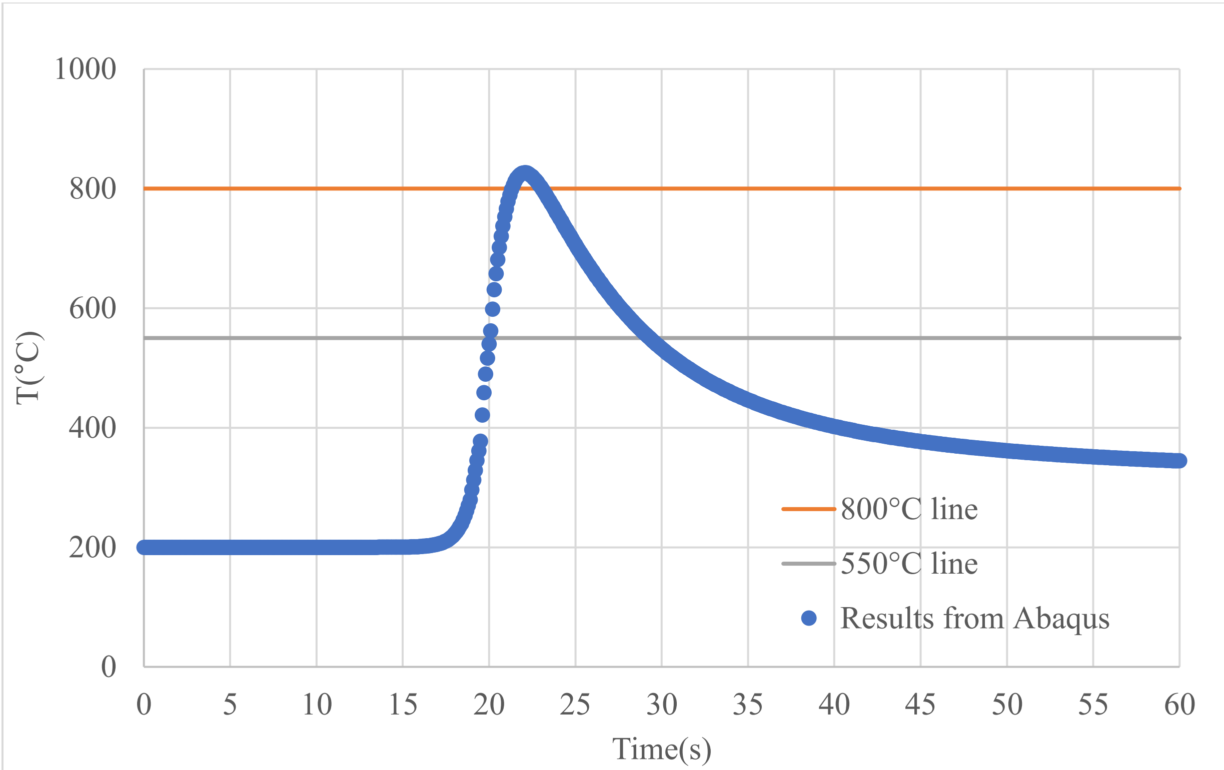

Figure 4-11: Temperature profile at point B.

The prediction of the solidification cooling rate is one of the key objectives of this study, as the cooling rate has a significant impact on the microstructure and mechanical properties of the deposited material. It also has an essential influence on the deposition of the next layers. Figure 4-12 shows that the FEM simulations reveal that the cooling rate from liquidus to solidus decreases as the heat input increases. This phenomenon can be attributed to the increased amount of heat that is being transferred into the deposited material, resulting in a slower solidification cooling rate.

Figure 4-13 helps to measure the bead depth of the predicted model. The bead depth can be determined by analyzing the cross-section of the simulated deposit and measuring the distance between the plate's surface and the penetration at the solidus temperature.

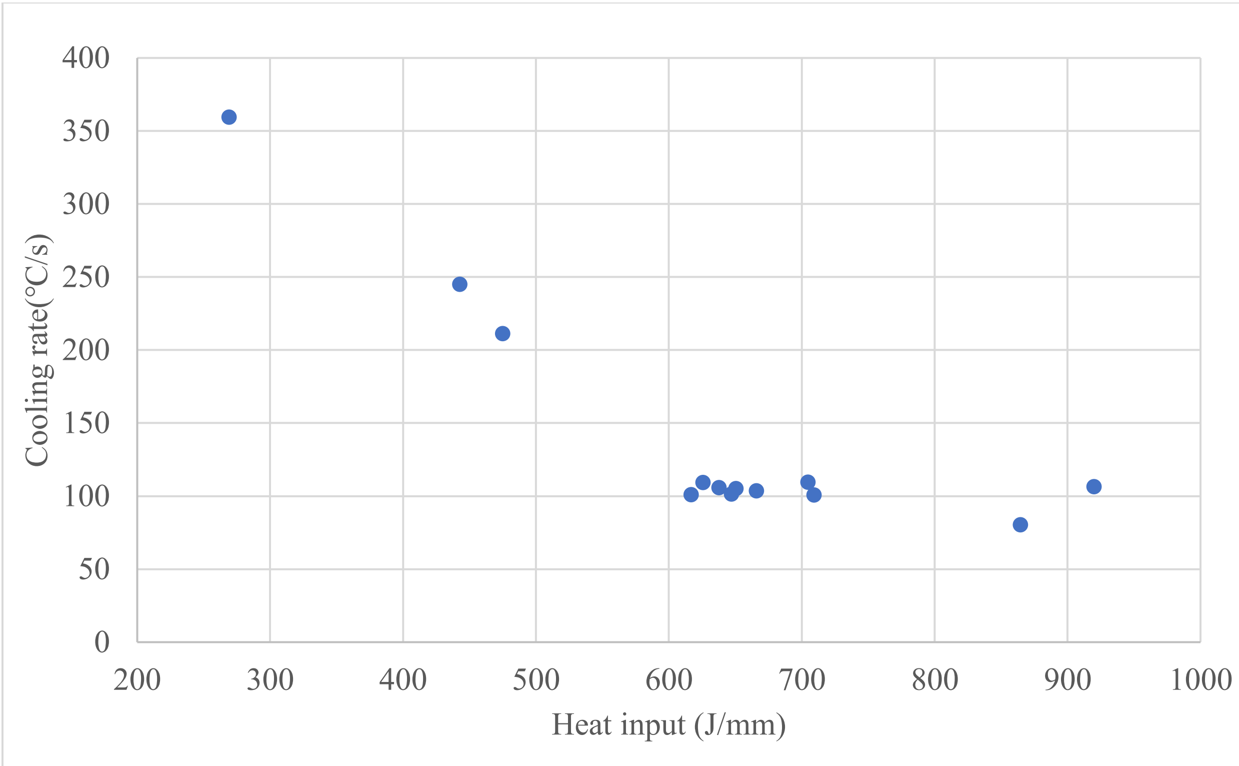

Figure 4-12: Predicted solidification cooling rate as a function of heat input.

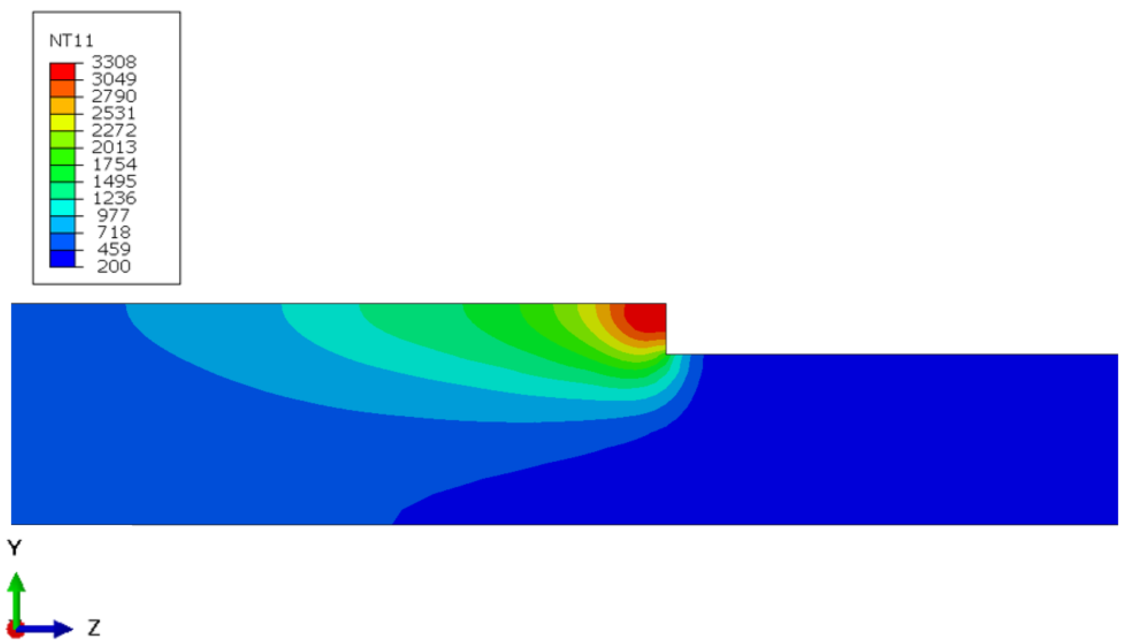

Figure 4-13: An example of an illustration for bead depth in the model.

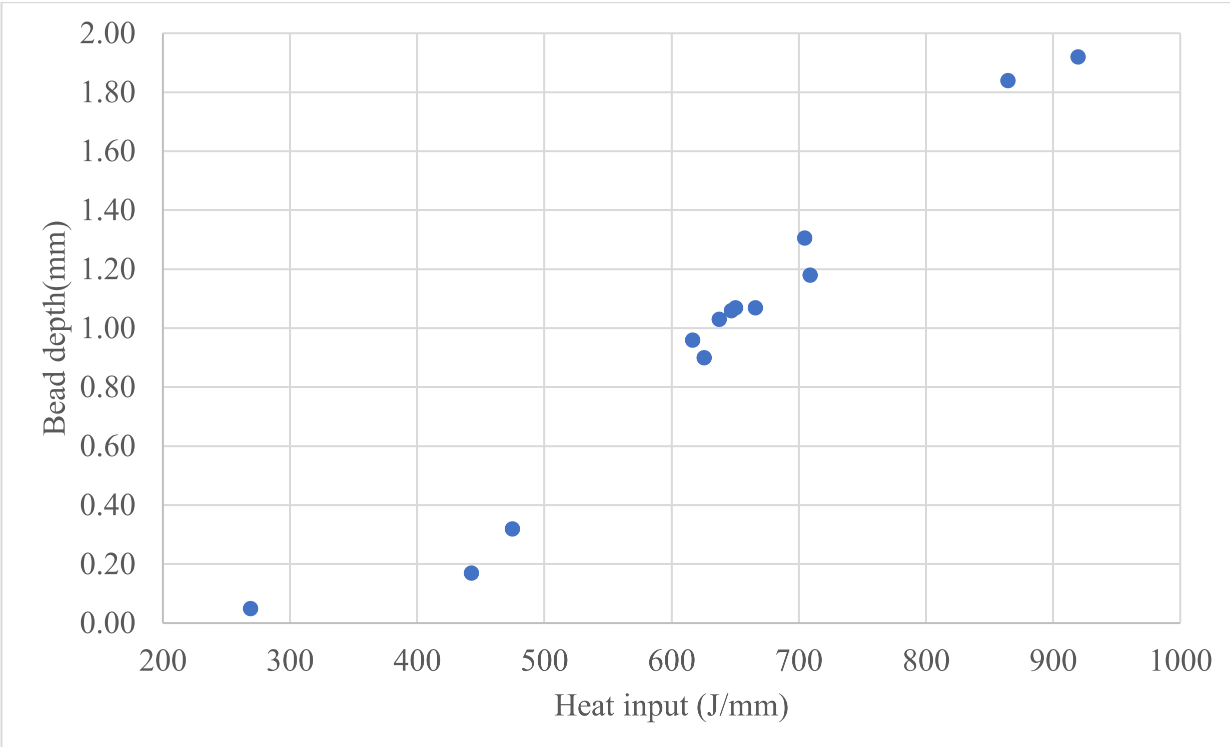

Figure 4-14: Bead depth as a function of heat input.

The prediction of bead depth for a WAAM process can be influenced by several process parameters, one of them being the heat input (as shown in Figure 4-14). As the heat input to the process increases, more heat is deposited into the material, which can lead to an increase in the bead depth, resulting in a thicker layer.

4.4 Validation of the model

4.4.1 Experimental setup

Experimental setup for a WAAM process typically involves the use of a robotic arm to control the movement of the arc and the material being deposited. The robotic arm holds the wire feeder and the torch that are used to melt and deposit the material. Figure 4-15 is an image of the experimental setup. The temperature measurements of the experiments are done by McDonald[2].

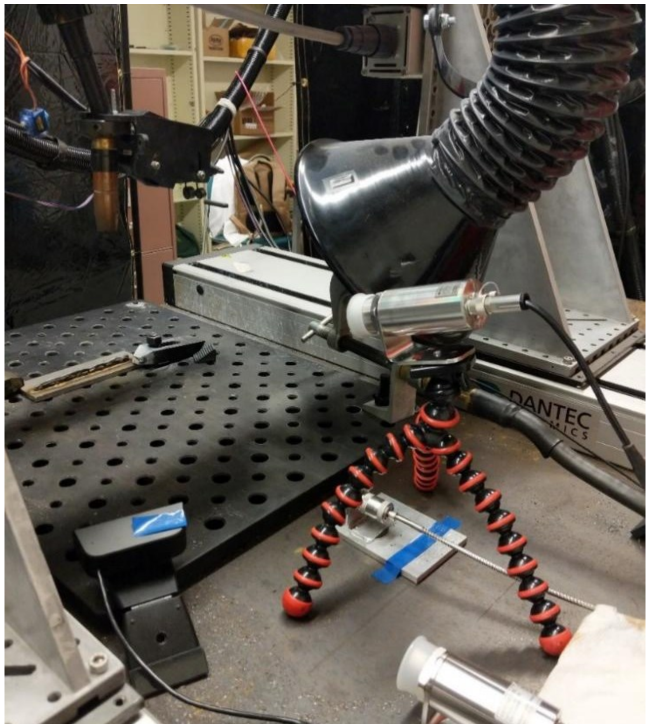

Figure 4-15: Experimental setup for WAAM process.

In addition to the robotic arm, an experimental setup for a WAAM process also typically includes several other key components, such as a motion control system, a power source for the arc, and a gas supply for shielding the arc. The gas used to shield the arc is argon at a flow rate of $2.75 \cdot 10^{-4}$ cubic meters per second.

Table 4-2: Composition of Exocor Executive 630 wire.

Element	**Wt. %**
C	0.01
Mn	0.2
Si	0.3
P	0.007
S	n.d.
Cu	4.3
Ni	4.1
Cr	16.4
O	0.06
Mo	0.01
N	0.02
Nb+Ta	0.3
Fe	Balance

The composition of the Exocor Executive 630 wire that was used as a feedstock is shown in Table 4-2. The wire is a 1.2 mm diameter 17-4PH stainless steel. An Optris CTRF2MH1SFVFC3 pyrometer is placed behind the build plate and aimed at the center of the bead. It is used to record the temperature data and compare it to the results obtained from the simulation.

To accurately predict a WAAM process using a finite element model in Abaqus, it is crucial that the geometry of the plate used in the simulation matches the geometry of the plate used in the experimental setup. This includes ensuring that the dimensions of the plate in the simulation (152mm x 51mm x 6mm) are the same as the dimensions of the plate used in the experiment. By doing so, any discrepancies in the results can be attributed solely to variations in the process parameters and not to differences in the plate geometry.

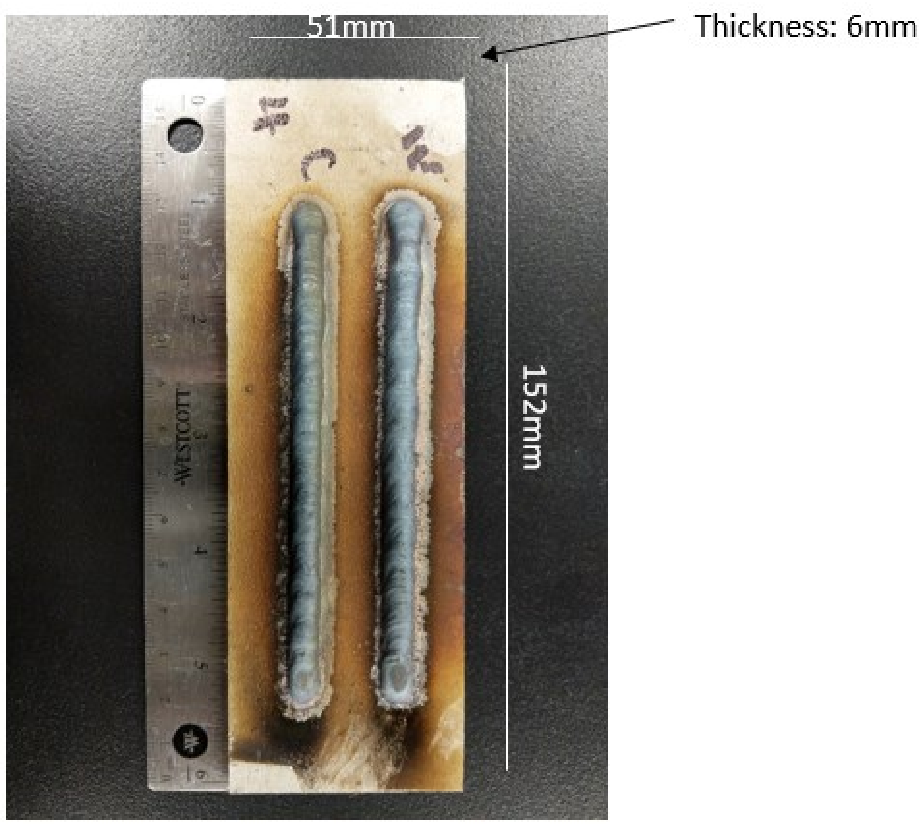

Figure 4-16: Geometry of the plate in the experiment.

Generally, two beads are run for each plate, as shown in Figure 4-16. The left bead, referred to as the cold bead, is used to record data under standard conditions, while the right bead, known as the warm bead, is run immediately after the cold bead, with the substrate preheated. So the second bead has a preheating temperature on the plate. It should be noted that the solidification cooling rate may vary due to the differences in temperature between the cold and warm conditions. In the simulation, as there is preheat, only the results under warm substrate conditions are compared with the simulation results.

4.4.2 Comparison of Abaqus prediction and experimental results

In this part, the results predicted by Abaqus are compared with the experimental results. A total of thirteen simulations were conducted with varying heat inputs, and the results were analyzed for comparison. In the experiments, 26 plates were produced, but only 19 of them had validated results. Of these 19 plates, 13 were selected for simulation and comparison, as the remaining six plates were repeated conditions, and the data for similar conditions was already available. Three comparisons are shown here (plate 5, plate 11 and 21). One is with low heat input. One is with middle heat inputs, and one is with high heat input. This allows for a comprehensive understanding of the relationship between heat input and the resulting solidification cooling rate.

The 5th plate in the experiment has a heat input of 269.1 J/mm. The simulation is under the same condition, and the temperature data is picked from a similar location as the experiment. Figure 4-17a shows the temperature profiles for both the ABAQUS prediction and experimental test. The maximum temperatures for the two cases have a difference of around 200℃. The plots end at a temperature around 550℃ because the pyrometer used in the experiment can only detect a temperature above 550℃. ℃. At around 1000℃, there is a slight deviation in the plots. Figure 4-17b is the illustration of the calculation of cooling rates. The graph represents a zoom-in of the region between the liquidus and solidus temperatures. The cooling rates are depicted as the slope of the plot. In order to give the plots mathematical significance, the time is reset to zero seconds when the steel is at the Liquidus temperature. This procedure is followed for all the analyses of solidification cooling rates. The simulation results have a solidification cooling rate of 359.5℃/s, while the experimental results give a solidification cooling rate of 375.4℃/s.

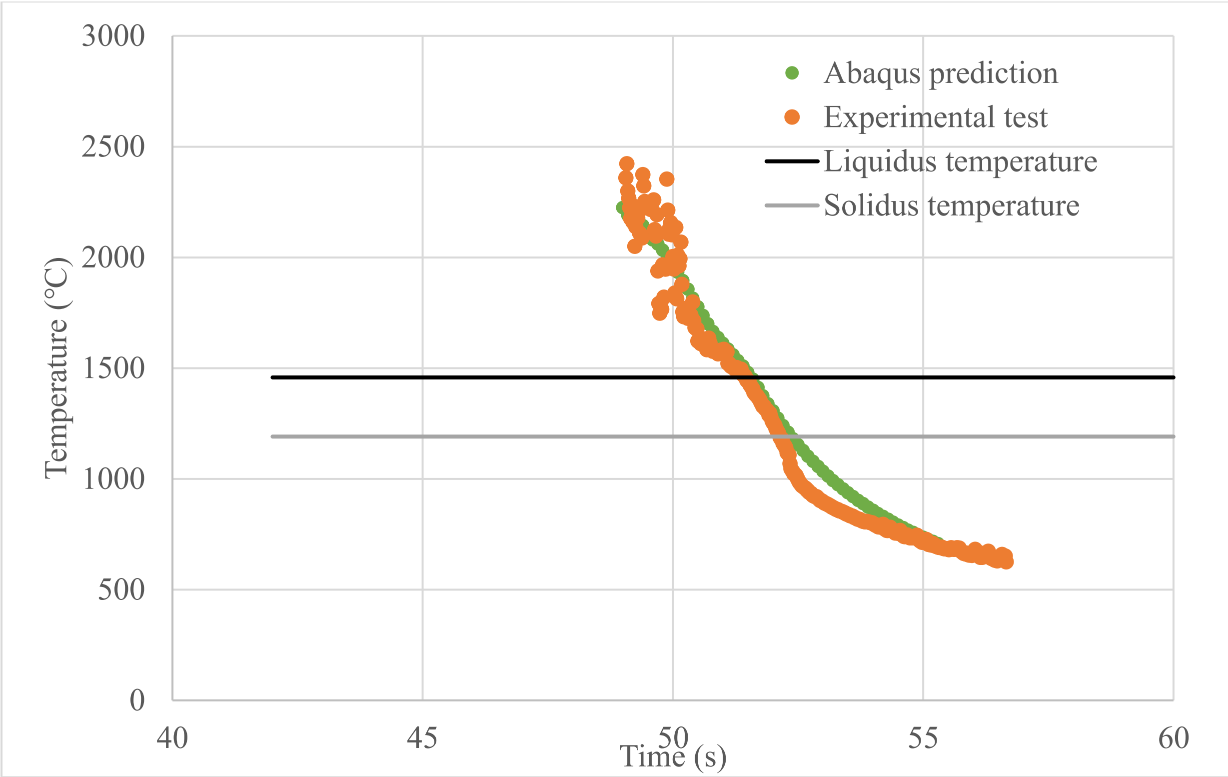

Figure 4-17a: Temperature profiles on the warm bead for the 5th plate.

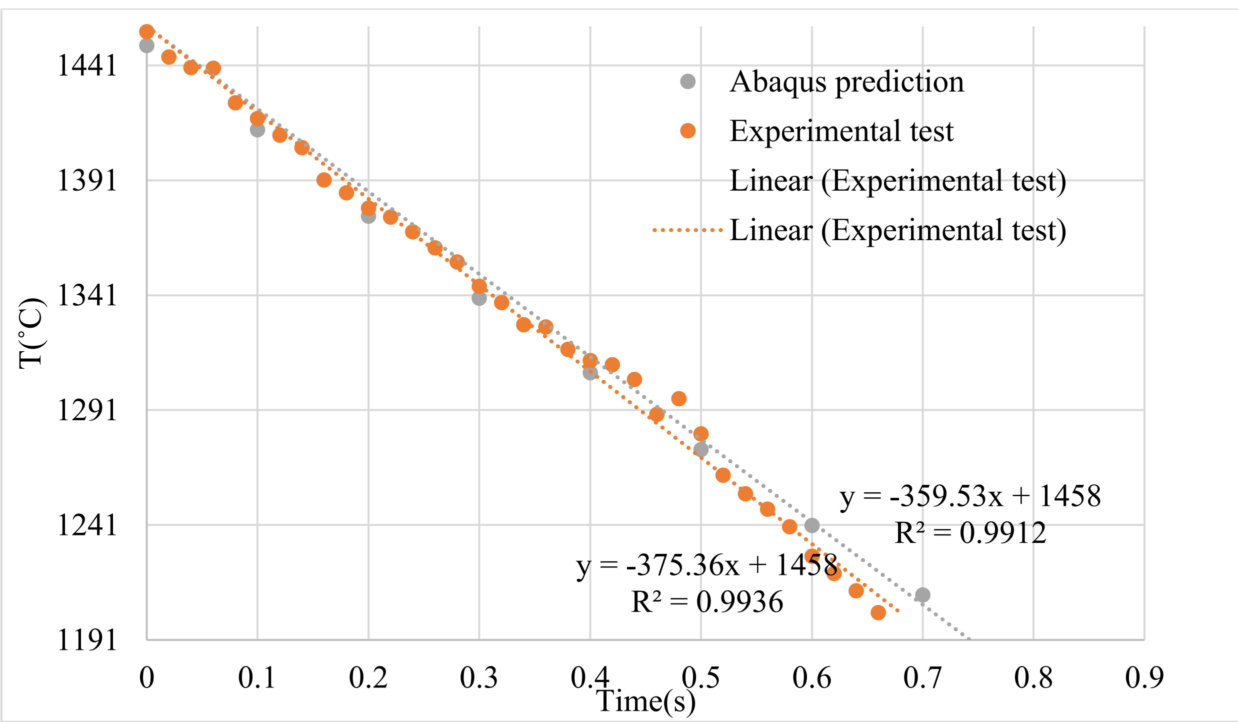

Figure 4-17b: Temperature profiles in the range of liquidus and solidus temperature on the warm bead for the 5th plate.

The comparison of the 11^{th} plate is shown in Figures 4-18a and 4-18b. As before, the temperature profiles are similar, indicating that the simulation prediction matches the experimental results. The cooling at the end of the process is slightly different, but the solidification cooling rates are very close.

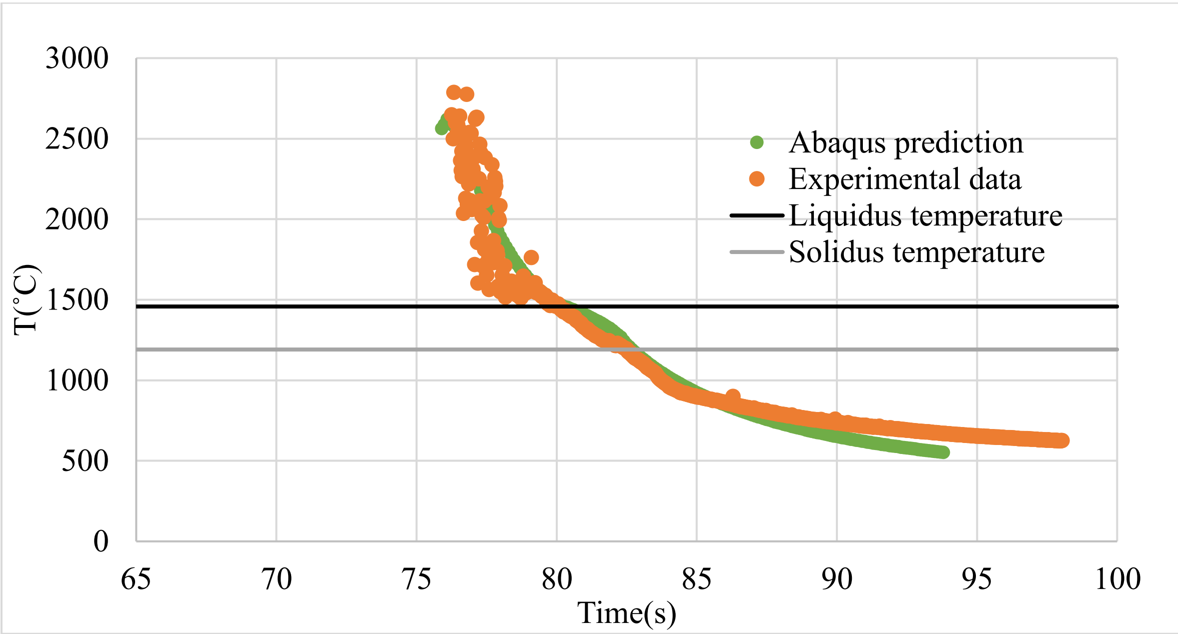

Figure 4-18a: Temperature profiles on the warm bead for the 11th plate.

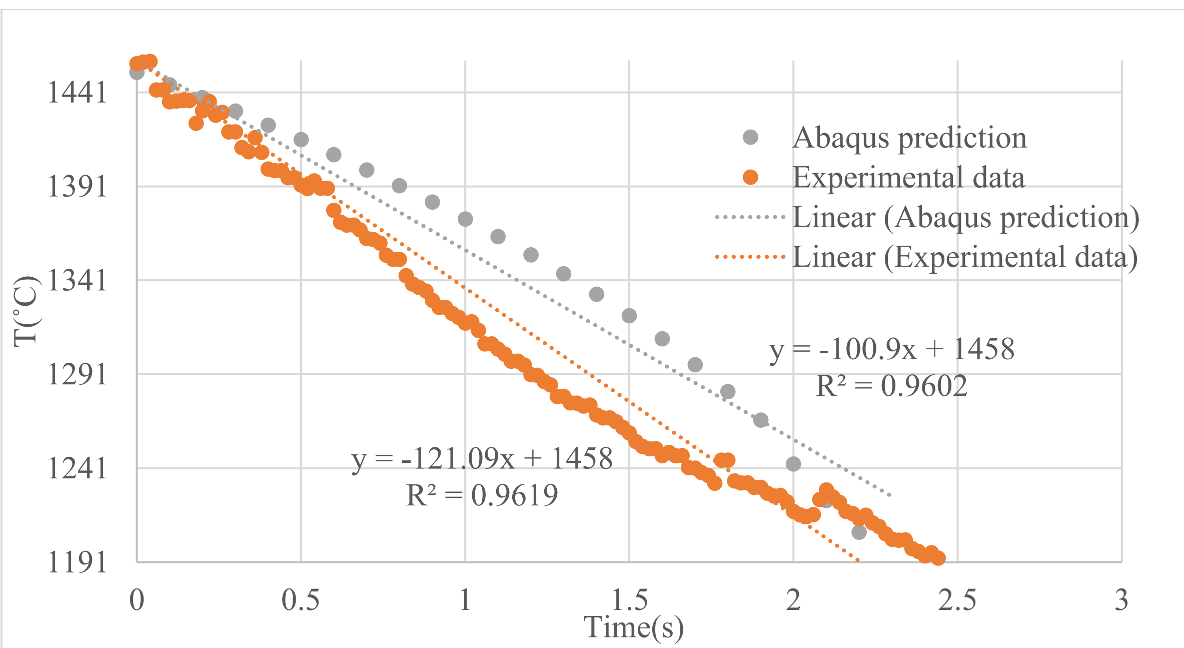

Figure 4-18b: Temperature profiles in the range of liquidus and solidus temperature on the warm bead for the 11th plate.

The comparison of a plate with higher heat input is shown in Figures 4-19a and b. It can be seen that the simulation predicts a higher maximum temperature than the experiment. This may be because some of the heat loss is not considered in the simulation. The prediction of the solidification cooling rates is a bit different. The temperature profile at the end is quite similar.

Figure 4-19b indicates that the cooling rate from liquidus to solidus of the experiment is 99.2℃/s while the solidification cooling rate of the prediction is 80.4℃/s. However, it is also observed that there is a flat part at a temperature of around 1450℃ during the cooling process. The temperature does not change for about 0.5 seconds during this flat part, resulting in a non-uniform solidification cooling rate before and after this point. The solidification cooling rate before the flat part is 89.5℃/s, which is closer to the predicted solidification cooling rate, while the solidification cooling rate after the flat part is around 181.5℃/s. The reason may be the pyrometer is not measuring the correct location on the sample.

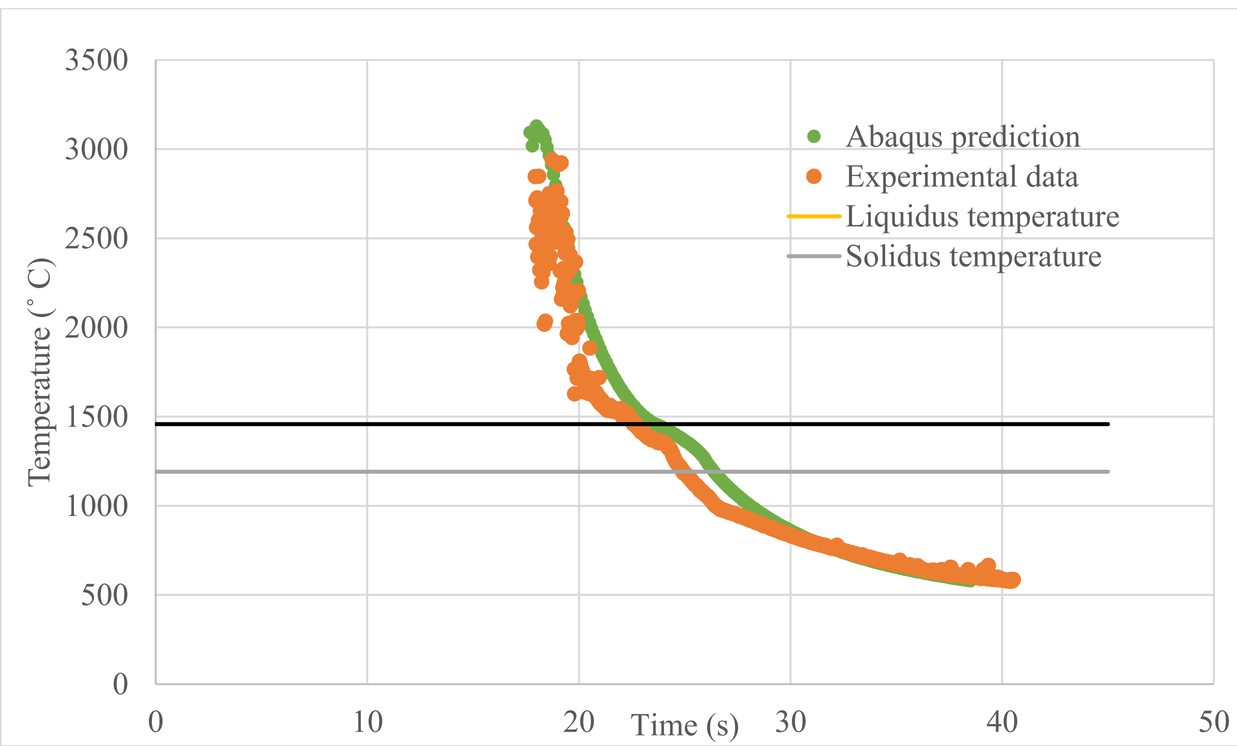

Figure 4-19a: Temperature profiles on the warm bead for the 21st plate.

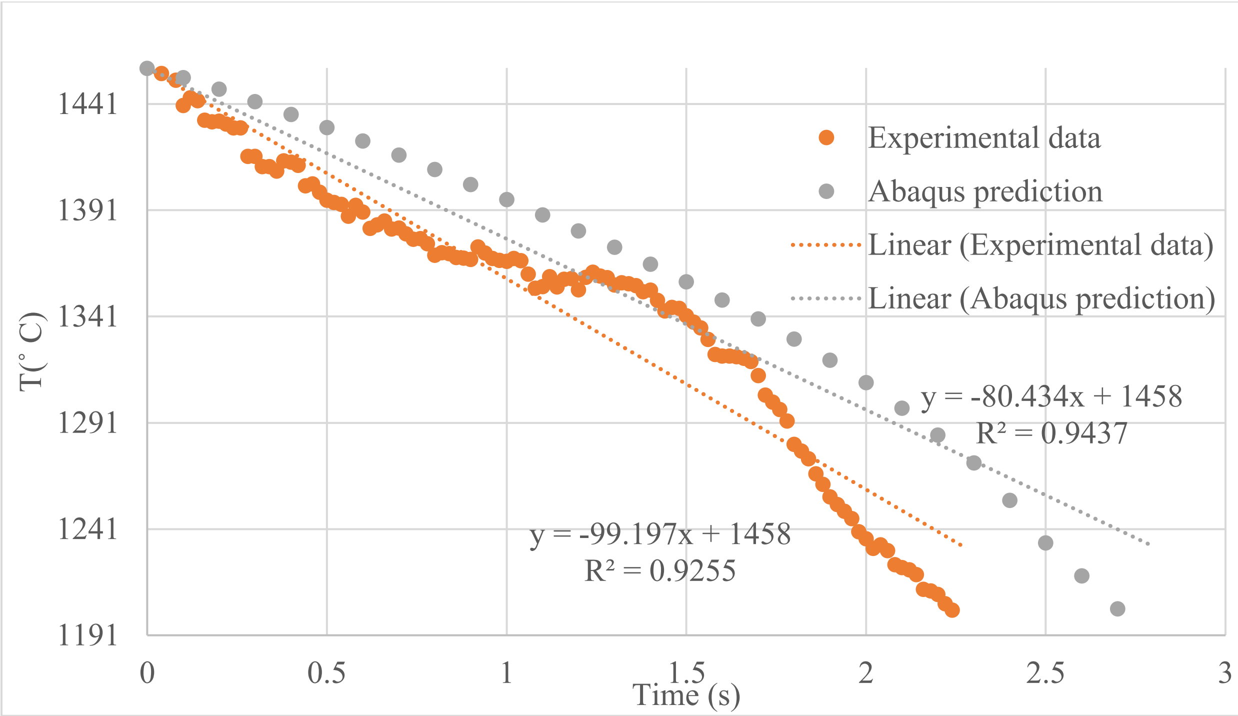

Figure 4-19b: Temperature profiles in the range of liquidus and solidus temperature on the warm bead for the 21st plate.

All the details for other comparisons of the rest of the plates can be seen in Appendix C.2. In the experiment, the bead depths are measured only for two of the plate. For the 4th plate, the bead depth is around 0.34mm, while in the simulation, it is 0.32mm. For the 21st plate, it is around 1.5mm, and the prediction is 1.8mm.

4.5 Summary

Figure 4-20 is the solidification cooling rate as a function of heat input for all thirteen plates. The solidification cooling rate decreases as the heat input increases. This relationship can be observed both in experimental results and in the results of the simulation, as indicated in Figure 4-20. The prediction of the solidification cooling rate is generally accurate for all the ranges of heat inputs. Additionally, the experimental setup or measurement errors can also contribute to the differences between the experimental results and the simulation predictions.

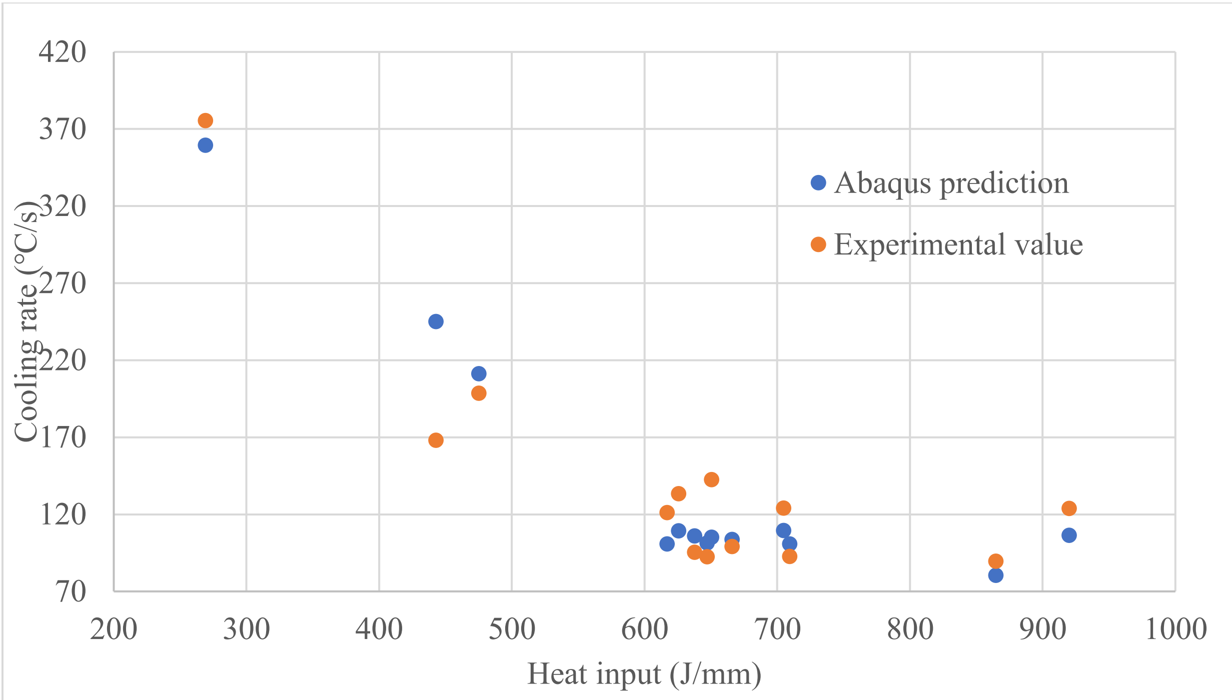

Figure 4-20: Solidification cooling rate as a function of heat input for both predictions and experiments.

Table 4-3 shows the details of the measurement. The error is a relative error that is calculated as follows:

$$Relative\ error = \left|\frac{Experimental\ value - Predicted\ value}{Predicted\ value}\right| \cdot 100\% \qquad (4\text{-}9)$$

The average relative error is 14.7 %, which can be accepted. This indicates that the simulation is able to accurately predict the cooling rate in the critical temperature range from liquidus to solidus, despite small discrepancies in the overall cooling process. The small difference in the solidification cooling rate could be due to various factors such as measurement errors, boundary conditions or material properties, and it's important to investigate the sources of the difference to improve the accuracy of the simulation. Overall, this comparison suggests that the simulation is able to provide a good estimate of the solidification cooling rate in the critical temperature range, which is essential to the understanding of the solidification process.

Table 4-3: Details of the measurement of Abaqus prediction and experimental data.

Plate	Heat input (J/mm)	Abaqus CR (°C/s)	Experimental CR (°C/s)	Error(%)	bead depth (mm)
4	475.00	211.20	198.5	6.01	0.32
5	269.08	359.50	375.4	4.42	0.05
7	442.76	245.00	168.1	31.39	0.17
11	616.81	100.90	121.1	20.0	0.96
12	665.94	103.70	99.2	4.34	1.07
15	637.68	105.90	95.4	9.92	1.03
17	647.05	101.40	92.4	8.88	1.06
18	650.55	105.10	142.5	37.4	1.07
19	625.67	109.30	133.4	22.05	0.90
21	864.57	80.40	89.5	11.3	1.84
23	704.72	109.60	124.4	14.4	1.31
24	709.21	100.70	92.6	8.04	1.18
25	919.84	106.50	123.9	16.34	1.92

This chapter has presented a method for simulating the temperature profile during WAAM using the AM Modeler in Abaqus. The simulation results have shown the temperature profile of the WAAM process, providing information about solidification cooling rates and bead depths. The chapter also discussed the validation process by comparing the simulation results with the experimental data collected from the pyrometer. The combination of experiments and simulations can provide a more comprehensive understanding of the thermal behaviour of the WAAM process, which can help to improve the quality and performance of the builds.

Chapter 5: Conclusions and future work

In this chapter, the conclusions of the research and potential future work are discussed.

5.1 Conclusions of this work

This study highlights the effectiveness of using AM Modeler in modelling welding and WAAM processes. It takes into account the heat transfer phenomena, including convection and radiation, by incorporating temperature-dependent thermo-physical properties, such as density, conductivities, and specific heat. However, before running the simulation, it is crucial to validate the parameters in Goldak's approach through multiple tests. To ensure accurate results, the initial temperature of the bead should be set near the liquidus temperature, and the preheating of the plate need to be simulated.

The simulation results of the SAW study will converge when the bead mesh size is reduced to around 0.6mm. The findings indicate that an increase in input power or a decrease in travel speed results in a higher peak temperature, wider bead width, and deeper penetration. Furthermore, the simulation results obtained from ABAQUS are in good agreement with both simulation results and experimental data from previous studies[1].

For the WAAM study, the convergence of results begins when the bead mesh size is reduced to approximately 0.8mm. The results clearly indicate a phase transition between the liquidus and solidus temperatures. Additionally, the results indicate that the cooling rate from liquidus to solidus decreases with increasing heat input while the penetration depth increases. The simulation results obtained using Abaqus also show good agreement with the experimental data obtained by McDonald [2].

5.2 Future work

Future work for the simulation of single-wire SAW includes the investigation of twin-wire SAW. This approach utilizes two wires instead of one, which allows for higher welding speeds and increased deposition rates. However, the simulation of twin-wire SAW will be more complex as there will be two layers to consider.

In addition, for the simulation of WAAM, the bead shape is currently assumed as a rectangle, but in the future, it could be assumed as a curve, which is closer to the real-world situation. The thermophysical properties of the material also play a significant role in the simulation results. To obtain more accurate results, a technique such as Differential Scanning Calorimetry (DSC) can be used to measure the heat flow associated with changes in a material's physical or chemical state. Furthermore, multiple-pass WAAM can be simulated to build up the final part and study the thermal effect of each layer.

In addition to this, the method of measuring temperature can also be varied and compared. For example, an infrared (IR) camera can be used as a non-contact measurement method, providing temperature variations across the surface of an object, whereas thermocouples and pyrometers typically provide only a single temperature reading.

Lastly, the geometry of the simulation can also be expanded to include pipes instead of plates. This would require the use of a cylindrical coordinate system. The simulation of the coordinates of deposition and heat source as a function of time would be more complex.

References

[1] A. Lecoanet. "Finite Element Model of the Thermal Profile During Submerged Arc Welding with One and Two Electrodes" A thesis submitted in partial fulfillment of the requirements for the degree of Master of Science in Chemical Engineering.2016

[2] McDonald, A. Exploring the effect of Cooling Rate on the Microstructure of Rapidly Solidified 17-4PH Stainless Steel. [MSc thesis, ongoing]. University of Alberta.

[3] "Physics of Welding and Cutting." WELDING HANDBOOK-Welding Science and Technology, by American welding society, edited by Cynthia L. Jenney and Annette O'Brien, p. 52.

[4] Www.twi-Global.com [Online] Available at: www.twi-global.com/technical-knowledge/faqs/what-is-arcwelding#:~:text= Arc%20welding%20is%20a%20type.

[5] Sindo Kou. Welding Metallurgy. Second ed., S.L., John Wiley, 2020, pp. 22–24.

[6] O'brien, Annette, et al. Welding Handbook. Volume 2. Welding Processes, Part 1. Vol. 256-258, Miami, Fl, American Welding Society, 2004.

[7] D. B. Holliday, et al. Welding Handbook Volume 2 Gas Metal Arc Welding. Miami, Fl, American Welding Society, 2001.

[8] Kou, Sindo. Welding Metallurgy. John Wiley & Sons, 31 Mar. 2003, pp. 19–22.

[9] Kou, S, and Y Wang. Weld Pool Convection and Its Effect Demonstrated for the First Time Are 3-D Convection in Moving Arc Weld Pools and Its Effect on Penetration, Segregation and Porosity. 2013.

[10] Wu, Joseph. A Basic Guide to Thermocouple Measurements Application Report a Basic Guide to Thermocouple Measurements. 2018.

[11] "Pyrometers: Non-Contact Temperature Measurement." Hotfoil-EHS, available at : blog.hotfoilehs.com/2017/08/pyrometers-non-contact-temperature.html

[12] Ofer. "Two Color Portable Pyrometer." Accurate Sensors Technologies, 14 Jan. 2019. Available at : www.accuratesensors.com/two-color-portable-pyrometer/.

[13] Chokkalingham, S., et al. "Artificial Neural Network Modeling for Estimating the Depth of Penetration and Weld Bead Width from the Infra Red Thermal Image of the Weld Pool during A-TIG Welding." Lecture Notes in Computer Science, vol. 6457, 2010, pp. 270–

278.

[14] Chokkalingham, S., et al. "Predicting the Depth of Penetration and Weld Bead Width from the Infra Red Thermal Image of the Weld Pool Using Artificial Neural Network Modeling." Journal of Intelligent Manufacturing, vol. 23, no. 5, 23 Mar. 2011, pp. 1995–2001.

[15] Zhang, De Fen, et al. "Investigation on Non-Preheating Welding Technology of X70 Pipeline Steel." Applied Mechanics and Materials, vol. 333-335, no. 1662-7482, July 2013, pp. 1836–1840.

[16] www.rolledalloys.com [Online] Available at: https://www.rolledalloys.com/wp-content/uploads/17-4_Data-sheet-rolled-alloys.pdf

[17] Kodama H. A scheme for three-dimensional display by automatic fabrication of three-dimensional model. J. IEICE 1981;64:1981–4.

[18] Jean-Claude A. Disdpositif pour realiser un modele de piece industrielle. National De La Propriete Industrielle; 1986.

[19] C.W. Hull, Apparatus for Production of Three-Dimensional Objects by Stereolithography US Patent Office (1984).

[20] Zhang, Jing, and Yeon-Gil Jung. Additive Manufacturing: Materials, Processes, Quantifications and Applications. Butterworth-Heinemann, 17 May 2018.

[21] McAndrew, A. et al. Interpass rolling of Ti-6Al-4V wire + arc additively manufactured features for microstructural refinement. Addit. Manuf. 2018, 21, 340–349.

[22] Ríos, Sergio, et al. "Analytical Process Model for Wire + arc Additive Manufacturing." Additive Manufacturing, vol. 21, May 2018, pp. 651–657.

[23] H. Geng, J. Xiong, D. Huang, X. Lin, J. Li, A prediction model of layer geometrical size in wire and arc additive manufacture using response surface methodology, Int. J. Adv. Manuf. Technol. 93 (1–4) (2017) 175–186.

[24] D. Ding, Z. Pan, D. Cuiuri, H. Li, A multi-bead overlapping model for robotic wire and arc additive manufacturing (WAAM), Rob. Comput. Integr. Manuf. 31 (2015) 101–110.

[25] "The Influence of Wire Properties on the Quality and Performance of Wire+Arc Additive Manufactured Aluminium Parts." Advanced Materials Research, vol. 1081, no. 1662-8985, Dec. 2014, pp. 210–214.

[26] Dinovitzer, Malcolm, et al. "Effect of Wire and Arc Additive Manufacturing (WAAM) Process Parameters on Bead Geometry and Microstructure." Additive Manufacturing, vol.

26, Mar. 2019, pp. 138–146.

[27] Ou, W., et al. "Fusion Zone Geometries, Cooling Rates and Solidification Parameters during Wire Arc Additive Manufacturing." International Journal of Heat and Mass Transfer, vol. 127, 1 Dec. 2018, pp. 1084–1094.

[28] Rosli, Nor Ana, et al. "Review on Effect of Heat Input for Wire Arc Additive Manufacturing Process." Journal of Materials Research and Technology, vol. 11, Mar. 2021, pp. 2127–2145.

[29] Gudur, Srinath, et al. "A Study on the Effect of Substrate Heating and Cooling on Bead Geometry in Wire Arc Additive Manufacturing and Its Correlation with Cooling Rate." Materials Today: Proceedings, vol. 41, 2021, pp. 431–436.

[30] Rosenthal, D. "The Theory of Moving Sources of Heat and Its Application to Metal Treatments." Journal of Fluids Engineering, vol. 68, no. 8, 1 Nov. 1946, pp. 849–865.

[31] R.R. Rykalin, Energy sources for welding, Weld. World 12 (1974) 227–248.

[32] Eager, T. W., and Tsai, N. S.: Temperature Fields Produced by Traveling Distributed Heat Sources, Welding Journal, 62[12] (1983) 346

[33] Nguyen,N.T., Ohta,A., Suzuki,N., Maeda,Y., Analytical Solutions for Transient Temperature of Semi-Infinite Body Subjected to 3-D Moving Heat Source, Welding Journal, August 1999, 265.

[34] Wu, Joseph. A Basic Guide to Thermocouple Measurements Application Report a Basic Guide to Thermocouple Measurements. 2018.

[35] "Pyrometers: Non-Contact Temperature Measurement." Hotfoil-EHS, available at : blog.hotfoilehs.com/2017/08/pyrometers-non-contact-temperature.html

[36] Kik, Tomasz. "Heat Source Models in Numerical Simulations of Laser Welding." Materials, vol. 13, no. 11, 10 June 2020, p. 2653.

[37] Kempf, Volker. "Approximated Analytical Approach for Temperature Calculation in Pulsed Arc Welding." International Journal on Interactive Design and Manufacturing (IJIDeM), vol. 14, no. 2, 1 Nov. 2019, pp. 675–681.

[38] Roshyara, Nab Raj, et al. "Approximate Analytical Solution for the Temperature Field in Welding." Metallurgical and Materials Transactions B, vol. 42, no. 6, 21 July 2011, pp. 1253–1273.

[39] Www.twi-Global.com [Online] Avalible at:

www.twi-global.com/technical-knowledge/faqs/faq-what-is-the-difference-between-heat-input-and-arc-energy.

[40] Akbari, D., and I. Sattari-Far. "Effect of the Welding Heat Input on Residual Stresses in Butt-Welds of Dissimilar Pipe Joints." International Journal of Pressure Vessels and Piping, vol. 86, no. 11, Nov. 2009, pp. 769–776.

[41] Shanmugam, N. Siva, et al. “A Transient Finite Element Simulation of the Temperature and Bead Profiles of T-Joint Laser Welds.” Materials & Design, vol. 31, no. 9, 1 Oct. 2010, pp. 4528–4542.

[42] Dhinakaran, V, et al. “Analytical and Numerical Investigations of Weld Bead Shape in Plasma Arc Welding of Thin Ti-6al-4v Sheets.” SIMULATION, vol. 93, no. 12, 30 Aug. 2017, pp. 1123–1138.

[43] Pathak, AK; Datta, GL. PROCEEDINGS OF THE INSTITUTION OF MECHANICAL ENGINEERS PART B-JOURNAL OF ENGINEERING MANUFACTURE; MAR 2004; 218; 3; p269-p280.

[44] Chun-yan Yan; Li-chao Wu; Chen-xia Kan; Ming-gui Xu; Gen-yuan Zhang; "FE Analysis of Temperature Field in A Twin-wire Tandem Submerged Arc Welded X80 Steel Pipe", DESTECH TRANSACTIONS ON COMPUTER SCIENCE AND ENGINEERING, 2018.

[45] Wen, S. W., et al. "Finite Element Modelling of a Submerged Arc Welding Process." Journal of Materials Processing Technology, vol. 119, no. 1, 20 Dec. 2001, pp. 203–209.

[46] Nart, Ergun, and Yuksel Celik. "A Practical Approach for Simulating Submerged Arc Welding Process Using FE Method." Journal of Constructional Steel Research, vol. 84, May 2013, pp. 62–71.

[47] Nezamdost, M. R., et al. "Investigation of Temperature and Residual Stresses Field of Submerged Arc Welding by Finite Element Method and Experiments." The International Journal of Advanced Manufacturing Technology, vol. 87, no. 1-4, 27 Feb. 2016, pp. 615–624.

[48] Xiong, Jun, et al. "Finite Element Analysis and Experimental Validation of Thermal Behavior for Thin-Walled Parts in GMAW-Based Additive Manufacturing with Various Substrate Preheating Temperatures." Applied Thermal Engineering, vol. 126, Nov. 2017, pp. 43–52.

[49] Wu, Qianru, et al. "Effect of Molten Pool Size on Microstructure and Tensile Properties of

Wire Arc Additive Manufacturing of Ti-6Al-4V Alloy." Materials, vol. 10, no. 7, 4 July 2017, p. 749.

[50] Realistic Simulation with Abaqus Unified FEA. ABAQUS Unified FEA.

[51] Mena, Edison A. Bonifaz* and Andres, et al. "A Directed Energy Deposition Additive Manufacturing Process Simulated with ABAQUS AM Modeler." International Journal of Robotic Engineering, vol. 6, no. 1, 7 Aug. 2021.

[52] Song, Xu, et al. "Advances in Additive Manufacturing Process Simulation: Residual Stresses and Distortion Predictions in Complex Metallic Components." Materials & Design, vol. 193, 1 Aug. 2020, p. 108779.

[53] Michalski, Jakub. "Additive Manufacturing Simulations in Abaqus - Update." Info.simuleon.com, 23 June 2022, info.simuleon.com/blog/additive-manufacturing-simulations-in-abaqus.

[54] Abaqus/CAE User's Manual. Available at: http://130.149.89.49:2080/v6.11/books/usi/default.htm?startat=pt03ch17s08s01.html

[55] Abaqus/CAE User's Manual. Available at: http://130.149.89.49:2080/v6.11/books/usi/default.htm?startat=pt03ch17s17s02.html

[56] Packard, Keith. "Metallurgy for Welders." Www.thefabricator.com, 25 May 2012.

[57] Gnielinski, V., Int. Chem. Eng., 16, 359, 1976.

[58] Winterton, R.H.S. (February 1998). "Where did the Dittus and Boelter equation come from?" International Journal of Heat and Mass Transfer. Elsevier. 41 (4–5): 809–810.

[59] Sieder, E. N., and G. E. Tate, Ind. Eng. Chem., 28, 1429, 1936.

[60] K. Mundra , T. DebRoy & K. M. Kelkar2 (1996) NUMERICAL PREDICTION OF FLUID FLOW AND HEAT TRANSFER IN WELDING WITH A MOVING HEAT SOURCE, Numerical Heat Transfer, Part A Applications, 29:2, 115-129.

Appendix A

A.1. Thermophysical properties for X70

X70 is the material used in SAW. The thermophysical properties for X70 are the same as in the previous research [1], which are temperature dependant. The following figures show the density, specific heat, and thermal conductivities as a temperature function.

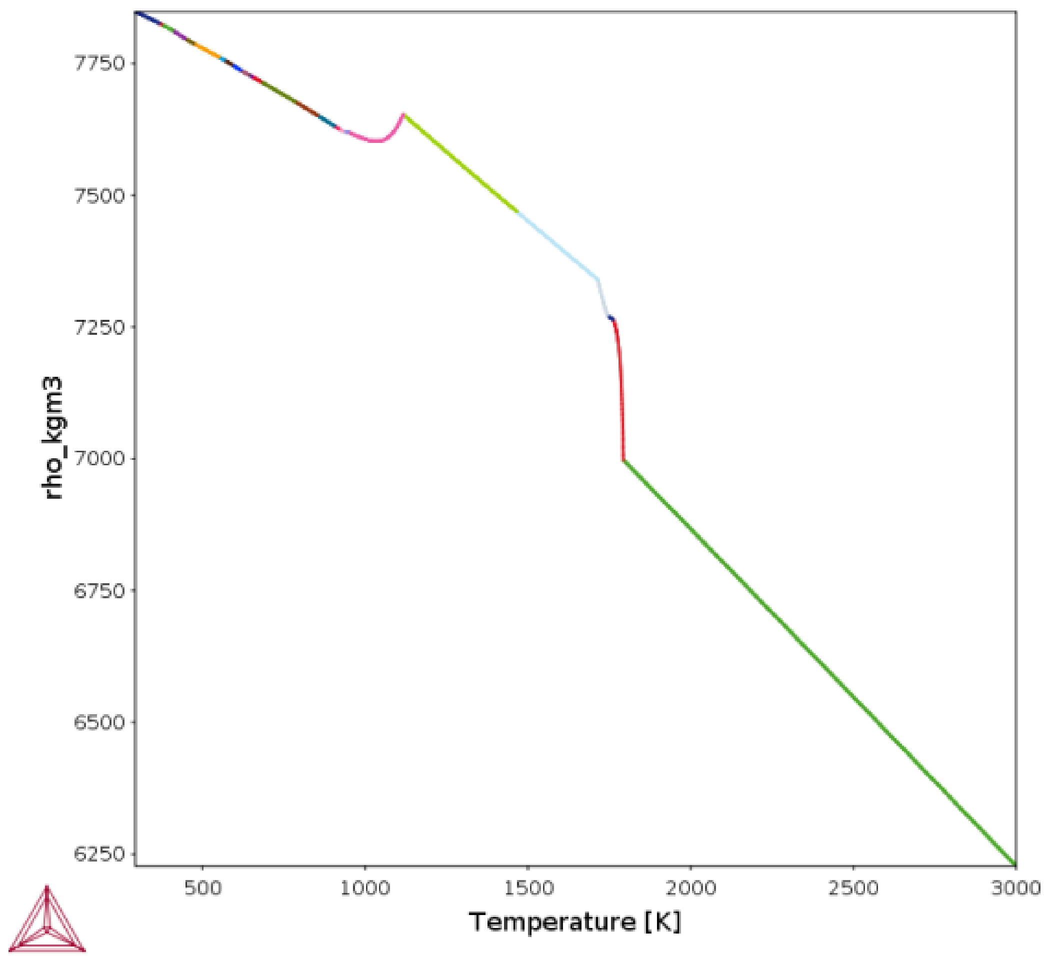

Figure A.1: Density as a function of temperature given by Thermo-Calc. [1]

The software does not provide the density directly, but it does provide the mass and volume of the system. To calculate the density, a function was defined within the software that calculates the ratio of mass to volume.

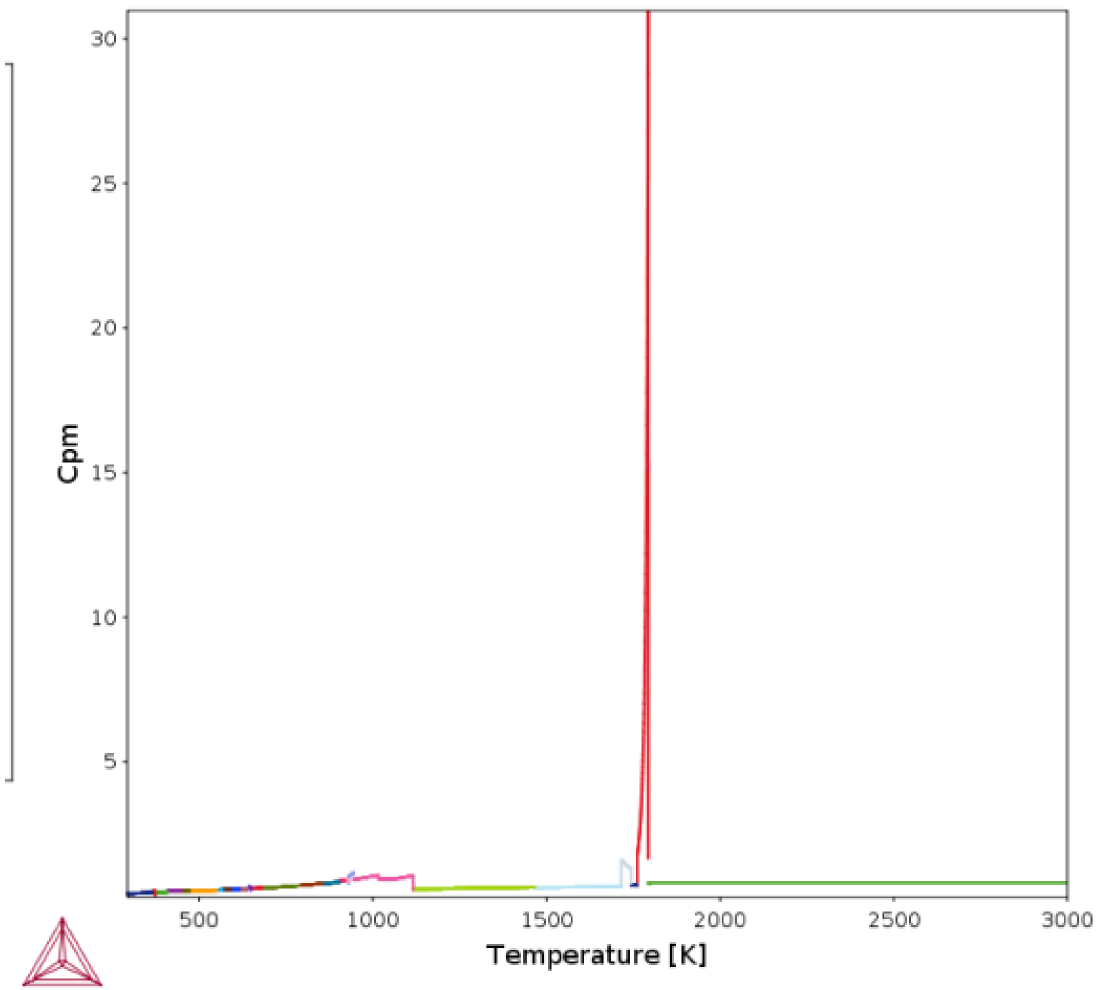

Figure A.2: Derivative of Enthalpy(J/g.K) as a function of temperature given by Thermo-Calc. [1]

In this project, the derivative of enthalpy with respect to temperature was utilized. A custom function was implemented in the software to calculate this derivative, which provided the heat capacity of the system.

Figure A.3 illustrates the combination of the thermal conductivity of the solid phase and the thermal conductivity of the liquid phase.

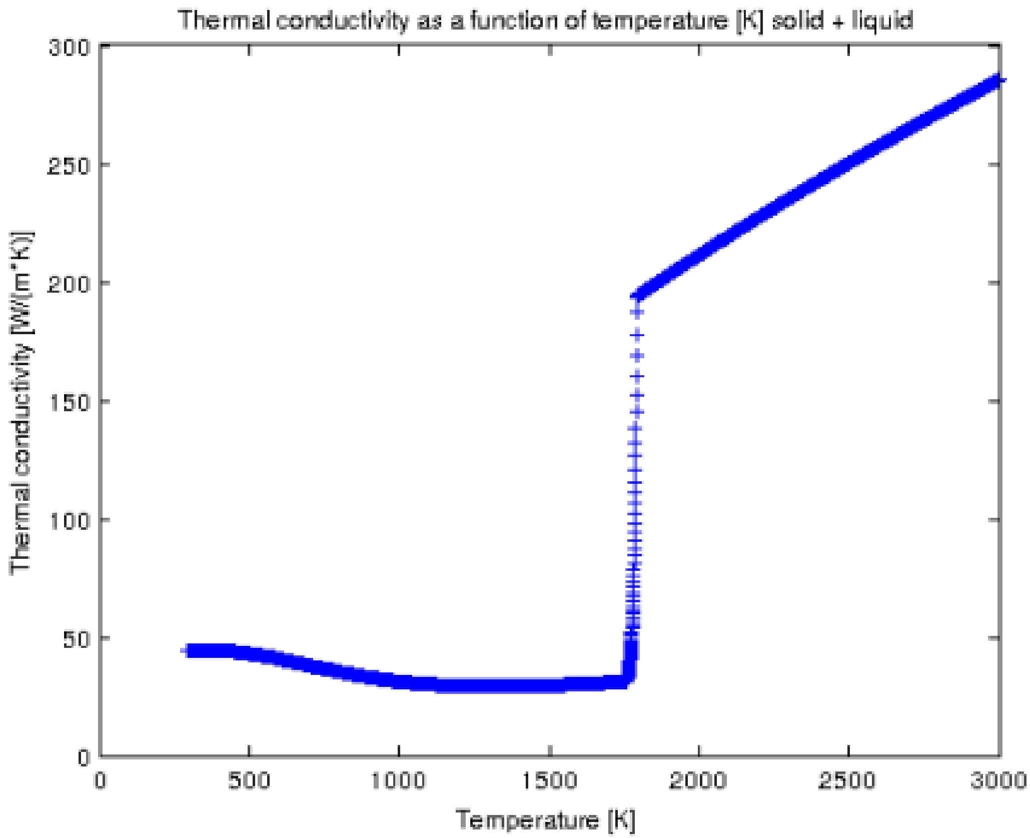

Figure A.3: Thermal conductivity as a function of temperature given by Thermo-Calc. [1]

A.2. Thermophysical properties for 17-4 PH

The thermal conductivity is obtained in the site of Rolled Alloy [16]. Table A.1 shows the values with different temperatures.

Table A. 1: Thermal conductivity of 17-4PH for different temperatures.

Temperature (°C)	Thermal conductivity (W/(m.K))
21	15
100	16
200	17
300	18

The density of the material can be seen to change within the liquidus to solidus temperature range as shown in Figure A.4, and it is observed to decrease with an increase in temperature.

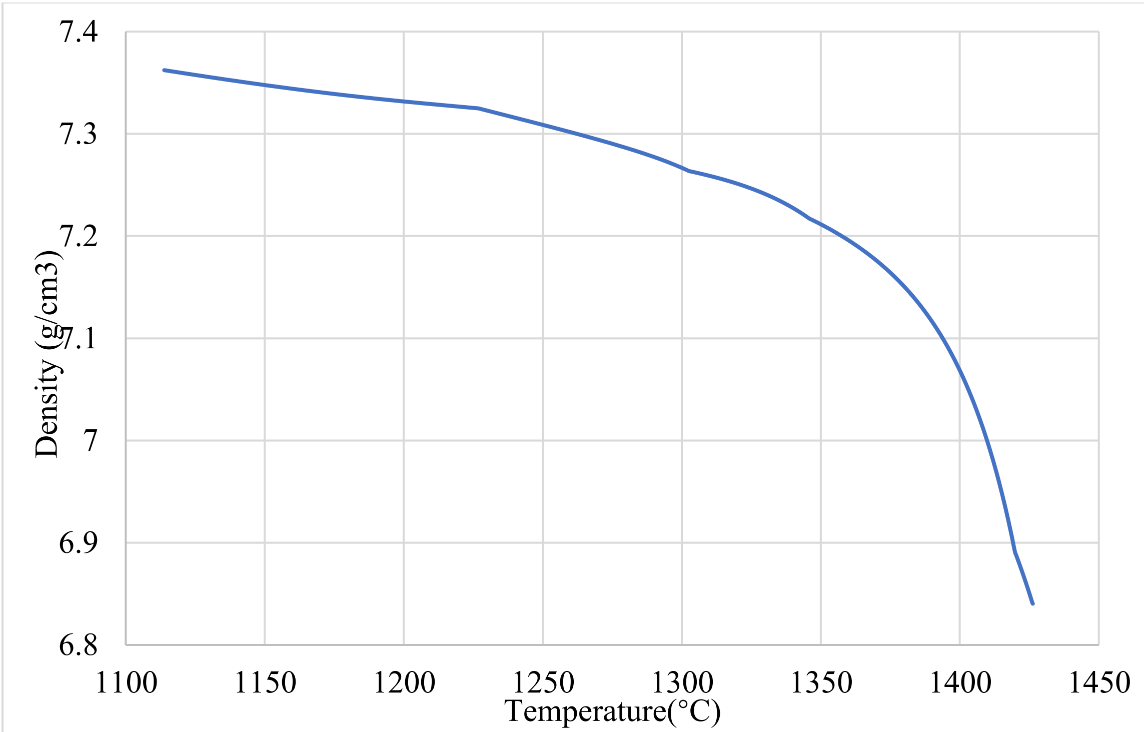

Figure A.4: Density as a function of temperature.

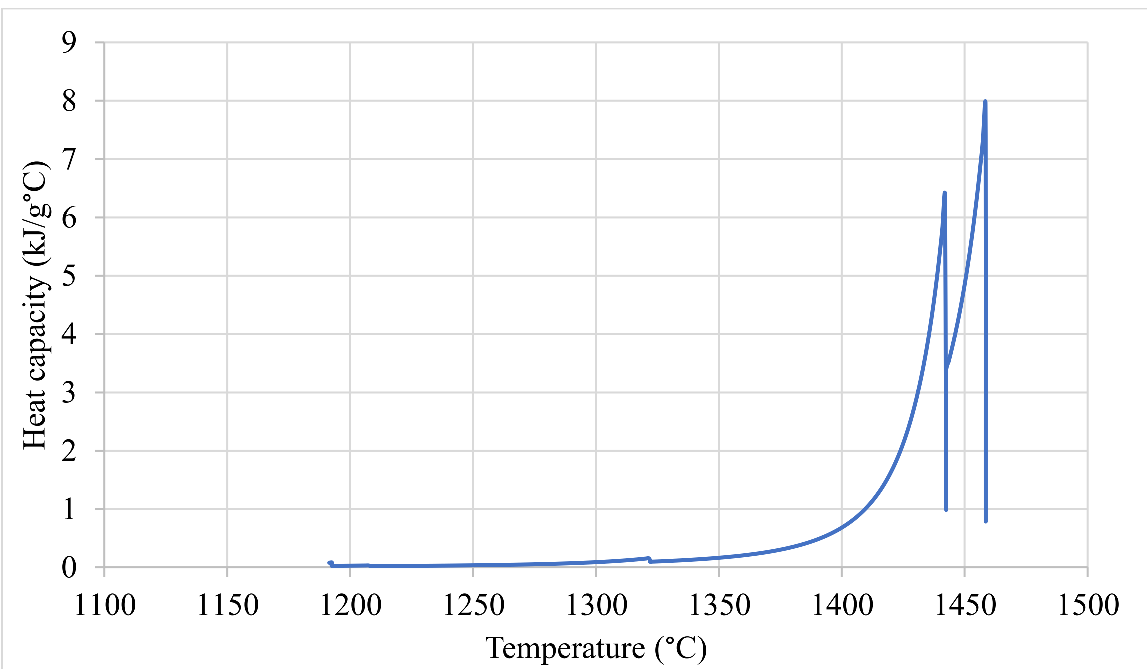

Figure A.5: Heat capacity as a function of temperature.

In Figure A.5, the material's heat capacity is plotted against temperature. The notable peaks and breaks in the graph correspond to the phase transitions of the material.

Appendix B

B.1. Goldak parameters used in SAW simulation

The Goldak parameters used in SAW is shown in Table B.1

Table B. 1: Goldak parameters used in SAW

a	b	c_f	c_r	f_f	f_r
12	9	4	8	0.67	1.33

B.2. Goldak parameters used in WAAM simulation

The Goldak parameters used in WAAM is shown in Table B.2

Table B. 2: Goldak parameters used in WAAM

a	b	c_f	c_r	f_f	f_r
2.5	8.5	2.5	5	0.67	1.33

Appendix C

C.1 Experimental settlements for SAW in the previous research

In Figure C.1, the dimensions of the plate that contains the embedded thermocouples are displayed. The locations and designations of the various thermocouples in each zone are depicted. To identify a particular thermocouple, the notation provided in Figure C.1 is employed, followed by the letter "Z" and the zone number in which the thermocouple is situated. For example, to refer to thermocouple Kb in zone 2, the notation KbZ2 is utilized, and for thermocouple B in zone 1, the notation BZ1 is utilized.

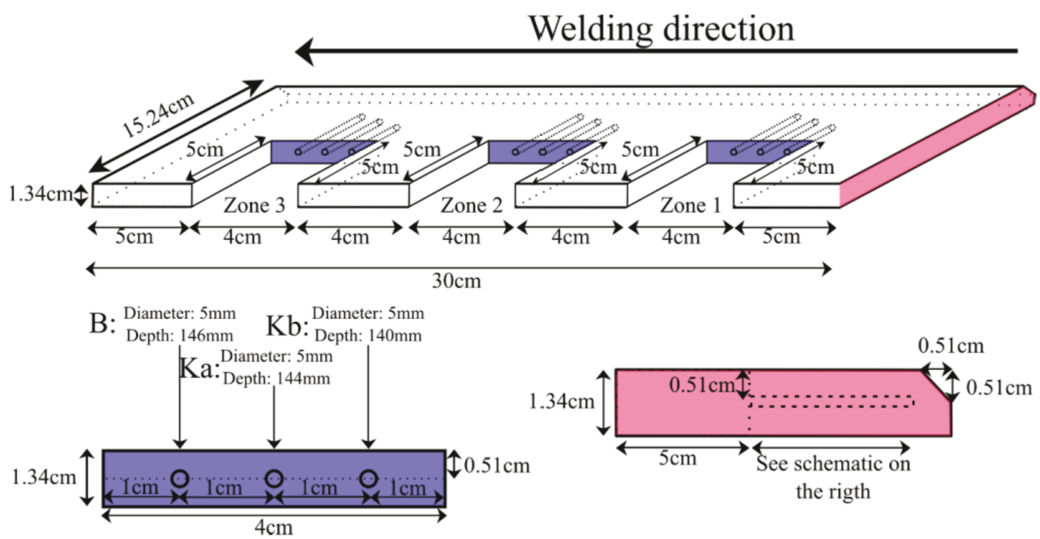

Figure C.1: Geometry of the machined plate, with the positions of the thermocouples[1]

Figure C.2 is an image of the nine cross-sections. From this image, the bead width, maximum reinforcement height, maximum penetration depth and the distance between the centre of the plate and the centre weld can be measured. The positions of the thermocouples can also be seen.

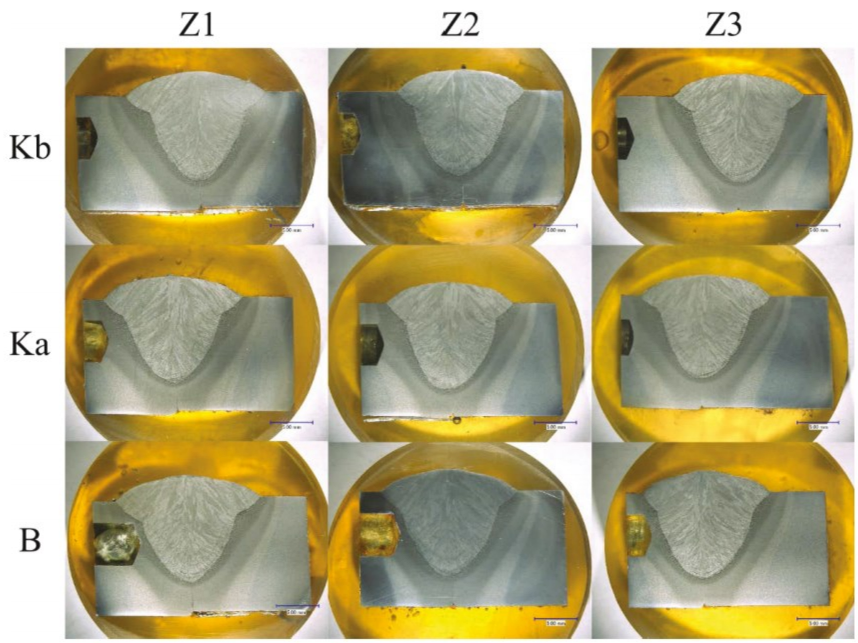

Figure C.2: An example of polished and etched cross-sections presented in previous research.[1]

C.2. Simulation results for WAAM from ABAQUS

The comparisons of ABAQUA prediction and experimental data for the thirteen plates are all shown in this section.

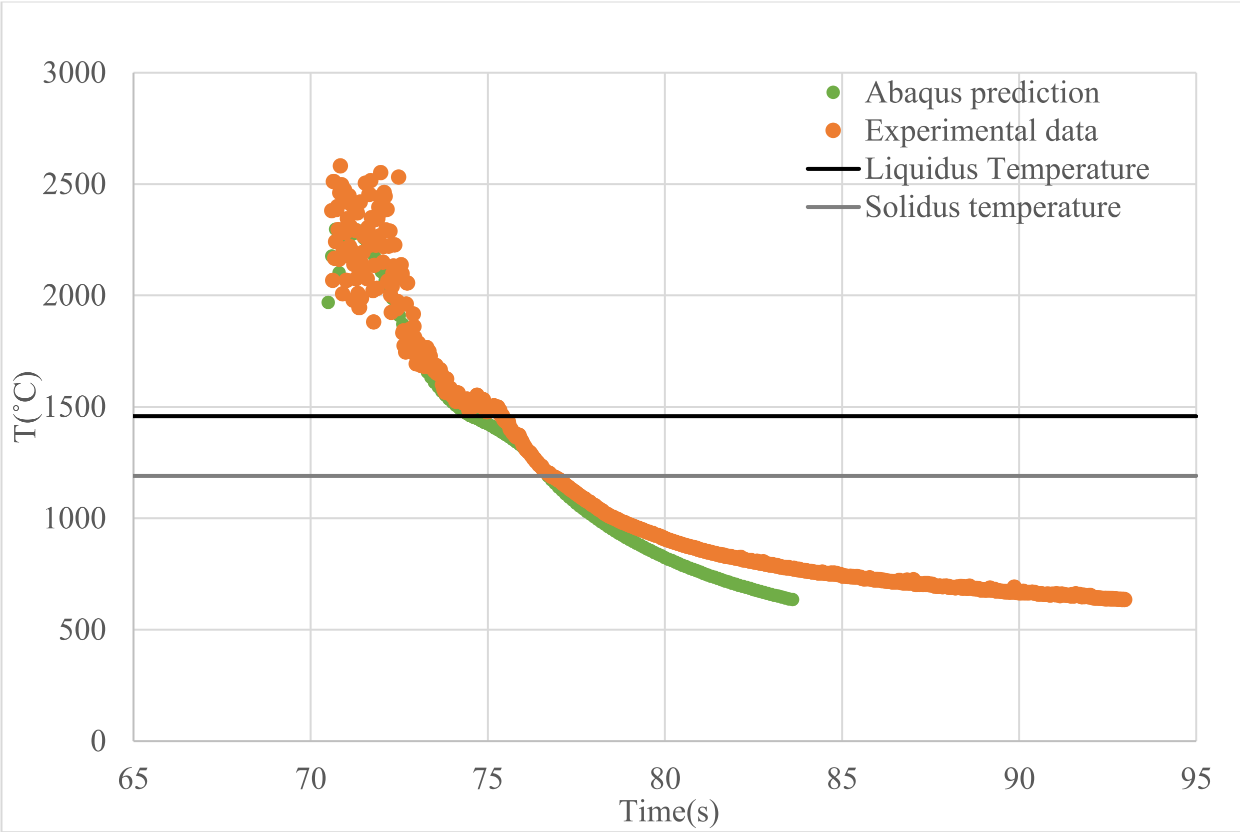

Figure C.3a: Temperature profiles for the 4th plate.

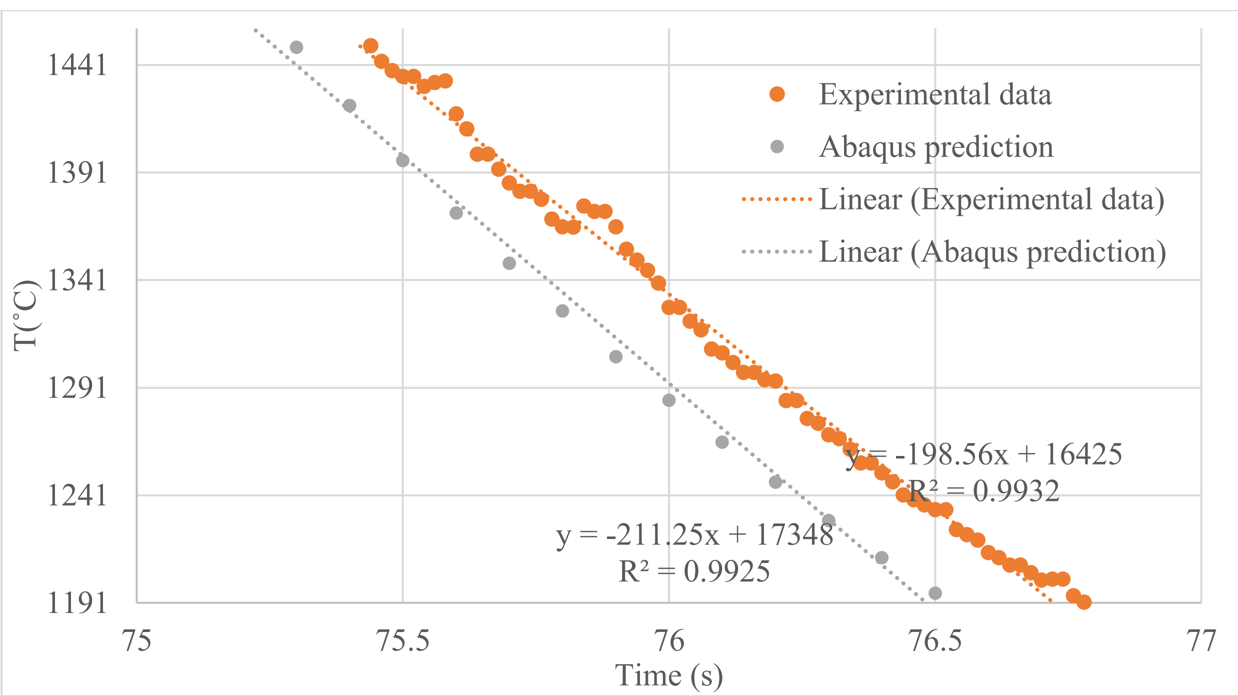

Figure C.3b: Temperature profiles in the range of liquidus and solidus temperature for the 4th plate.

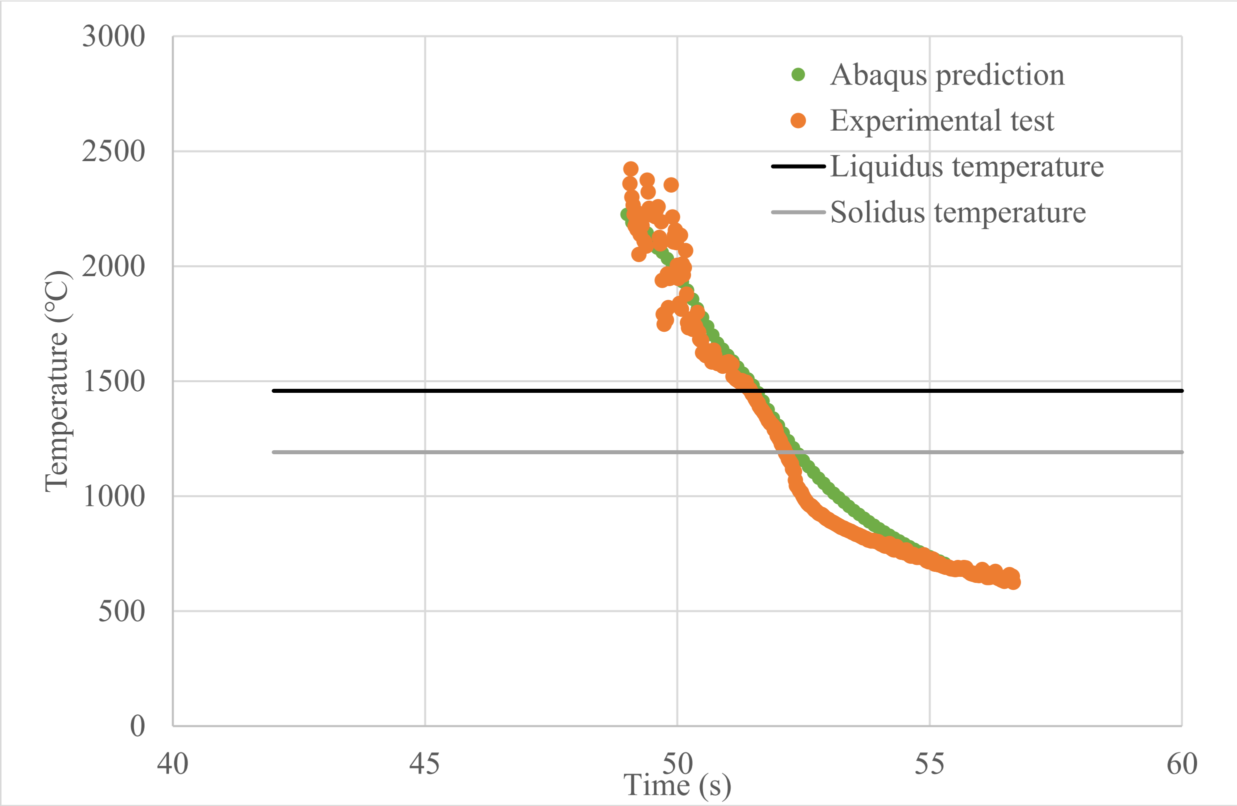

Figure C.4a: Temperature profiles for the 5th plate.

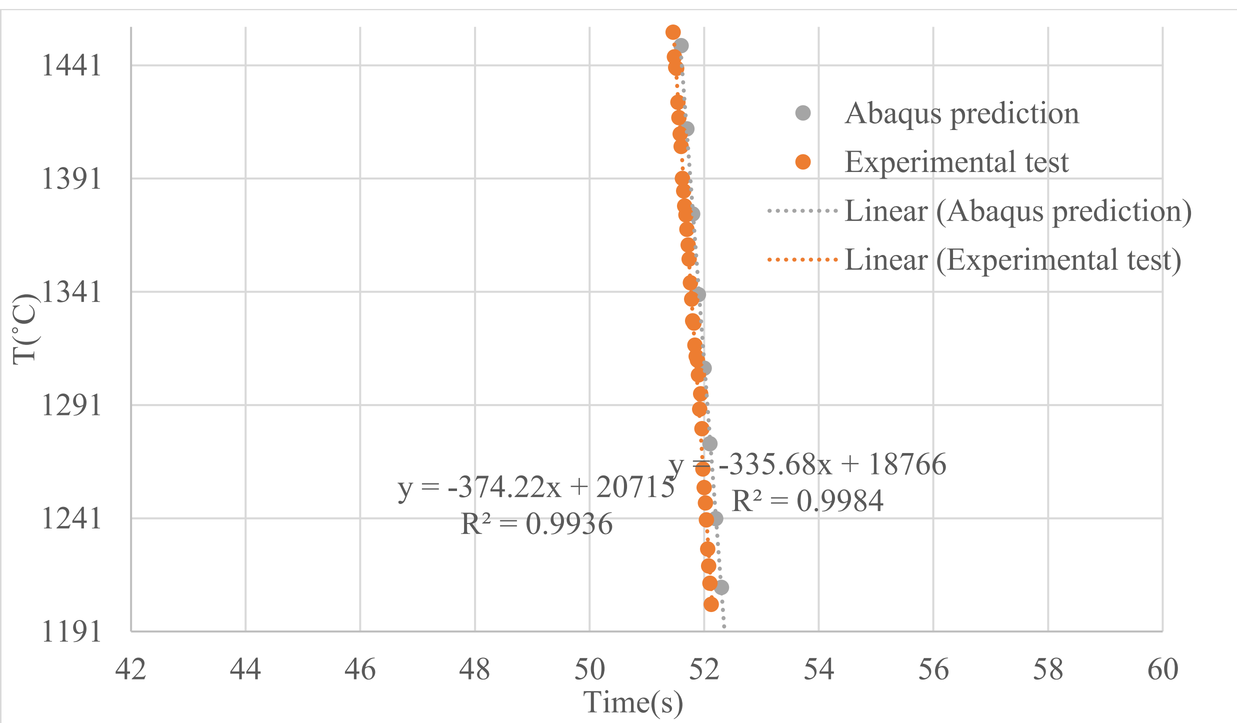

Figure C.4b: Temperature profiles in the range of liquidus and solidus temperature for the 5th *plate.*

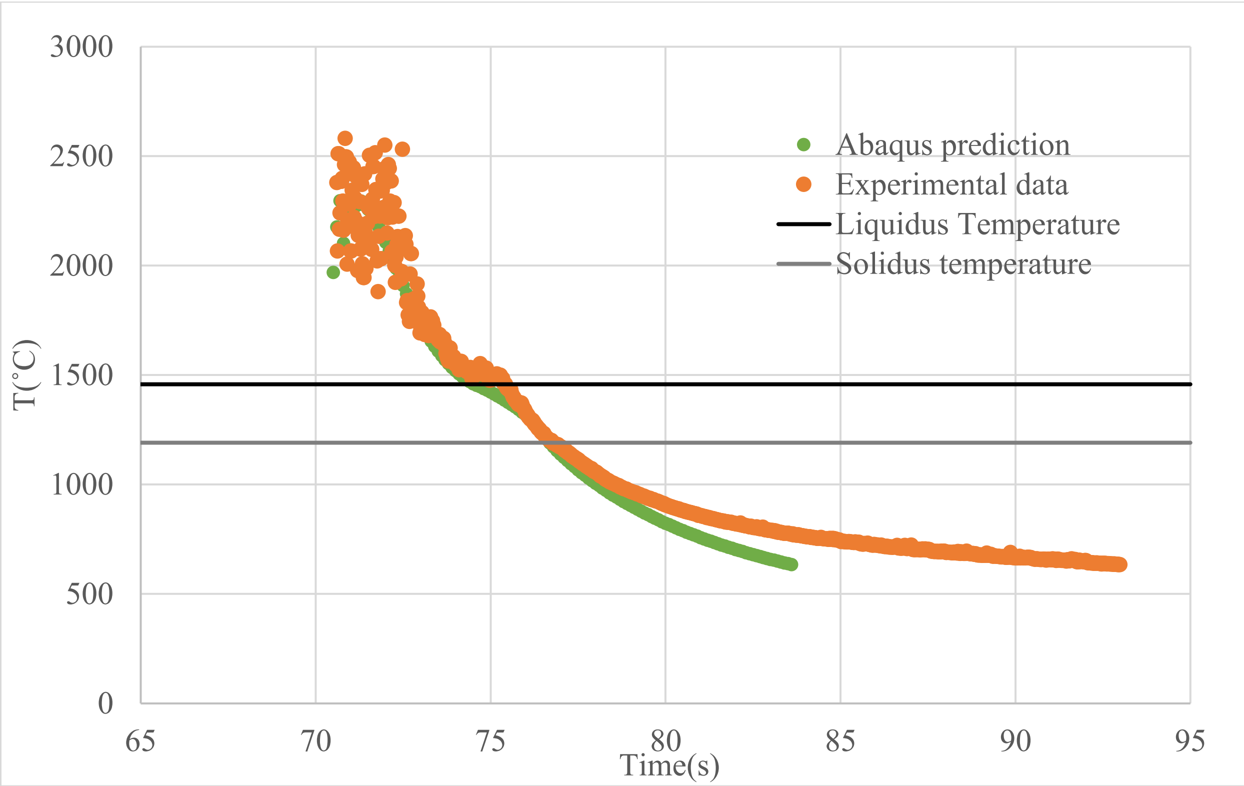

Figure C.5a: Temperature profiles for the 7th plate.

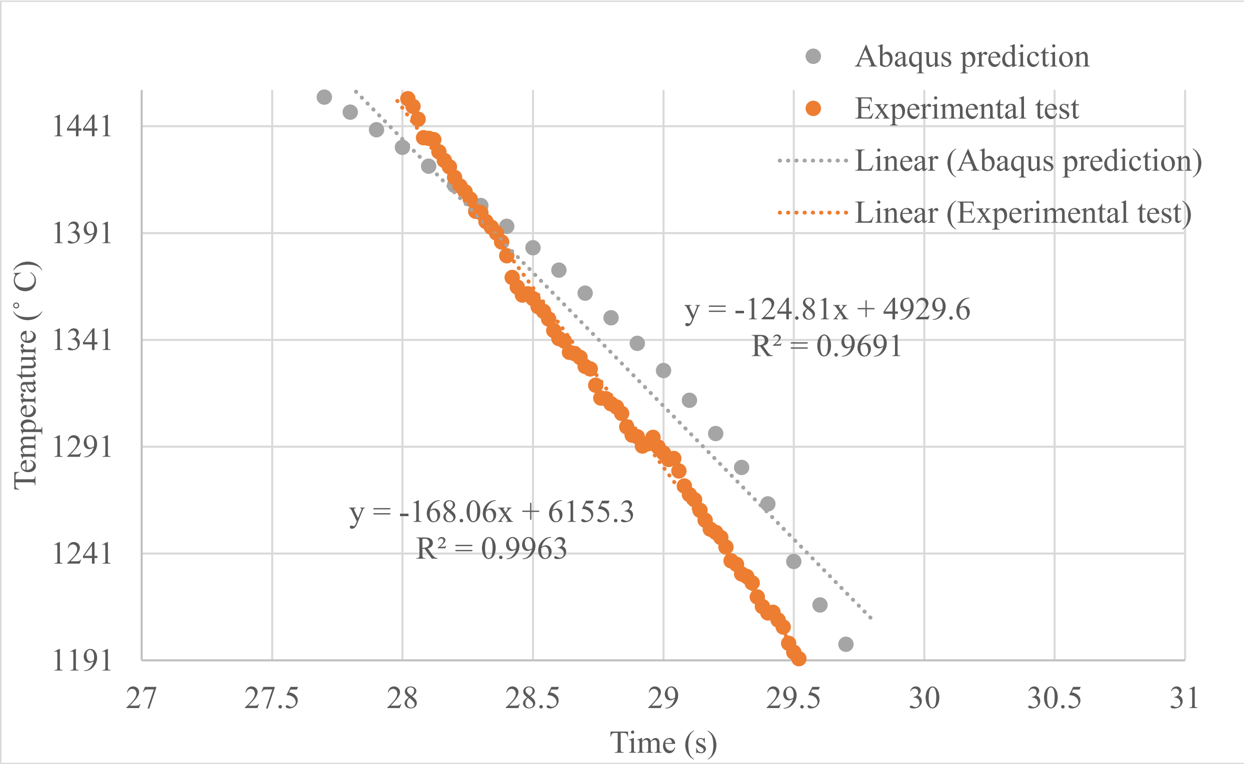

Figure C.5b: Temperature profiles in the range of liquidus and solidus temperature for the 7th plate.

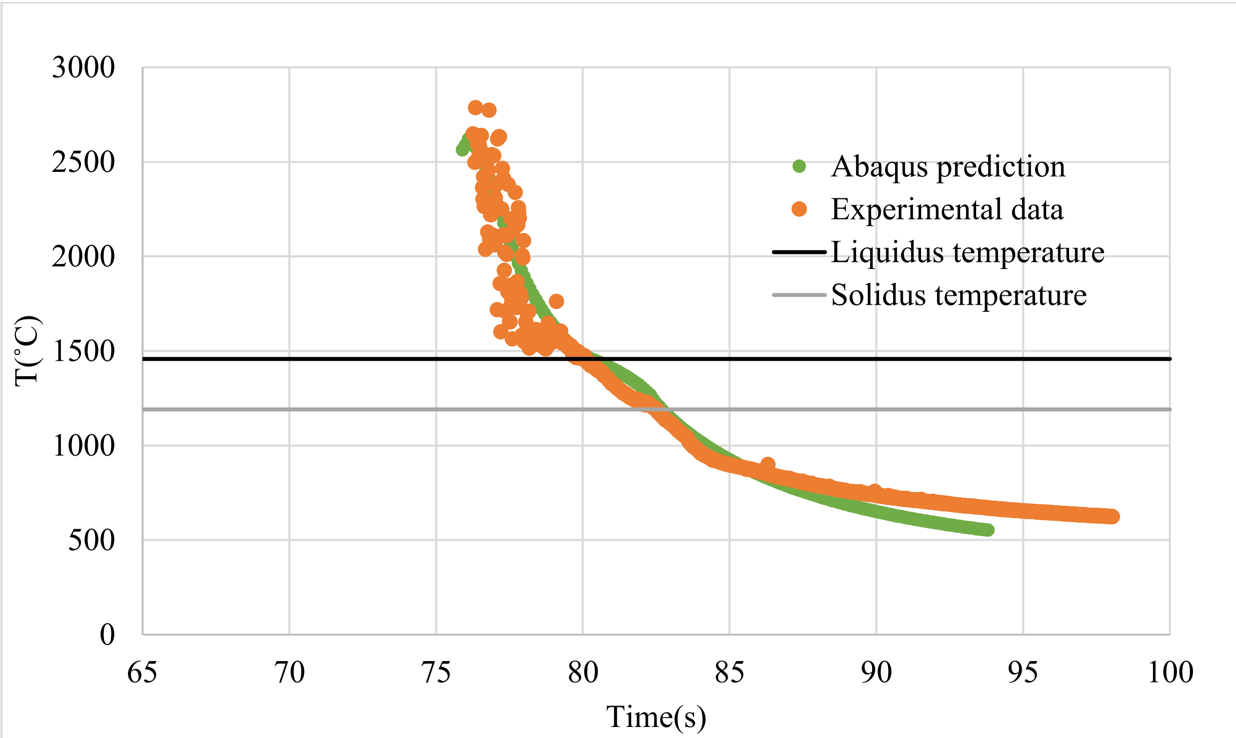

Figure C.6a: Temperature profiles for the 11th plate.

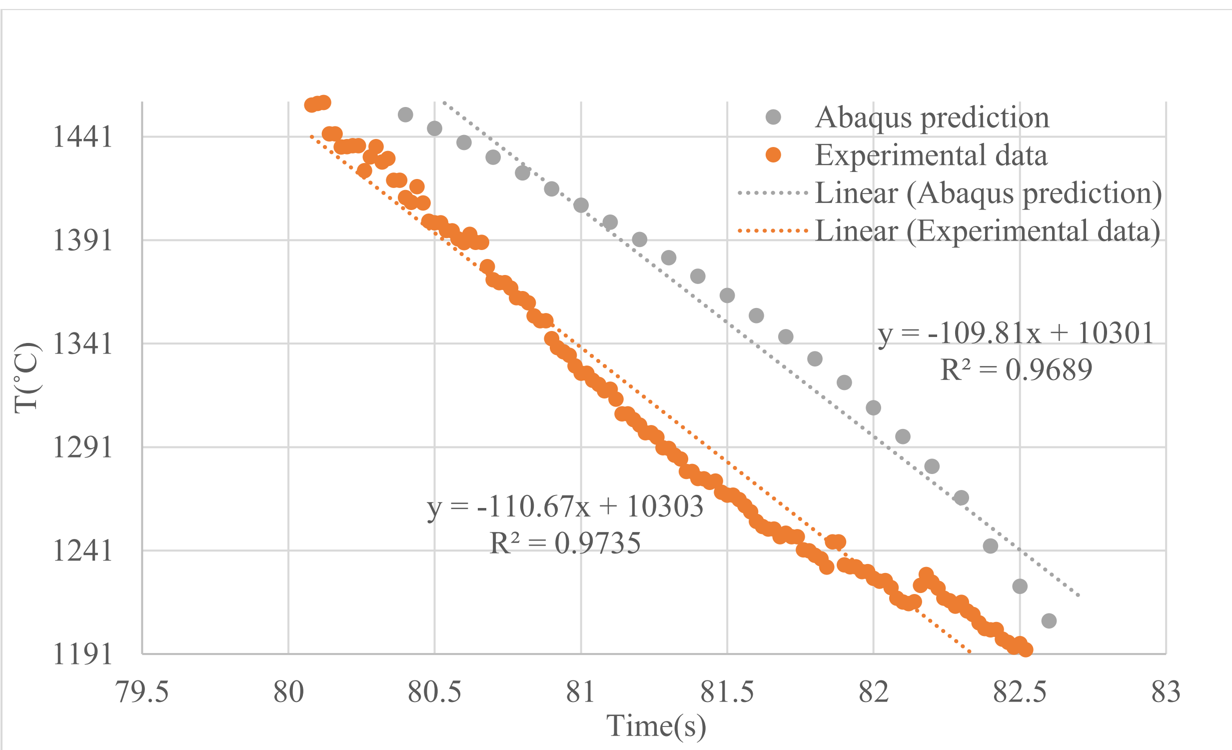

Figure C.6b: Temperature profiles in the range of liquidus and solidus temperature for the 11th plate.

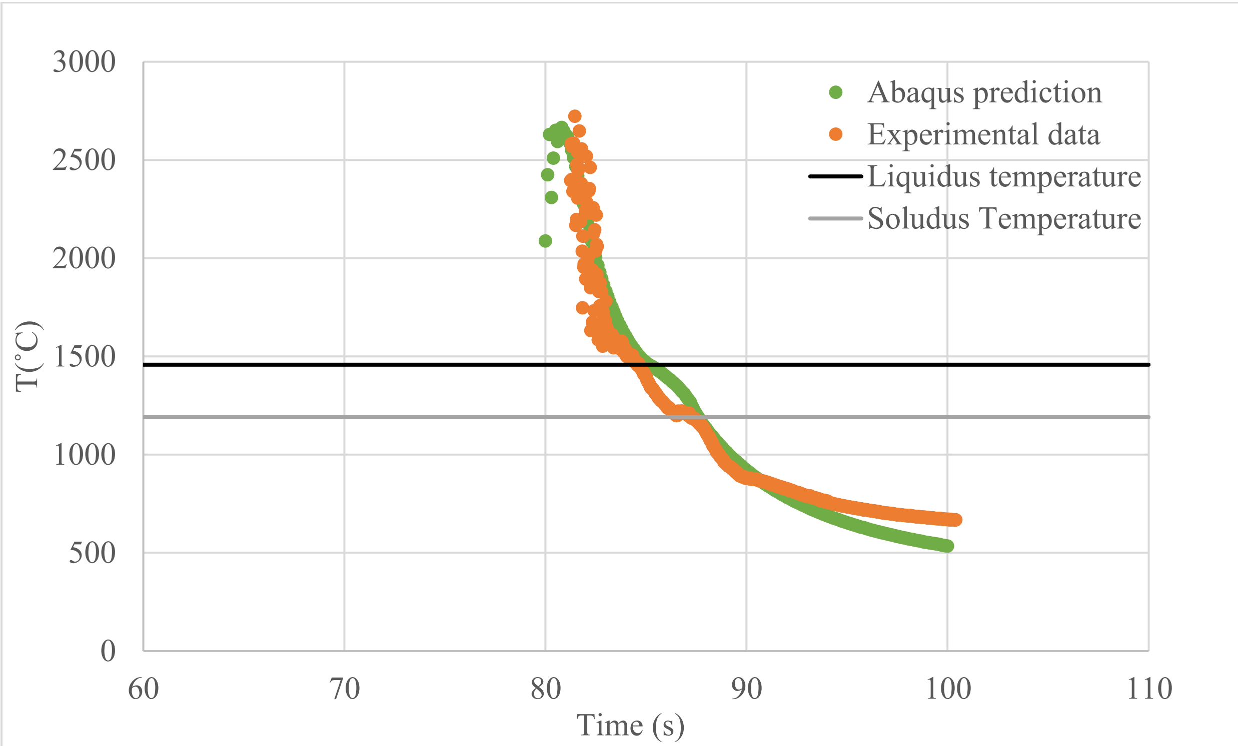

Figure C.7a: Temperature profiles for the 12th plate.

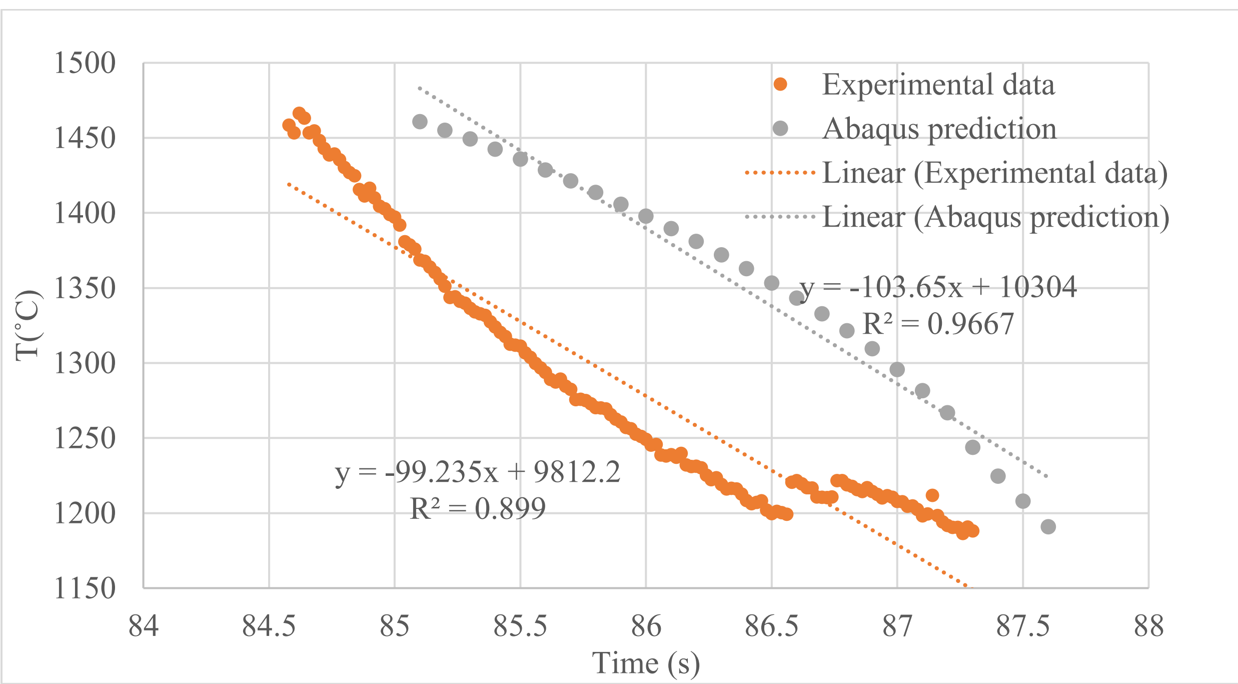

Figure C.7b: Temperature profiles in the range of liquidus and solidus temperature for the 12th *plate.*

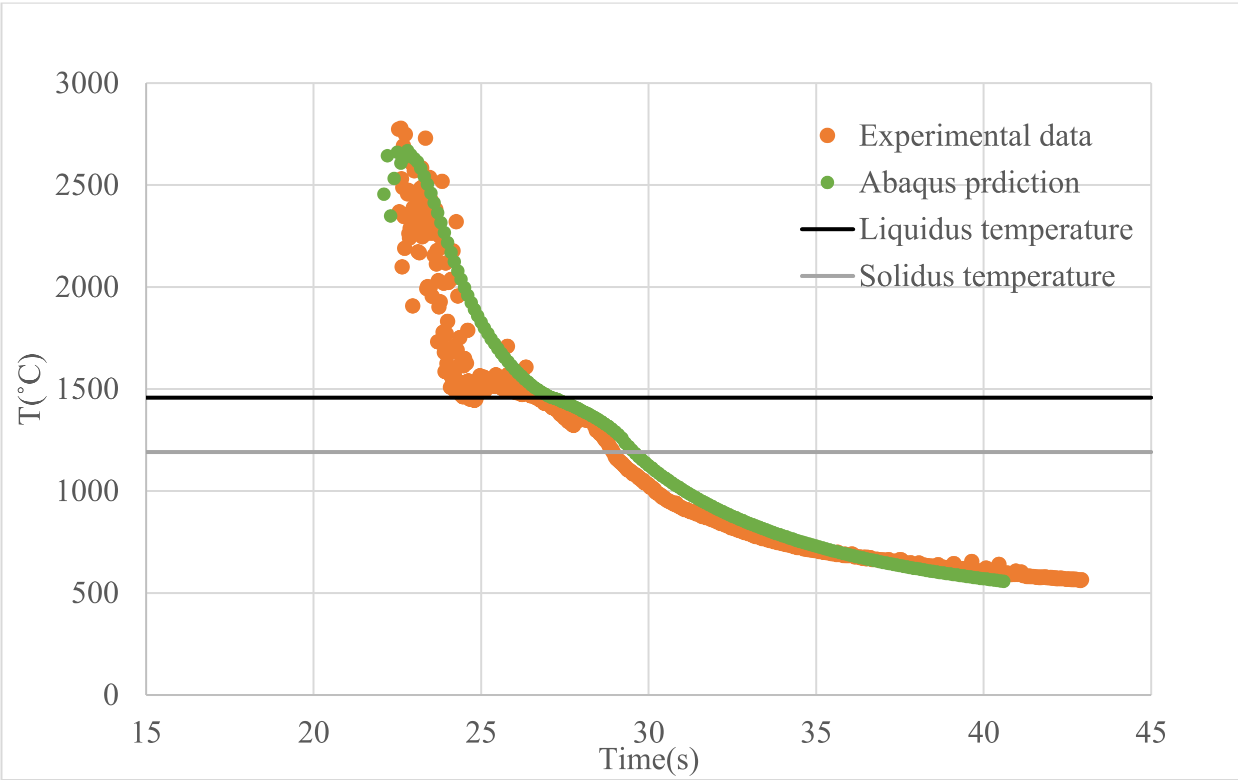

Figure C.8a: Temperature profiles for the 15th plate.

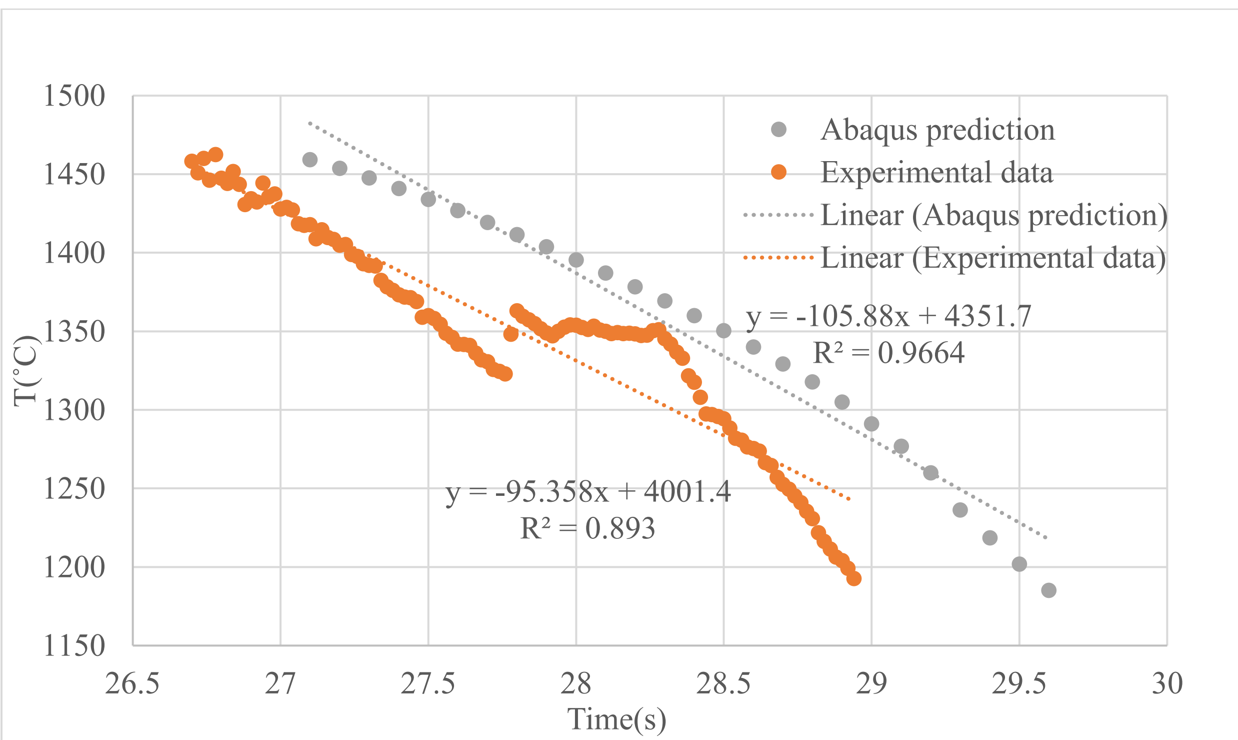

Figure C.8b: Temperature profiles in the range of liquidus and solidus temperature for the 15th plate.

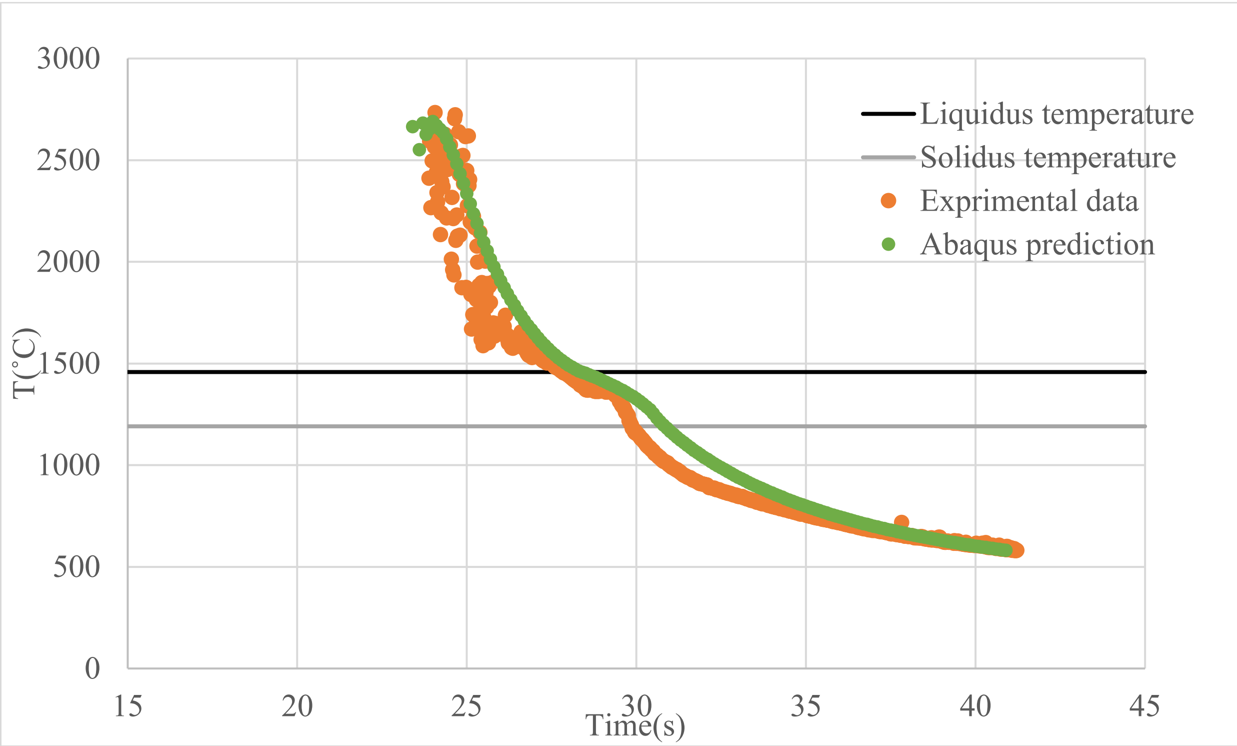

Figure C.9a: Temperature profiles for the 17th plate.

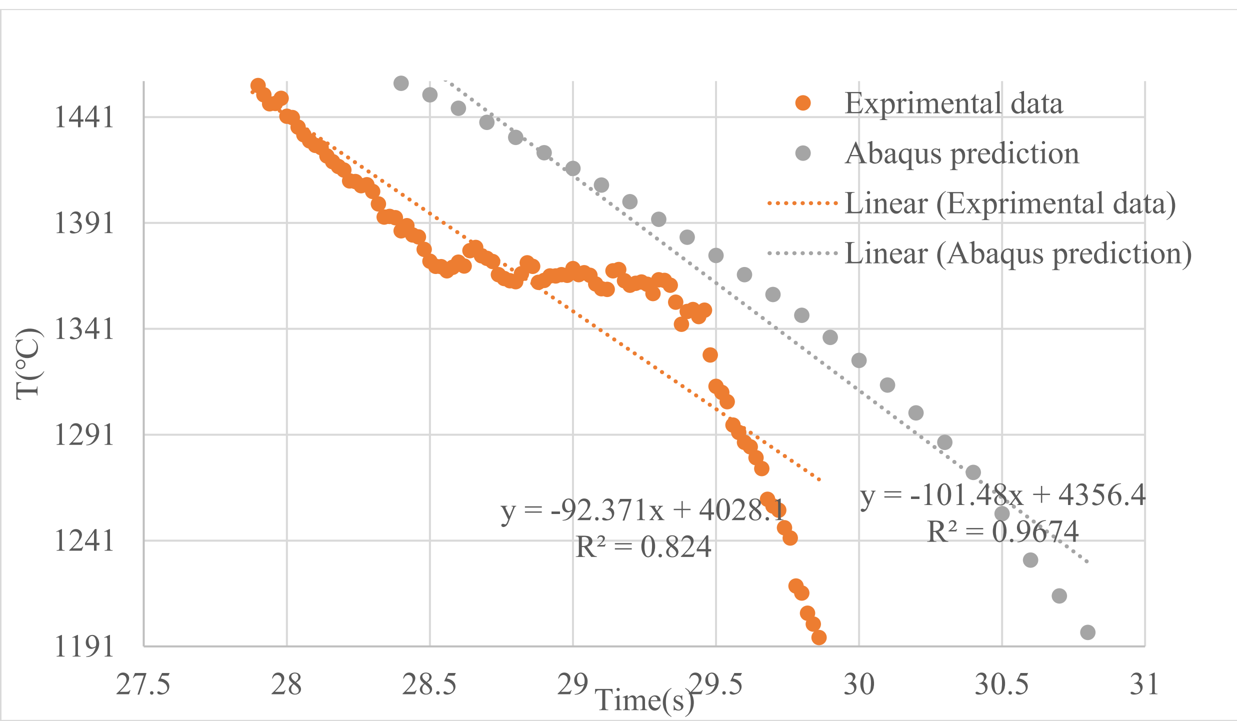

Figure C.9b: Temperature profiles in the range of liquidus and solidus temperature for the 17th plate.

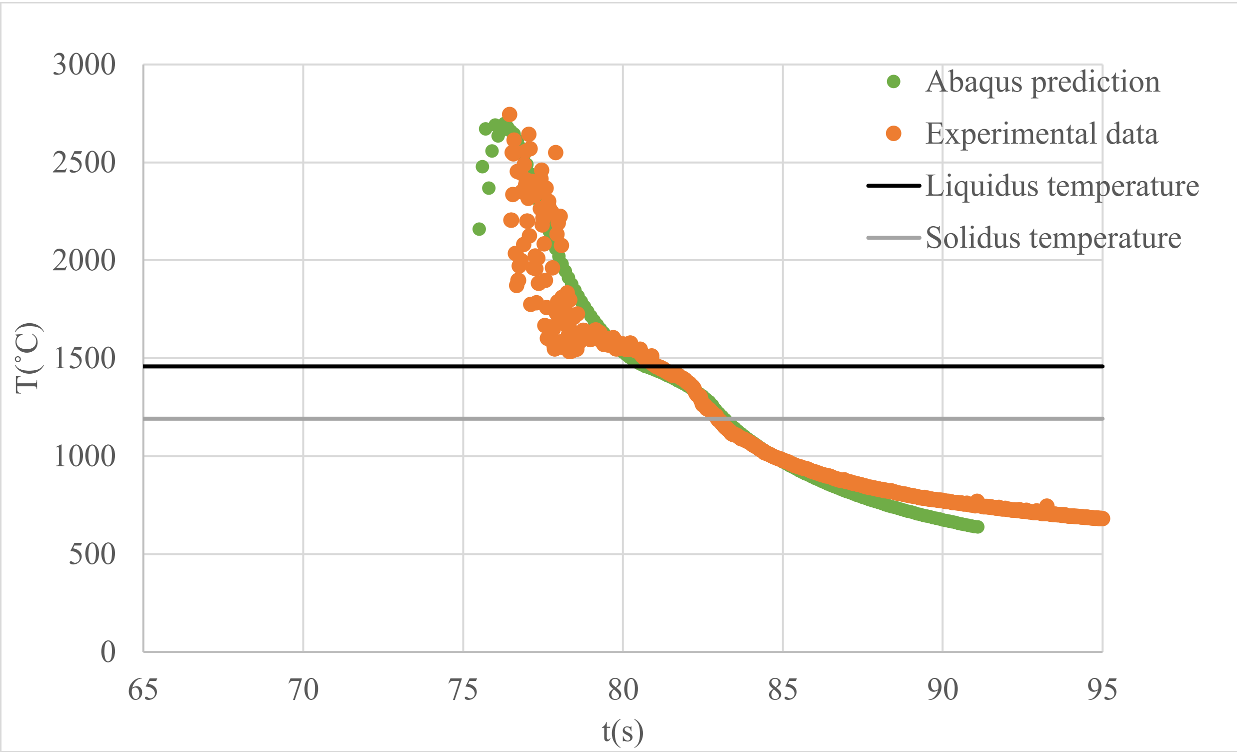

Figure C.10a: Temperature profiles for the 18th plate.

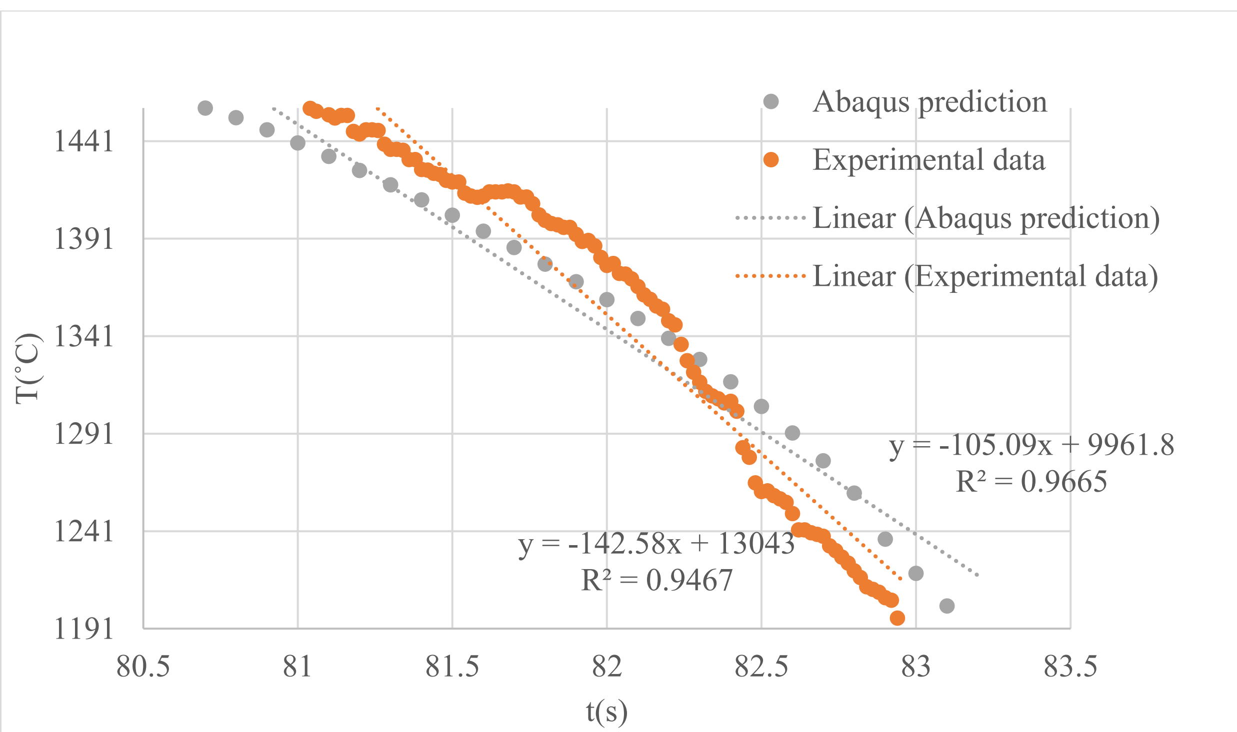

Figure C.10b: Temperature profiles in the range of liquidus and solidus temperature for the 18th plate.

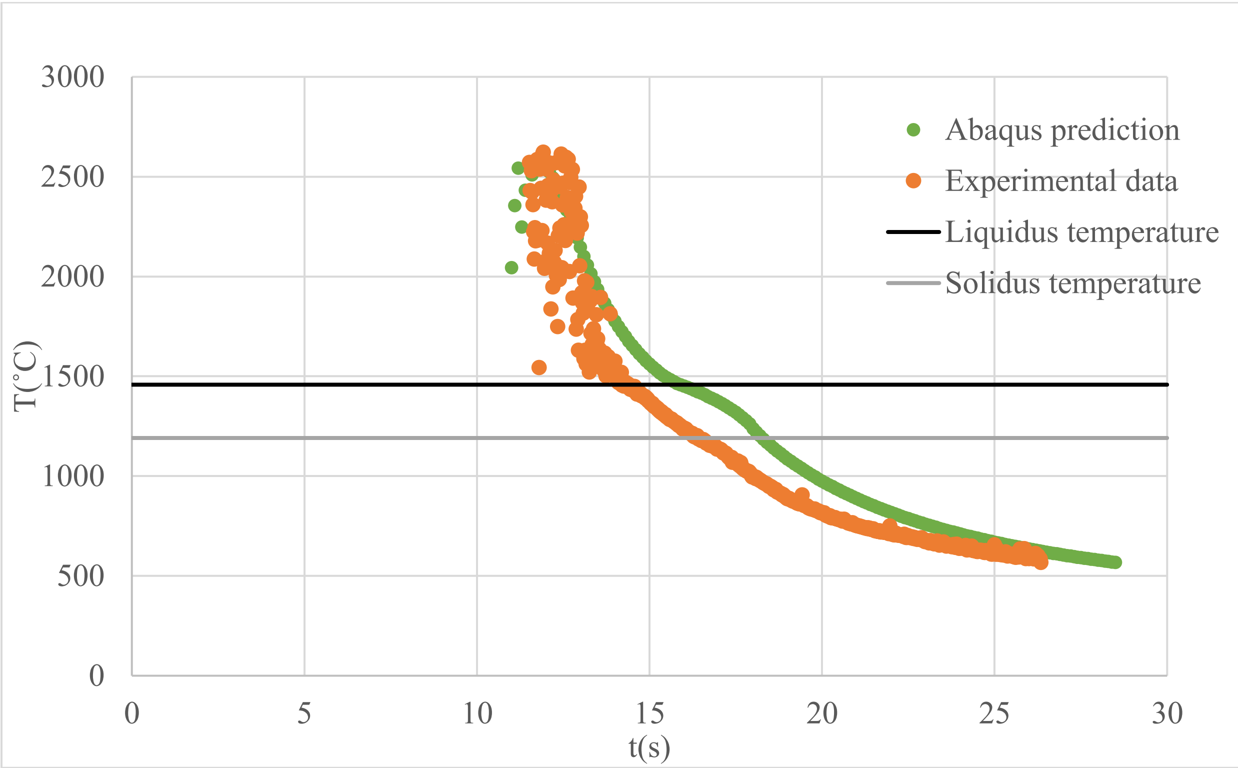

Figure C.11a: Temperature profiles for the 19th plate.

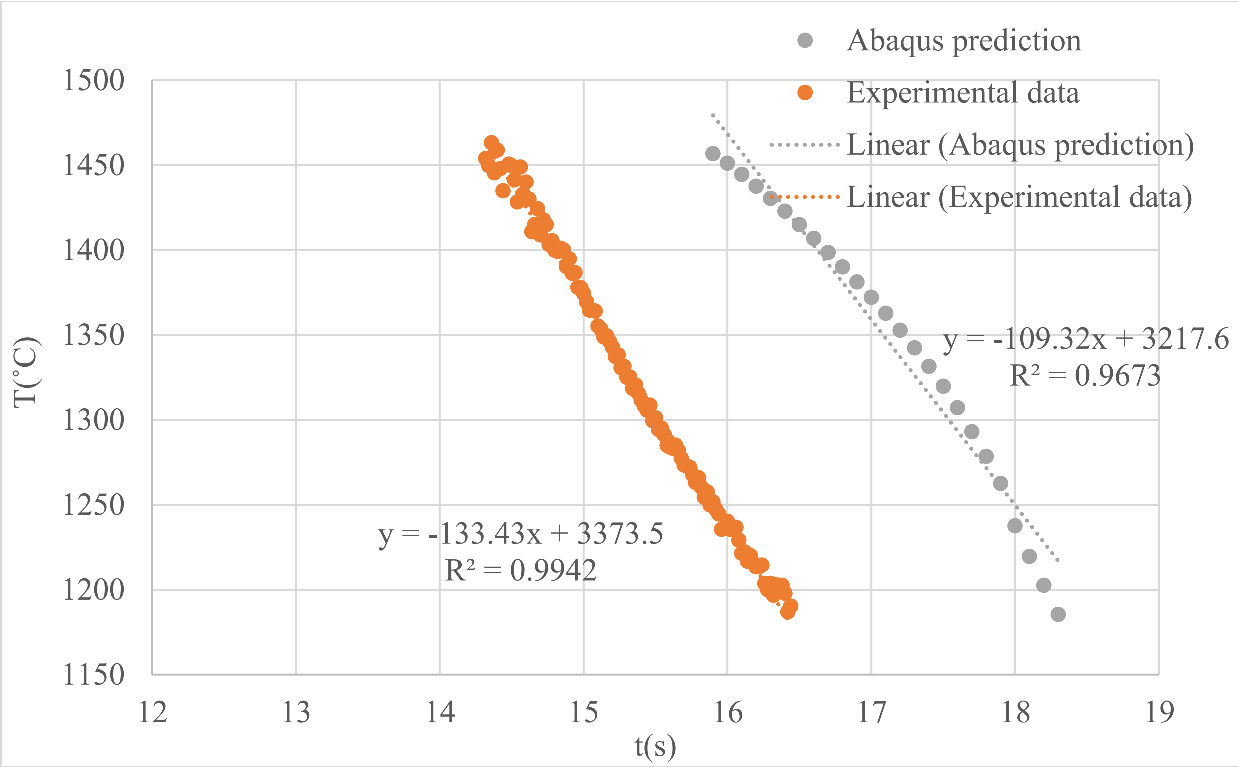

Figure C.11b: Temperature profiles in the range of liquidus and solidus temperature for the 19th plate.

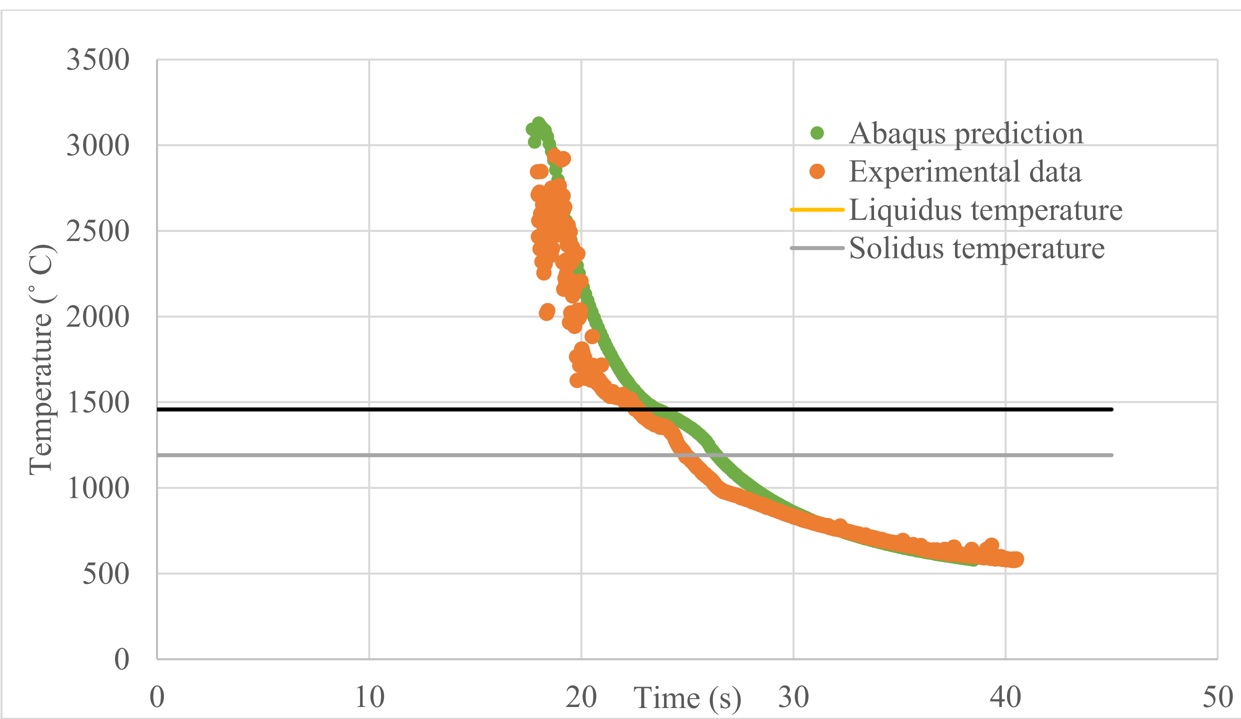

Figure C.12a: Temperature profiles for the 21st plate.

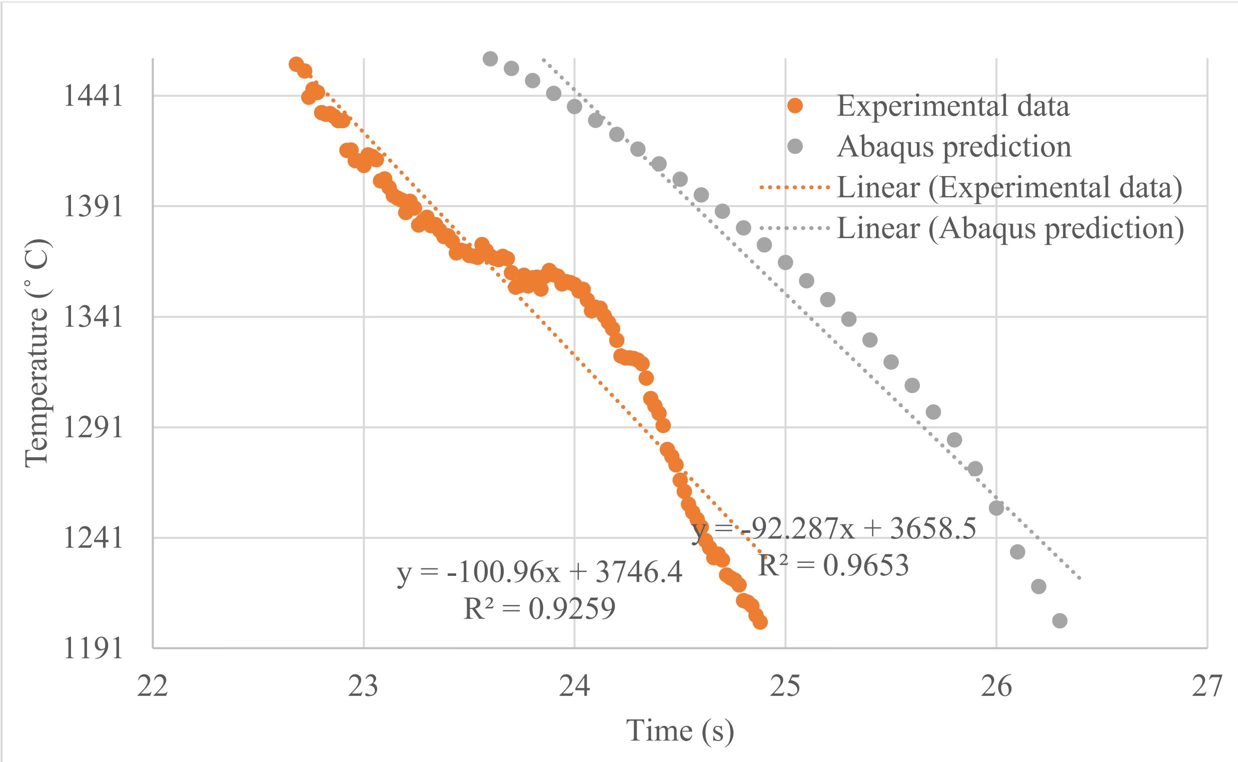

Figure C.12b: Temperature profiles in the range of liquidus and solidus temperature for the 21st plate.

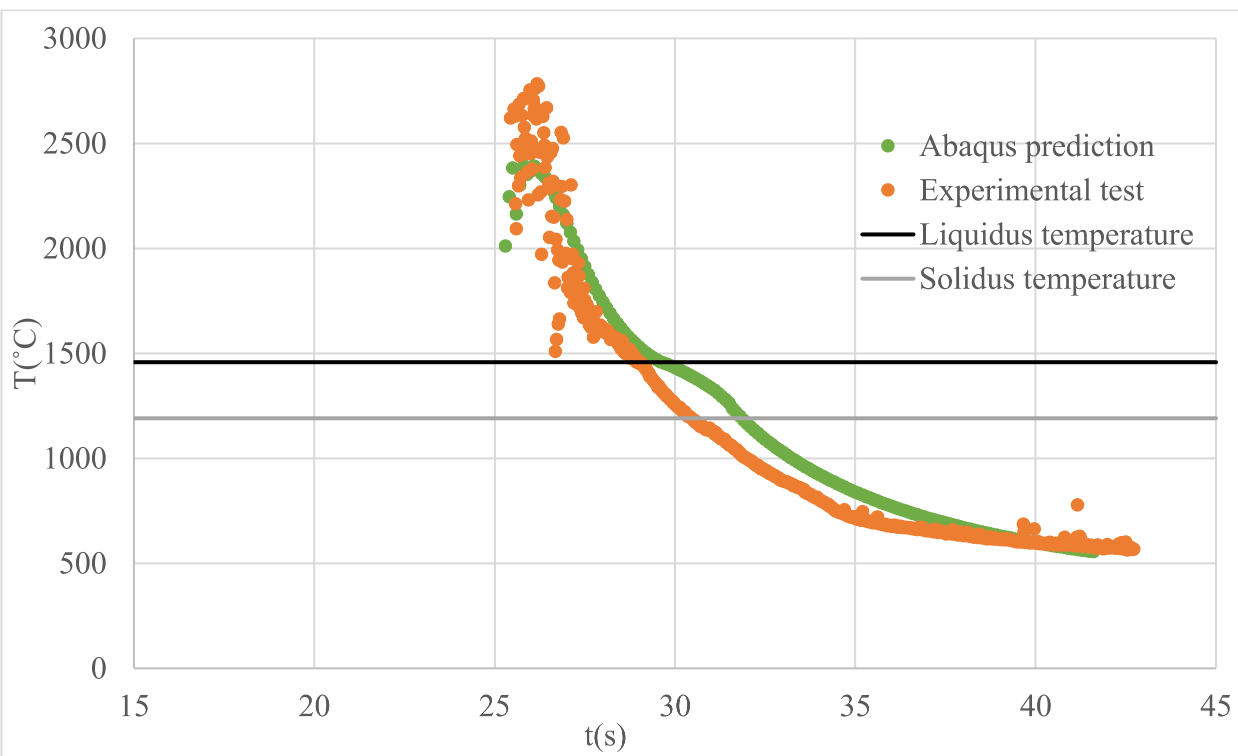

Figure C.13a: Temperature profiles for the 22nd plate.

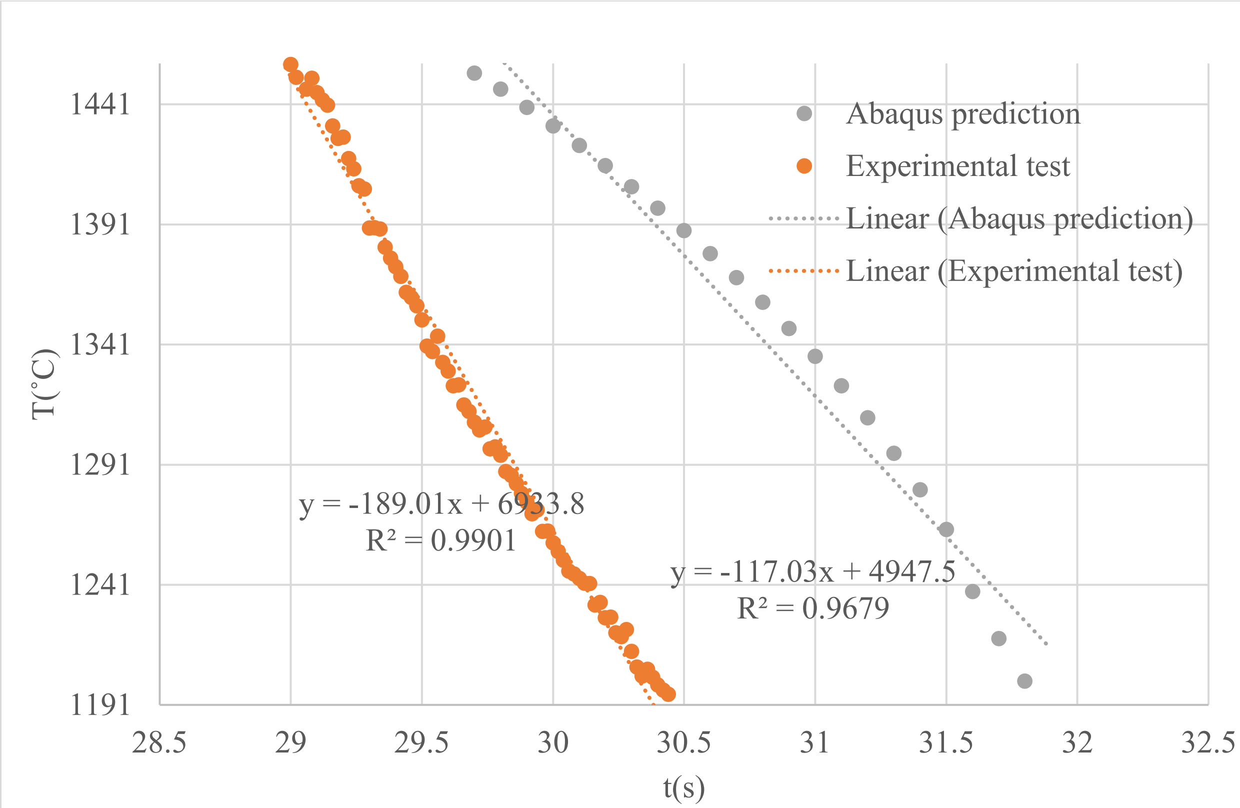

Figure C.13b: Temperature profiles in the range of liquidus and solidus temperature for the 22nd plate.

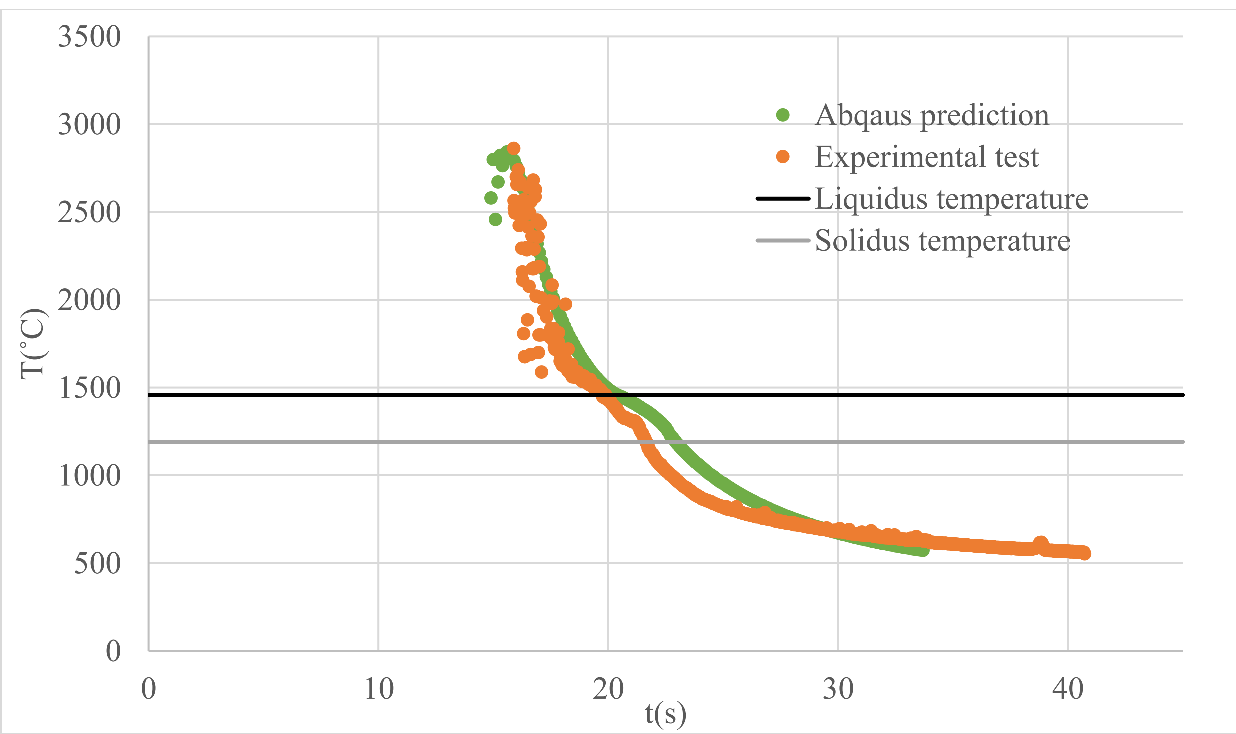

Figure C.14a: Temperature profiles for the 23rd plate.

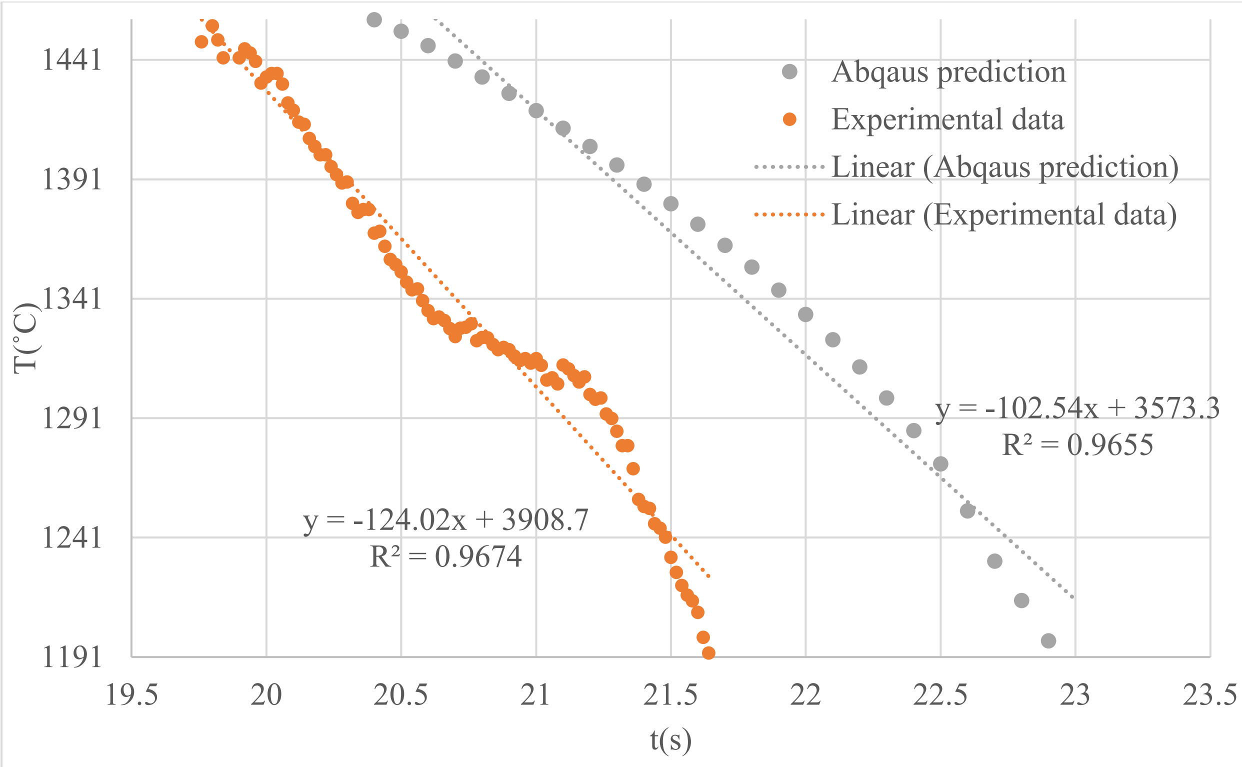

Figure C.14b: Temperature profiles in the range of liquidus and solidus temperature for the 23rd plate.

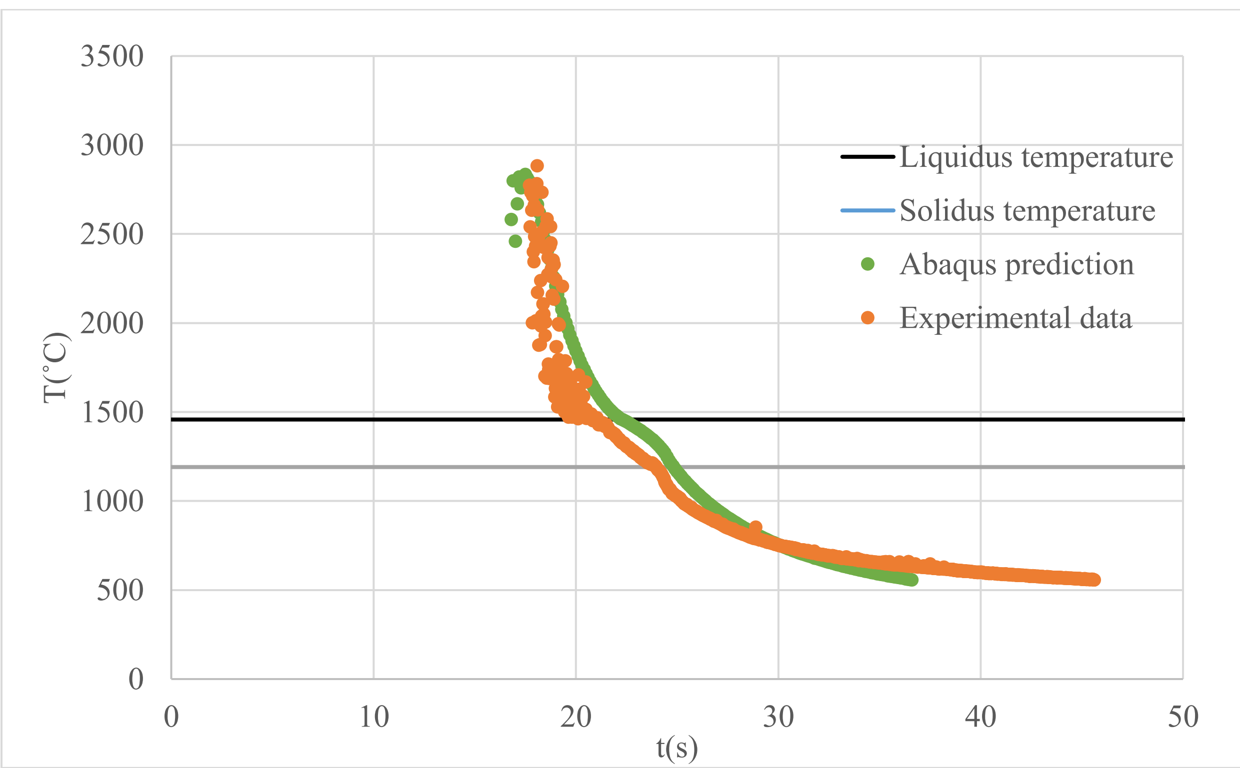

Figure C.15a: Temperature profiles for the 24th plate.

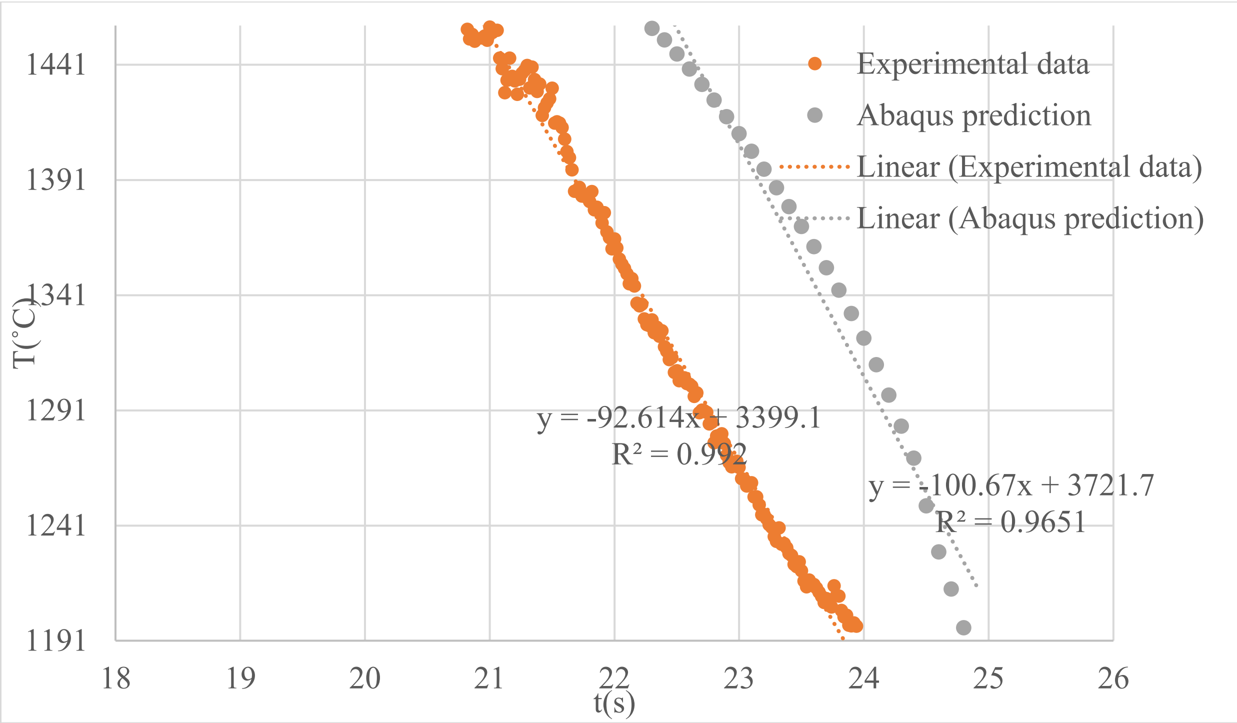

Figure C.15b: Temperature profiles in the range of liquidus and solidus temperature for the 24th plate.

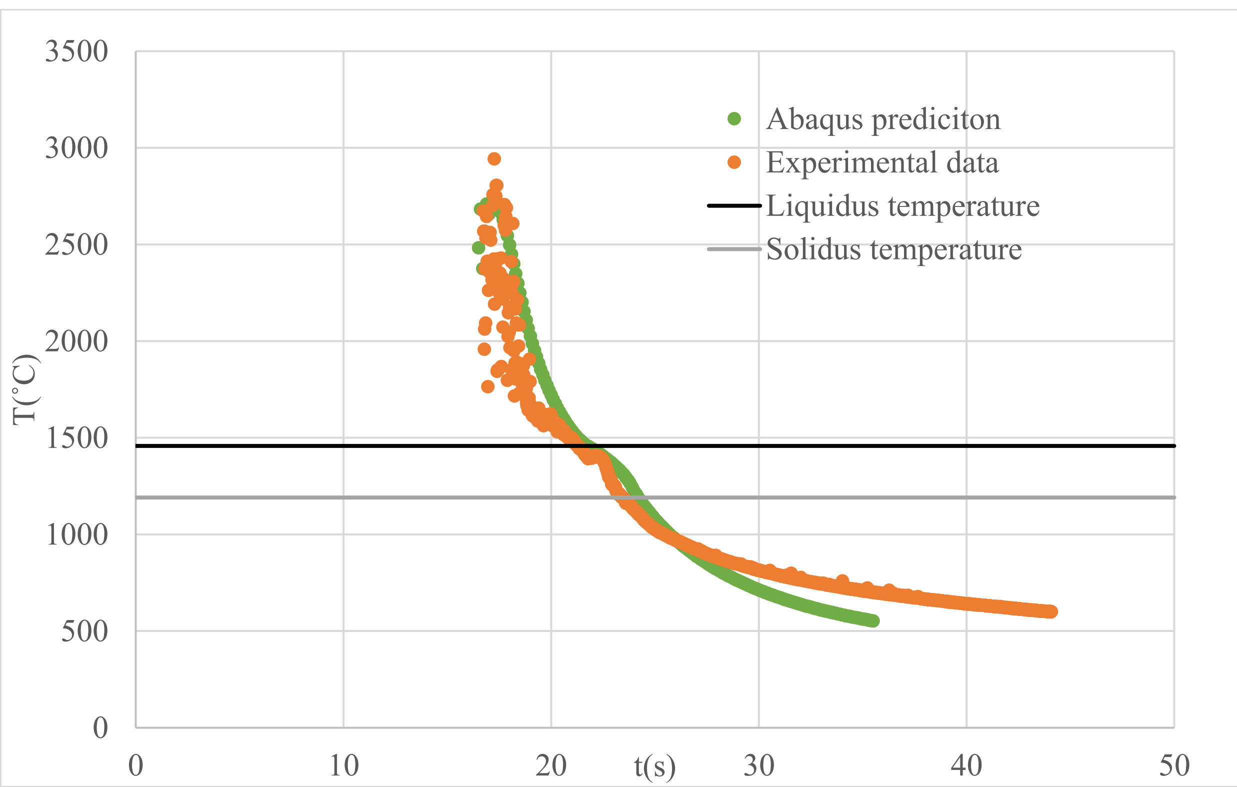

Figure C.16a: Temperature profiles for the 25th plate.

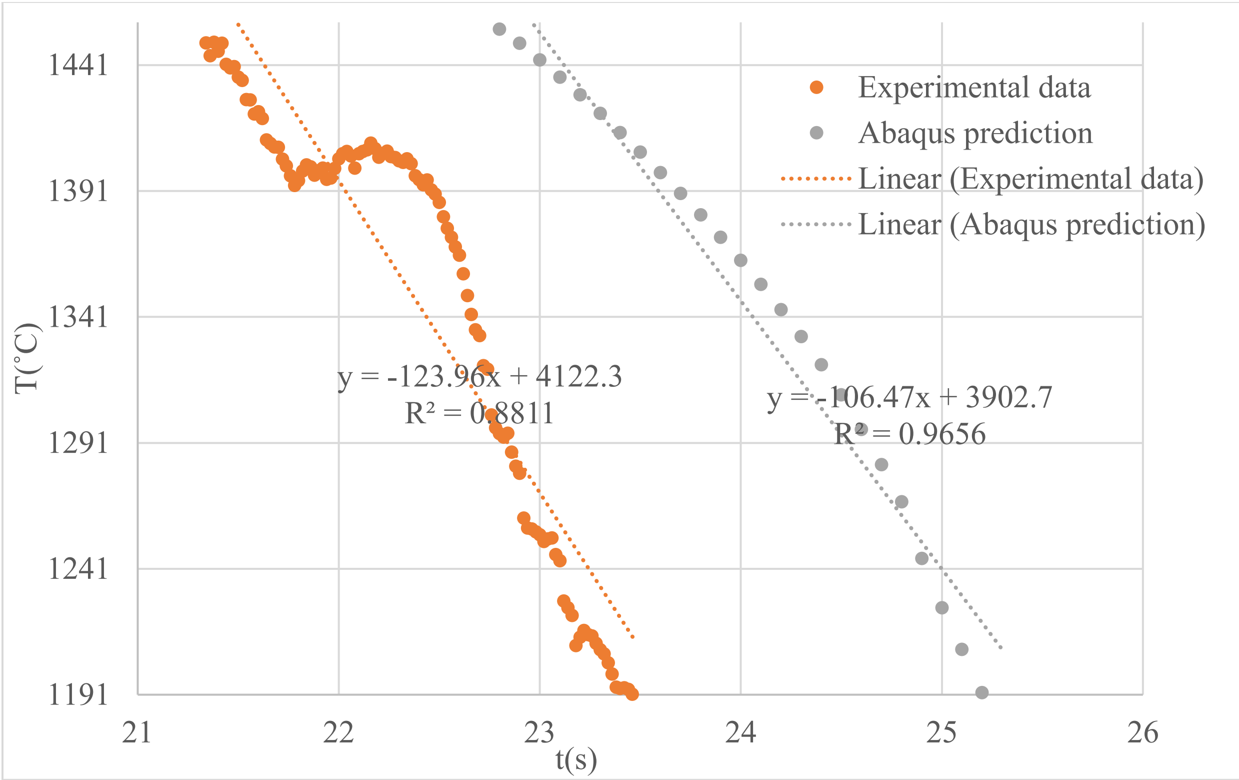

Figure C.16b: Temperature profiles in the range of liquidus and solidus temperature for the 25th plate.